# Reconfigurable Optical Devices Utilizing Chalcogenide Phase Change Materials

by

Mohsen Jafari

A dissertation submitted in partial fulfillment
of the requirements for the degree of
Doctor of Philosophy
(Electrical Engineering)
in the University of Michigan
2019

Doctoral Committee:

Associate Professor Mina Rais-Zadeh, Co-Chair
Professor L. Jay Guo, Co-Chair
Professor Anthony Grbic
Professor Vanessa Sih

Mohsen Jafari

jafarim@umich.edu

ORCID iD: 0000-0001-9906-954X



2019

*To*

*My Family*

*For their unconditional love*

# Acknowledgements

First, I would like to express my deepest appreciation to my advisor, Professor Mina Rais-Zadeh for her continuous support and guidance during the past five years. Her technical and life mentorship and motivation were essential to my success during my PhD years. I will be always thankful to her for providing me with this opportunity and for guiding me throughout these years. Moreover, I want to extend my genuine appreciation to my co-advisor, Professor L. Jay Guo who was a great teacher as well as an inspiring mentor. His support and guidance in carrying out the experiments and understanding the basics behind them helped me to better understand the results and push for the next steps. I would like to state my gratitude to Professor Anthony Grbic for providing me with his insight on the multi-layer device design from the electromagnetic aspects as well as his continuous support. Finally, I want to extend my thanks to Professor Vanessa Sih for her detailed comments on the underlying physics of devices implemented within this research.

Resonant MEMS group and Guo's research group were a very resourceful and inspiring places, which gave me supports and motivation to carry out this research. I am very thankful to all the group members especially to Azadeh, Adam, Muzhi, Cheng, Chengang, and Xi. I would like to particularly thank Muzhi for his support and for being my cleanroom mentor and Cheng for helping me with the experiments. Moreover, I want to take this opportunity to thank Professor Azadeh Ansari for being a very supportive friend and

collogue during this last five years. I also want to take this opportunity to thank our resourceful postdocs Dr. Haoshen Zhu, Dr. Jing Zhou, Dr. Afzaal Qamar, and Dr. Semi Oh for all their help, comments, and continuous discussions during my PhD. I am always thankful for both the friendship and guidance of all of them to achieve what is presented here.

I cannot leave University of Michigan without mentioning the great support and guidance that the staff at the Lurie Nanofabrication Faculty (LNF) provided for me, which helped me through everyday challenges of fabrications. Special thanks to David, Brian, Pilar, Vishva, Greg, and so many other staff, which were always there when I had a question or needed help with my process. I am also very thankful to be part of LNF and WIMS (center of wireless integrated micro-systems) at University of Michigan, where a great number of researchers shaped the future of nanotechnology and MEMS.

I also want to send my deepest thanks to my dearest friends in Ann Arbor, who made it a second home for me while being away from the family. I cannot imagine how life would have been in Ann Arbor without their support and friendship.

Most of all, I am deeply indebted to my parents, Ebrahim and Fatemeh for their unconditional support and endless love during all my years of studies and especially in the last five years. They were instrumental in achieving my goals throughout my life by providing me their never-ending cares and encouragement. I also want to thank my brothers

and sister for their unlimited and endless love. I dedicate this thesis to my family for their unwavering emotional support.

# Table of Contents

# List of Figures

# List of Tables

# Abstract

Tunable integrated photonic devices working at the visible and near infrared (NIR) regions are needed in a variety of applications such as in time keeping systems, imagers, displays, and memories, among others. To achieve tunability, a reconfigurable structure or material must be integrated within the device. Opto-mechanical devices go through structural change and have the advantage of larger tunability compared to that of an electro-optical device. Electro-optical devices are essentially dependent on the change in the properties of the materials, which is usually a small change. However, electro-optical devices are cheaper, faster, more reliable, and are easier to integrate due to their smaller dimensions as compared to opto-mechanical devices. With the advancements in the nanotechnology and the introduction of micro-electro-mechanical (MEM) devices, some of these issues are addressed in micro-structures. However, generally speaking, the MEM structures still suffer from low yield and/or complex fabrication processes mostly as they include a suspended structure or a moving part.

From a large selection of materials which can provide tunability, phase change materials (PCMs) stand out due to their reliable phase transitions and relatively large change in their optical and electrical properties as they go through crystallographic phase transition. Specifically, Germanium Telluride-based compounds, such as Germanium Antimony Telluride (GST) and Germanium Telluride (50:50) (GeTe), exhibit very

different optical and electrical properties when they undergo phase transitions. Compared to the more commercialized GST material, GeTe has a much simpler fabrication process, more reliable phase transitions and lower loss at the visible wavelength and thus is the material selected in this research. Two stable phases of GeTe exist at room temperature: amorphous (a-GeTe) and crystalline (c-GeTe), which have drastically different optical and electrical properties at NIR and noticeable differences in the visible range.

Here, for the first time, a transmissive optical shutter is demonstrated that employs GeTe in a multi-layer sub-wavelength grating structure. The shutter exhibits an excellent contrast of ~30 dB (the ON/OFF power ratio) with transmission loss of < 3 dB when the shutter is OFF at the wavelength of 1.55 μm. The measured response verifies the modeling results. By stacking more layers, a noteworthy contrast of 70 dB is achievable with this structure. The ON state of the shutter is achieved by transitioning the a-GeTe to c-GeTe by heating to its crystallization temperature (~200 °C). Resetting the c-GeTe to a-GeTe brings the device back to the OFF state. To go to the a-state, the GeTe temperature is raised to near its melting point (~750 °C) followed by quick removal of heat. In our shutter, the sub-wavelength array of gold lines also provides efficient joule heating to change the phase of GeTe (indirect heating scheme). The same gold grating provides the heat sink required for fast cooling of GeTe during the amorphization process. It is worth mentioning that since both phases of GeTe are stable at room temperature, this shutter consumes zero static

power. This is in contrast with Vanadium Oxides ($VO_x$) and liquid crystal-based devices which need constant applied power to maintain the ON or OFF state.

A reflection-based shutter is presented in the subsequent chapter of this thesis. The reflection-based shutter structure includes only a thin layer of GeTe (~40 nm) on a bottom gold heater and yet exhibits a measured contrast (modulation index) of > 20 dB at the visible and NIR range (780 nm-1.1 μm). This shutter can tune the intensity of the reflected light at two different wavelengths, which is useful for multi-frequency applications. This device is the first integrated shutter (or modulator) working in the visible wavelength range using the lossy GeTe. The structure of the device is further modified in the next device, the first color reflector at visible wavelengths, to enhance the device performance, considering the high loss of GeTe in the visible range. Using a thin layer of GeTe two interchangeable red and blue colors are achieved in the color filter that includes a sub-wavelength coating (300 nm) of GeTe.

Another contribution of this thesis work is to show, for the first time, the dependency of the phase transition temperature of thin-film GeTe to its thickness and to employ this interesting property to achieve more than two colors using only GeTe as the thermochromic material. It is shown here that with thinner GeTe films of < 20 nm, the glass transition temperature increases as the thickness is reduced. Such dependency of the glass transition temperature on the film thickness is further employed to demonstrate the first integrated

multi-layer PCM device working at the visible wavelength. This device shows four vivid interchangeable red, yellow, green, and blue colors using a single joule heating element.

Finally, a novel grating-based reflective color filter is shown here by integrating GeTe grating on a silicon dioxide ($SiO_2$) waveguide to enhance the number of colors and the color dynamics. An integrated thin-film silver heater is deposited under the GeTe film with an ultra-thin $SiO_2$ passivation layer. Such device demonstrates several interchangeable colors when the phase or pitch of the GeTe grating is changed.

Future work includes studying of the device reliability, exploring the use of other phase change materials, and other methods for achieving phase transition more reliably, efficiently, and/or at a higher speed.

# Chapter 1: Introduction

## 1.1. Motivation

Optical shutters, modulators, and tunable color filters are ubiquitous in modern society. Applications of such devices include sport cameras, integrated photonics for communication, imaging, and spectroscopy, in atomic clock assemblies, and in other consumer/commercial products, aerospace components, and automotive parts (Figure 1) [1.1-1.10].

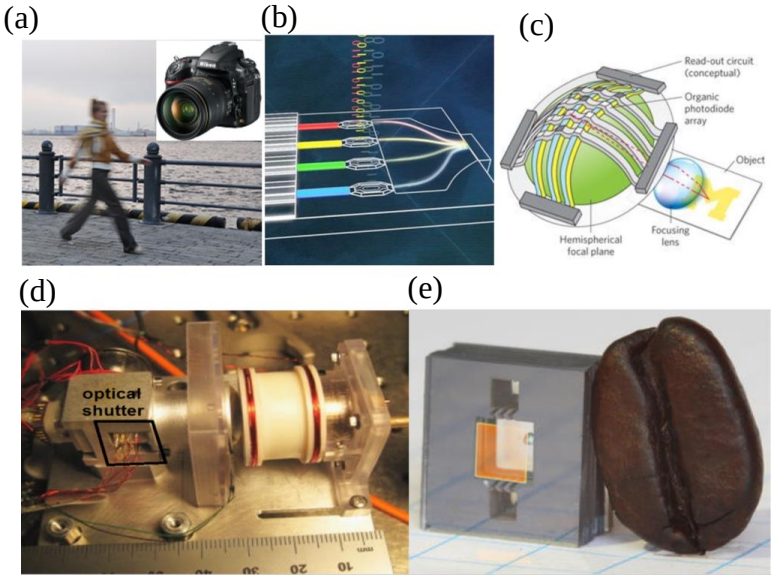


Figure 1. Different application of the tunable optical components ranging from (a) photography, (b) silicon photonics [1.7], (c) sensing and communications [1.8] to more specific systems such as (d, e) atomic clocks [1.9, 1.10].

The core part of these tunable optical devices is the reconfigurable element (material or structure) integrated within each device. This re-configurability either results from micrometer-scale changes in the structure using moving elements such in opto-mechanical devices [1.11-1.13] or relatively small changes in the material properties such as in electro-optical systems [1.14-1.16]. Mechanical devices demonstrate significantly higher optical performance in color filters and modulators (in terms of number of colors, color vivacity and contrast, *etc.*) by changing the structure of the device compared to that of an electro-optical system with fixed structure. However, mechanical devices are usually bulky, less reliable, and less durable; they also consume more power compared to the electro-optical systems [1.17]. Moreover, it is more difficult to integrate mechanical devices in microsystems, as they require more complicated processes for successful integration [1.18]. Electro-optical devices use a fundamental change in the material properties to modulate or filter the reflection or transmission of the light at the desired part of the spectrum [1.19]. As the optical properties of the well-known electro-optical materials change slightly, the electro-optical devices usually suffer from lower optical performances compared to those of opto-mechanical systems [1.20, 1.21]. There are different materials, whose electrical and/or optical properties will change in response to external stimuli and can find uses in aforementioned applications. Examples of these materials include but not limited to two dimensional (2D) materials such as graphene and transition metal dichalcogenide (TMD) [1.22, 1.23]. The drawback with 2D and TMD

based devices is their low reliability despite heavy research in this field during the past few years. Moreover, they show poor repeatability and cannot meet the uniformity needed for large-scale commercial devices [1.24]. Alternatively, liquid crystal (LC) and vanadium oxides ($VO_x$) have shown reliable performances for large-area devices with acceptable number of switching cycles [1.25, 1.26]. As shown in Figure 2, using these materials, the change in the optical output intensity is limited and also temperature dependent.

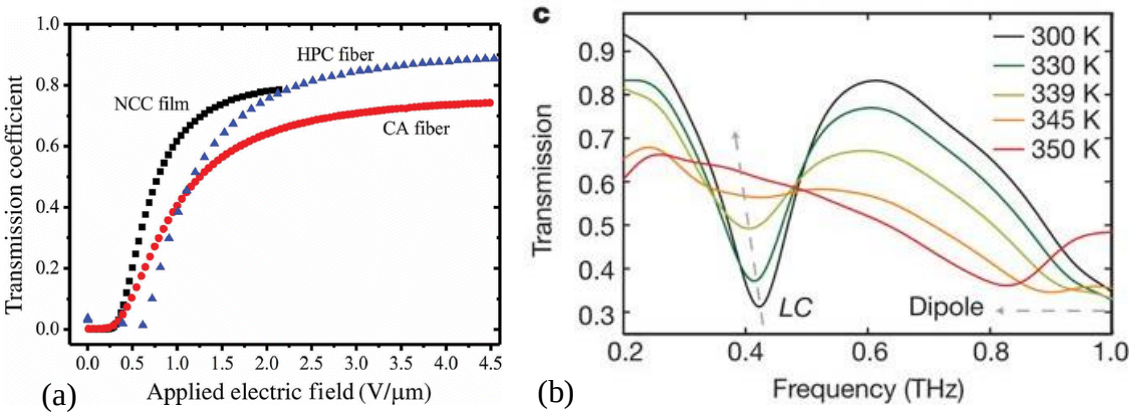


Figure 2. (a) Curves of the applied electric field dependence of the light transmission coefficient [1.25]. (b) The change in the transmission of the light at different temperatures using $VO_2$ [1.26].

Interest in liquid crystals or TMDs is due to their well-developed processes and higher dynamic range of optical, electrical, and mechanical properties compared to those of comparatively new 2D materials [1.27]. However, both $VO_x$ and LC require constant power to stay in one state, which results in large power consumption [1.28]. Non-volatile

phase change materials (PCM), on the other hand, can have two room temperature-stable states, amorphous and crystalline, with different electrical and optical properties (see Figure 3) [1.29, 1.30]. In other words, they can possess two different properties at room temperature, making them prime candidates for ultra-low power and low-duty cycle applications [1.31].

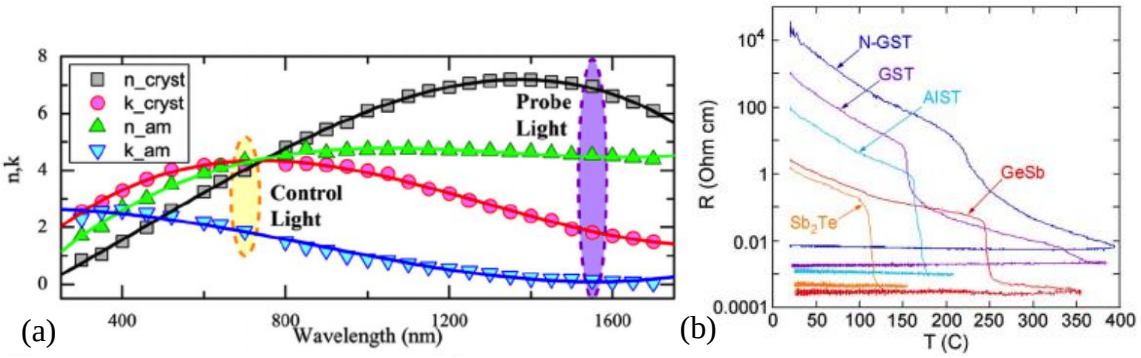


Figure 3. The refractive index of GST at different wavelengths [1.29]; (b) Resistivity as a function of temperature during a heating cycle at 1 K/s for initially amorphous, as-deposited 50-nm-thick films of various phase change materials [1.30].

This memory-like property of PCMs made them suitable for non-volatile memory applications. The crystallographic phase transition of PCMs occurs in response to an external stimulus, such as electrical field, heat, or strain [1.32]. Germanium Antimony Telluride (Ge-Sb-Te or GST), which is one of the well-known chalcogenide glasses with superior phase transitions, is one example of PCMs with high potential in applications requiring resistive switching and in optical devices [1.33], [1.34]. Figure 4 shows an

example where the change in the refractive index of GST is used to achieve two different colors at the crystalline and amorphous phase [1.34]. In this example, the color reflected in the visible range is changed from pink to orange for a 180 nm film.

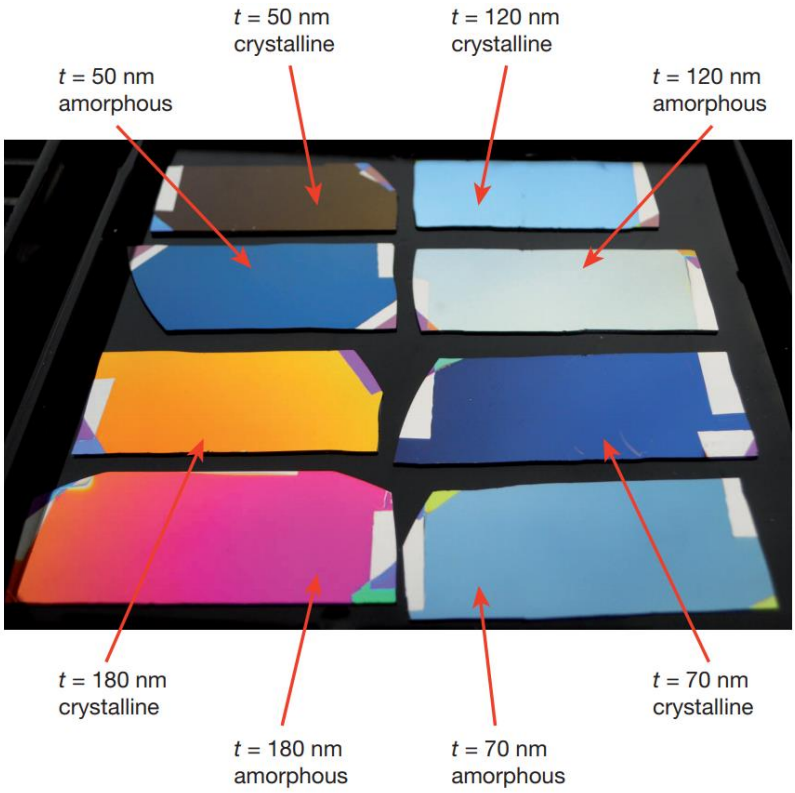


Figure 4. The reflected color of a GST-based color filter with different thicknesses of the stack [1.34].

However, due to the presence of Antimony in the compound, there are concerns with contamination issues and safety when processing GST and hence GST is not a favorable material. Furthermore, GST has a high optical loss in both amorphous and crystalline states

with a relatively small change in the real part of the refractive index (Figure 3) [1.29], [1.35]. The high k value of GST makes it challenging to design low-loss optical devices operating at the visible (VIS) or near infrared (NIR) regions of the spectrum [1.34]. Germanium Telluride (GeTe), which is a chalcogenide compound similar to GST, has also high loss at the visible wavelengths [1.36]. However, it has low losses in the NIR range as shown in Figure 5(a) for the amorphous GeTe. It also does not have the contamination concerns of GST. Moreover, due to a higher glass transition temperature (Tx) and higher gas pressure for the Germanium (Ge) and Tellurium (Te) compared to Antimony (Sb), it is more stable in both amorphous and crystalline phases. Some existing data on the optical refractive indices of the GST and GeTe are shown in Figure 3 and Figure 5. Further characterization is needed to extract the optical index of the GeTe in both phases in the visible and NIR regions, where such data is none existent or not reliable (compare Figures 3 and 5).

In summary, GeTe has more desirable optical and electrical properties, more reliable fabrication processes, and more endurance against variation, aging, and harsh physical stressors and therefore more suitable for tunable optical devices.

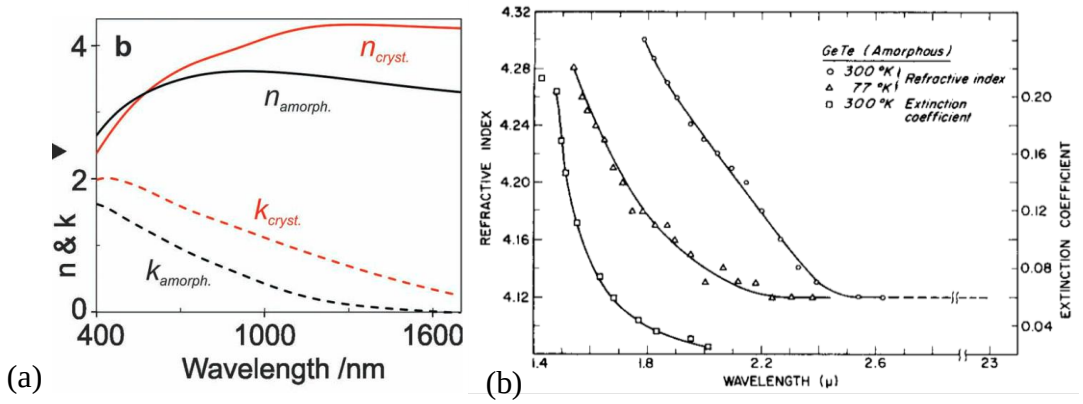


Figure 5. The optical refractive index of both phases of the GST (a) and the amorphous GeTe (b) for the NIR region [1.35, 1.36].

In this thesis work, new reconfigurable optical devices using GeTe are devised working at the NIR and visible ranges with record-breaking optical properties. The basic properties of chalcogenide-based PCMs and specifically GeTe are discussed in this chapter followed by a brief summary of research objectives and contributions. In the following chapters, the design, fabrication, and characterization of the devices are discussed in detail.

## 1.2. GeTe as a reconfigurable optical material

As mentioned earlier, GeTe has the ability to switch between its glassy resistive amorphous phase to the metallic conductive crystalline phase in response to external heat stimuli. The required heat can be generated by passing current through a resistive heater [1.33] or by using a laser beam at the wavelengths that the material has high optical absorption [1.37]. The resistivity of GeTe changes by more than four to six orders of

magnitude when it undergoes this phase transitions. Moreover, the real and imaginary parts of the refractive index for GeTe increase by a factor of two and ten, respectively, when transitioned from amorphous to crystalline phase at 1.55 μm. As mentioned before, GeTe remains in the crystalline state even when the heat source is removed due the non-volatile nature of the material. This memory-based phase transition is desirable in ultra-low power applications with low refresh rate such as non-volatile memories.

GeTe- or GST-based memories have been exploited for the last decade due to their almost zero static power and high speed [1.31], [1.32]. GST-based memory devices have been proven to provide sub-10 nanoseconds electrical access times [1.38]. They have also shown an ultra-fast sub-picoseconds access time when they have been read/written optically [1.39] or electrically [1.40]. Due to their large resistivity changes, GeTe and other chalcogenide glasses have also proven to be promising candidates in Terahertz (THz), RF, as well as optical systems. However, the high loss of GST compounds at the VIS-NIR region, needs to be addressed for a practical application.

The stoichiometry of GeTe compound as well as its deposition conditions have shown to significantly influence the loss and durability of the GeTe films during the phase transitions. Among many different available compositions, $Ge_{50}Te_{50}$ and $Ge_{70}Te_{30}$ have more desirable optical properties and phase transition kinetics. For this reason, $Ge_{50}Te_{50}$ is selected as the reconfigurable optical material in this work. Amorphous $Ge_{50}Te_{50}$ (a-GeTe) has very low extinction coefficient ($k_{am} \sim 0.027$) at the telecommunication wavelength

(1.55 μm). The k value increases by one order of magnitude when the film is transitioned to crystalline phase ($k_{cr} \sim 0.25$) [1.35]. The loss of the material is a significant factor to consider in transmissive devices. The low optical loss of a-GeTe in the NIR regions makes it possible to implement a reconfigurable transmissive device, such as a shutter, or a modulator, with minimum light absorption in the OFF state. The change in the real part of refractive index (n) is also significant (from $n_{am} = 3$ to $n_{cr} = 5$). This change is due the fact that the amorphous phase of GeTe is characterized by the lack of long-range order and periodicity; crystalline GeTe (c-GeTe), however, shows either a rock-salt or metastable trigonal structure based on the temperature of crystallization [1.41]. These large modulations in the n and k values result in a drastic change in the light transmission amplitude, which is another factor to consider when designing optical modulators and shutters. $Ge_{50}Te_{50}$ undergoes phase transitions from its amorphous phase to one of its three major crystalline forms at ~ 200 °C depending on the film thickness and geometry. Crystalline GeTe (c-GeTe) with higher optical loss and conductivity (~ $1\times10^4$ $S.cm^{-1}$) requires higher annealing temperatures to melt the compound ($T_m \sim 700$ °C) to bring it to its initial glassy and resistive amorphous phase. The activation energy for these transitions could be provided by rapid thermal annealing (RTA), electrical joule heating, laser annealing, or applying stress. At the visible and shorter wavelengths of NIR (wavelengths < 1 μm), GeTe possesses very high loss even in the amorphous phase; for example, at

780 nm, $k_{a\text{-}GeTe}$ is ~0.5. Thus, designing any low-loss transmissive-base device at these regions is very challenging.

## 1.3. GeTe-based optical devices: transmissive vs. reflective

GeTe-based optical devices in this work are divided in two main types: transmissive and reflective devices. Transmissive devices can be designed at the regions of the optical spectrum where GeTe has low loss at least in its amorphous phase; thus, the light absorption is minimal when it propagates through the device containing a-GeTe. The light will then be either blocked or modulated when the GeTe is transitioned to the crystalline phase. Reflective devices, on the other hand, can take advantage of the GeTe refractive index modulation at wavelengths where the change in n or k value is considerable. By employing different photonic effects, such as thin-film resonance, multiple reflections within a Fabry–Pérot cavity, and total light reflection (TIR) [1.42], a reflective device can efficiently reflect light back with very low loss at VIS-NIR regions of the spectrum when GeTe is amorphous or crystalline. This reflection then can be minimized when the GeTe is transitioned to the other phase. Therefore, reflective-based devices can offer large modulation of the reflected light despite the very high loss of GeTe at VIS-NIR. Of course, the large modulation of the n value helps to achieve very high contrast in reflective-based GeTe devices as well. This effect is used to implement modulators, shutters, and color filters as discussed further in Chapter 3 and Chapter 4.

## 1.4. Research objectives and contributions

This thesis is focused on the design, implementation, and development of a new class of reconfigurable optical components, which utilize GeTe, with the goal of advancing the state-of the-art in one or more of the device performance specifications. Applications of the devices developed in this work include, but not limited to atomic clocks, low-power displays, and imagers.

The first device discussed in this thesis is a transmissive optical shutter that works in the NIR range. The main performance specification of this device is its ON/OFF transmission ratio, also known as modulation index or contrast. As a proof of concept, we first demonstrate shutters operating at 1550 nm using a transmissive design and utilizing an array of gold lines with sub-wavelength dimensions, filled with GeTe. The design and modeling are performed to achieve efficient phase transition along with desirable optical properties such as high contrast at 1.55 μm (as discussed in Chapter 2). Multi-layer devices consisting of several such sub-wavelength gratings, each separated by a spacer (silicon dioxide layers) are then introduced to enhance the optical modulation index. The fabrication process to achieve multi-layer e-beam lithography is also discussed in detail. All designs were optimized with analytical approaches and finite element modeling (FEM) prior to fabrication. Experimental data demonstrates a very good fit to the modeling results.

Furthermore, use of other metals as the heater and the effect of using GeTe with different stoichiometry on the performance of the devices are also discussed.

As the main application of the shutters in this work is in atomic clock assemblies, in the second design, we targeted the Rubidium (Rb) atom transition wavelength at ~780 nm. For the atomic clock assembly, the shutter needs to have the >70 dB isolation, < 3dB insertion loss, and faster than 1 ms switching speed. Since GeTe has a high optical loss at 780 nm, it is not possible to meet the isolation and loss specification simultaneously in a transmissive shutter approach. Therefore, the device designed for operation at 780 nm is a reflective shutter, employing the high loss of GeTe in a thin-film resonance structure to achieve up to 50 dB of modulation index. This marks the first demonstration of a visible range shutter using phase change materials. A thin layer of silicon dioxide is placed under the GeTe layer to passivate it from the bottom metal layer which serves both as a reflector and a heater element. This passivation enhances the durability of the shutter by reducing the degradation caused due diffusion of metal into GeTe [1.43]. Using refractory metals, such as tungsten (W), Molybdenum (Mo), or platinum, and palladium, can further enhance the device durability owning to the high thermal stability of these metals. The structure and fabrication process of the device are optimized to achieve the highest modulation index or contrast at 780 nm with different metals. Reflection measurements were performed using ellipsometry to validate the simulated data at different wavelengths.

The third and final device discussed in this thesis work is a reconfigurable color reflector working in the visible region to address the need of consumer electronics at visible wavelengths. The main design challenges for color filters include increasing the number of colors addressed in the same pixel, color contrast, and vivacity. To tackle these challenges, we introduced a device structure with multiple thin layers of GeTe, demonstrating the first true tunable color filter using PCMs in the visible range. The light reflections in the visible range with different incident angles were measured using reflective ellipsometry to verify the device colors. Furthermore, the dependency of the phase transition temperature of GeTe on its thickness is studied, for the first time. It was shown that the crystalline transition temperature of GeTe increases as the film thickness decreases. This dependency of crystallization temperature (Tx) to the film thickness is the key that enabled us to achieve a color reflector with four distinct colors by integrating two layers of GeTe. The GeTe layers were individually transitioned between the crystalline and amorphous phase with the same integrated heater for the first time. The color reflector is then integrated with a distributed Bragg reflector (DBR) to achieve more vivid colors and more flexible range of operation wavelengths. The dynamic range of color achieved in this process is presented using different quantitative methods. Such devices are suitable for low refresh rate display systems, such as billboards, with a limited power budget.

In summary, the research contributions of this thesis work are:

- First time demonstration of a transmissive optical shutter using a single layer of GeTe in sub-wavelength grating with more than 14 dB of isolation at 1.55 μm.
- First time demonstration of a transmissive optical shutter that exhibits > 30dB isolation and < 3 dB loss using multi-layers of GeTe patterned using a newly developed fabrication process that includes two steps of e-beam lithography. Using the experimental data from two-layered structure, a five-layered device design has proven to achieve up to 75 dB isolation with less than 3 dB loss. The electrical transitioning of the device is performed using joule heating through an array of gold lines by applying voltage pulses with 2 MHz frequency.
- First time demonstration of a reflective shutter using only 40 nm of GeTe that exhibits the thin film resonance effect and achieves a record high modulation index of 14 dB at 780 nm.
- First time experimental proof of dependency of glass transition temperature of GeTe on its film thickness for GeTe films of less than 20 nm and using this interesting effect to achieve a tunable color filter that shows more than two colors using two layers of GeTe in the same pixel and using the same integrated heater. This device also marks the first demonstration of a truly tunable color filter using phase change materials in the visible range of spectrum.

## 1.5. Organization

This thesis consists of five chapters: In Chapter 1, we discussed the background and motivation of the work, the rationale behind selecting GeTe as the phase change material and provided a summary of its material properties. In this Chapter, we also summarized the research objectives and the contributions of this work. In Chapter 2, a transmissive optical shutter employing sub-wavelength array of gold lines is introduced. Details of the structure, its fabrication process, and measurement results are discussed in detail. The third chapter details the performance analysis of the reflective shutters. We also discuss the fabrication results and compare them against modeling data. The device is cycled for a number of times and the results are included in Chapter 3. In Chapter 4, we present the first tunable color filter which uses GeTe to achieve multiple colors. The color of the reflected light is quantified by using ellipsometry. The reflection amplitude is extracted for visible wavelengths and then converted using International Commission on Illumination standard to demonstrate the quantitative colors. The dependency of the GeTe glass transition temperatures on its thickness is studied to achieve selective phase transitioning and multiple colors by employing a single heater element. Finally, In the last chapter, we propose possible future work directions. We discuss methods to improve the reliability of the devices by proposing improvements to the structure of the device, processing steps, and even using other chalcogenide glasses. We also include a new tunable color filter design

using multiple sub-wavelength gratings of GeTe with different periods and filling ratios to achieve a larger number of colors in the same pixel. While this thesis work provides a number of proof-of-concept demonstrations to show that phase change materials can be used to implement tunable optical devices at visible to near IR range, there are many other devices that one can develop using a similar structure or platform as what is shown in this work. These tunable optical components can find numerous applications in a number of sectors from consumer electronics and commercial market to space.

## 1.6. References


[1.1] Humar, M., and Muševič, I. (2010). 3D microlasers from self-assembled cholesteric liquid-crystal microdroplets. Optics express, 18(26), 26995-27003.

[1.2] Araki, S., Nakamura, K., Kobayashi, K., Tsuboi, A., and Kobayashi, N. (2012). Electrochemical optical-modulation device with reversible transformation between transparent, mirror, and black. Advanced Materials, 24(23), OP122-OP126.

[1.3] Reed, G. T., Mashanovich, G., Gardes, F. Y., and Thomson, D. J. (2010). Silicon optical modulators. Nature photonics, 4(8), 518.

[1.4] Pospischil, A., Humer, M., Furchi, M. M., Bachmann, D., Guider, R., Fromherz, T., and Mueller, T. (2013). CMOS-compatible graphene photodetector covering all optical communication bands. Nature Photonics, 7(11), 892.

[1.5] Rajagopal, S., Roberts, R. D., and Lim, S. K. (2012). IEEE 802.15. 7 visible light communication: modulation schemes and dimming support. IEEE Communications Magazine, 50(3), 72-82.

[1.6] Papp, S. B., Beha, K., Del'Haye, P., Quinlan, F., Lee, H., Vahala, K. J., & Diddams, S. A. (2014). Microresonator frequency comb optical clock. Optica, 1(1), 10-14.

[1.7] https://www.techrepublic.com; https://www.nikonusa.com .

[1.8] Clark, J., & Lanzani, G. (2010). Organic photonics for communications. Nature photonics, 4(7), 438..

[1.9] Newman, Z. L., Maurice, V., Drake, T., Stone, J. R., Briles, T. C., Spencer, D. T., ... & Shen, B. (2019). Architecture for the photonic integration of an optical atomic clock. Optica, 6(5), 680-685..

[1.10] Shah, V., Lutwak, R., Stoner, R., & Mescher, M. (2012, May). A compact and low-power cold atom clock. In 2012 IEEE International Frequency Control Symposium Proceedings (pp. 1-6). IEEE..

[1.11] Cai, H., Xu, K. J., Liu, A. Q., Fang, Q., Yu, M. B., Lo, G. Q., & Kwong, D. L. (2012). Nano-opto-mechanical actuator driven by gradient optical force. Applied Physics Letters, 100(1), 013108.

[1.12] Gavartin, E., Braive, R., Sagnes, I., Arcizet, O., Beveratos, A., Kippenberg, T. J., & Robert-Philip, I. (2011). Optomechanical coupling in a two-dimensional photonic crystal defect cavity. Physical review letters, 106(20), 203902.

[1.13] Weis, S., Rivière, R., Deléglise, S., Gavartin, E., Arcizet, O., Schliesser, A., & Kippenberg, T. J. (2010). Optomechanically induced transparency. Science, 330(6010), 1520-1523.

[1.14] Liu, M., Yin, X., Ulin-Avila, E., Geng, B., Zentgraf, T., Ju, L., ... & Zhang, X. (2011). A graphene-based broadband optical modulator. Nature, 474(7349), 64.

[1.15] Vasudev, A. P., Kang, J. H., Park, J., Liu, X., & Brongersma, M. L. (2013). Electro-optical modulation of a silicon waveguide with an "epsilon-near-zero" material. Optics express, 21(22), 26387-26397.

[1.16] Melikyan, A., Alloatti, L., Muslija, A., Hillerkuss, D., Schindler, P. C., Li, J., ... & Chen, B. (2014). High-speed plasmonic phase modulators. Nature Photonics, 8(3), 229.

[1.17] Hossein-Zadeh, M., & Vahala, K. J. (2009). An optomechanical oscillator on a silicon chip. IEEE Journal of selected topics in Quantum Electronics, 16(1), 276-287.

[1.18] Shalin, A. S., Ginzburg, P., Belov, P. A., Kivshar, Y. S., & Zayats, A. V. (2014). Nano-opto-mechanical effects in plasmonic waveguides. Laser & Photonics Reviews, 8(1), 131-136.

[1.19] Lueder, E. (2010). Liquid crystal displays: addressing schemes and electro-optical effects. John Wiley & Sons.

[1.20] Guarino, A., Poberaj, G., Rezzonico, D., Degl'Innocenti, R., & Günter, P. (2007). Electro–optically tunable microring resonators in lithium niobate. Nature photonics, 1(7), 407.

[1.21] Martinez, S., Hernández, L., Reyes, D., Gomez, E., Ivory, M., Davison, C., & Aubin, S. (2011). Note: Fast, small, and low vibration mechanical laser shutters. Review of Scientific Instruments, 82(4), 046102.
[1.22] Phare, C. T., Lee, Y. H. D., Cardenas, J., & Lipson, M. (2015). Graphene electro-optic modulator with 30 GHz bandwidth. Nature Photonics, 9(8), 511.
[1.23] Ghorbani-Asl, M., Borini, S., Kuc, A., & Heine, T. (2013). Strain-dependent modulation of conductivity in single-layer transition-metal dichalcogenides. Physical Review B, 87(23), 235434.
[1.24] Schwierz, F. (2013). Graphene transistors: status, prospects, and problems. Proceedings of the IEEE, 101(7), 1567-1584.
[1.25] Geng, Y., Brogueira, P., Figueirinhas, J. L., Godinho, M. H., & Almeida, P. L. (2013). Light shutters from nanocrystalline cellulose rods in a nematic liquid crystal. Liquid Crystals, 40(6), 769-773.
[1.26] Cao, J., Ertekin, E., Srinivasan, V., Fan, W., Huang, S., Zheng, H., ... & Wu, J. (2009). Strain engineering and one-dimensional organization of metal–insulator domains in single-crystal vanadium dioxide beams. Nature nanotechnology, 4(11), 732.
[1.27] Aetukuri, N. B., Gray, A. X., Drouard, M., Cossale, M., Gao, L., Reid, A. H., ... & Roche, K. P. (2013). Control of the metal–insulator transition in vanadium dioxide by modifying orbital occupancy. Nature Physics, 9(10), 661.
[1.28] Kikuchi, H., Yokota, M., Hisakado, Y., Yang, H., & Kajiyama, T. (2002). Polymer-stabilized liquid crystal blue phases. Nature materials, 1(1), 64.
[1.29] Pernice, W. H. P., Bhaskaran, H. (2012). Photonic non-volatile memories using phase change materials. Applied Physic Letters, 101(17).
[1.30] H. P. Wong, S. Raoux, S. B. Kim, J. Liang, J. P. Reifenberg, B. Rajendran, M. Asheghi, and K. E. Goodson, Proc. IEEE 98, 2201–2227 (2010).
[1.31] Kolobov, A. V., Fons, P., Frenkel, A. I., Ankudinov, A. L., Tominaga, J., & Uruga, T. (2004). Understanding the phase-change mechanism of rewritable optical media. Nature materials, 3(10), 703.
[1.32] Lee, S. H., Jung, Y., & Agarwal, R. (2007). Highly scalable non-volatile and ultra-low-power phase-change nanowire memory. Nature nanotechnology, 2(10), 626.
[1.33] El-Hinnawy, N., Borodulin, P., Wagner, B., King, M. R., Mason, J. S., Jones, E. B., & Howell, R. S. (2013). A four-terminal, inline, chalcogenide phase-change RF switch using an independent resistive heater for thermal actuation. IEEE Electron Device Letters, 34(10), 1313-1315.
[1.34] Hosseini, P., Wright, C. D., & Bhaskaran, H. (2014). An optoelectronic framework enabled by low-dimensional phase-change films. Nature, 511(7508), 206.
[1.35] Gholipour, B., Zhang, J., MacDonald, K. F., Hewak, D. W., & Zheludev, N. I. (2013). An all-optical, non-volatile, bidirectional, phase-change meta-switch. Advanced materials, 25(22), 3050-3054.
[1.36] Bahl, S. K., & Chopra, K. L. (1969). Amorphous versus crystalline GeTe films. II. Optical properties. Journal of Applied Physics, 40(12), 4940-4947.
[1.37] Weidenhof, V., Pirch, N., Friedrich, I., Ziegler, S., & Wuttig, M. (2000). Minimum time for laser induced amorphization of Ge2Sb2Te5 films. Journal of Applied Physics, 88(2), 657-664.
[1.38] Qureshi, M. K., Srinivasan, V., & Rivers, J. A. (2009, June). Scalable high performance main memory system using phase-change memory technology. In ACM SIGARCH Computer Architecture News (Vol. 37, No. 3, pp. 24-33). ACM.
[1.39] Huang, H., Li, S., Zhai, F., Wang, Y., Lai, T., Wu, Y., & Gan, F. (2011). Picosecond laser pulse-driven crystallization behavior of SiSb phase change memory thin films. Materials Chemistry and Physics, 128(3), 405-409.

[1.40] Wang, W. J., Shi, L. P., Zhao, R., Lim, K. G., Lee, H. K., Chong, T. C., & Wu, Y. H. (2008). Fast phase transitions induced by picosecond electrical pulses on phase change memory cells. Applied Physics Letters, 93(4), 043121.
[1.41] T. Okabe and M. Nakagawa, "Crystallization behavior and local order of amorphous GexTe1-x films," J. Non. Cryst. Solids 88, 182–195 (1986).
[1.42] Yeh, P. (1988). Optical waves in layered media (Vol. 95). New York: Wiley.
[1.43] Lu, L., Dong, W., Behera, J. K., Chew, L., & Simpson, R. E. (2019). Inter-diffusion of plasmonic metals and phase change materials. Journal of materials science, 54(4), 2814-2823.

# Chapter 2: Optical Shutter with Integrated Heater

Fast and configurable photonic components are needed in a variety of applications spanning from intensity modulation in atomic clock assemblies [2.1, 2.2], quantum communication in satellites [2.3], beam steering in autonomous vehicles [2.4] to phase and polarization shaping in filters and lenses [2.5, 2.6]. This configurability comes either from movable elements (e.g. micro-mirrors in a phase array structures [2.7]) or use of an actively tunable optical material such as a liquid crystal [2.8, 2.9] or a PCM [2.10]. As discussed in the previous chapter, some of the commonly used materials for electro-optical systems are GeTe, GST, and $VO_x$, showing modulation in their optical and electrical properties in response to structural or electrical changes [2.11]. Unlike mechanical modulators, electro-optical modulators are less bulky, introduce lower noise, and consume less power. Since there is no suspended structure within electro-optical modulators, the yield, reliability, and durability of such devices are also significantly higher than their mechanical counterparts. However, they provide lower contrast compared to that of mechanical modulators due to material limitations. Mechanical modulators, on the other hand, suffer from slow switching speeds (~100s of microseconds) and require constant power to maintain their "ON" state. This is also the case in common electro-optical modulator such as those based on $VO_x$ and LCs. LCs are some of the most popular materials used in electro-optical modulators at NIR and visible regions. LC modulators offer a higher contrast compared to other electro-optical

counterparts [2.12]. LC modulators operate by switching between planar and focal conic textures in response to an applied electric field [2.13, 2.14]. LC-based devices such as polarizers and displays have shown superior performances at the IR and visible wavelengths [2.15]. However, LC modulators are very sensitive to temperature variations and the angle of incident light, lowering the stability and reliability of such modulators in harsh environments, especially in space applications [2.16]. PCMs, on the other hand, can provide the stability needed for application in harsh environments with minimal power requirements. This chapter starts with studying the structure and modeling used to make an electro-optical shutter or modulator based on a PCM (*i.e.* GeTe). This GeTe-based optical shutter shows the highest demonstrated switching speed, highest reported modulation contrasts, and easy integration with CMOS circuitry. Fabrication challenges of making a shutter consisting of multiple layers of sub-wavelength gratings to increase the contrast is discussed in details. The fabrication process of the multi-layer device can be applied to implement other electrical or optical components. Material characterizations and experimental results of the shutter are presented showing a great match to the modeling results. Next part focuses on characterization of the GeTe refractive index for both amorphous and crystalline, which is followed by the theory and structure of the transmission-based optical shutter.

## 2.1. Characterization of the optical refractive index of the GeTe film in amorphous and crystalline phases

The experimental value of the refractive index of the GeTe is not well studied within the literature for visible and NIR regions. To more accurately design the shutter, we extracted the real and imaginary parts of the refractive index (the n and k values) for both a-GeTe and c-GeTe using ellipsometry from a GeTe film with a thickness of 130 nm (Figure 6). To do so, the change in the amplitude ratio (tan (Ψ)) and phase shift (Δ) are extracted from measurement of the reflection and transmission of the linearly polarized light at different angles [2.17, 2.18]. To acquire enough data for modeling the optical properties, the sample is illuminated at three different angles of incidence (65°, 70°, and 75°) with a spectral range of 0.7 eV to 3 eV. A Cauchy model could be used for transparent films to extract the optical refractive indices. However, since amorphous GeTe has higher loss at visible wavelengths and is not considered fully transparent, a Basis-Spline (B-Spline) model is used to fit to the experimental tan (Ψ) and Δ values as well as the transmission amplitude for the entire range of visible and NIR regions. This measurement also consists of a back-side reflection correction method for the glass substrate for more accuracy. The reduced number of fitting parameters makes this method easier to use for semi-transparent films. A roughness value of 5 nm is added to the model to achieve the best possible fitting. The fitting for the crystalline film is more complicated especially

when the thickness of the film is larger than 100 nm. This is due the fact that the phase transitioning of the GeTe is not uniform throughout the thickness of the film. As the film gets thicker, the crystallization process using a convection oven gets harder and less reliable. With thicker than 100 nm films, several layers throughout the thickness with different levels of crystallizations are formed, which have very different refractive index values. Thus, to achieve the best fitting for the optical refractive index values, a graded model is used for the c-GeTe films. Here, a five-layer model is used with different refractive indices trough the thickness of the c-GeTe with the highest index being closer to the substrate as it experiences full crystallization. A graded refractive index model is used as shown in Figure 7. The model shows that the highest degree of crystallization happens near the silicon substrate due to a better conductive heating. The refractive index of the film then drops to its minimum value and eventually increases as we get closer to the surface of the film. This is due to the fact that the oven-based crystallization provides better heating on the surface of the film compared to the areas in higher depth. The amorphous refractive index of the film is extracted from the as-sputtered film which has a uniform phase. Moreover, to examine the phase transition condition of GeTe, we used an annealing process to heat the crystallized GeTe films to ~800 ˚C and quenched it by natural convection cooling (shown in Figure 9). However, it is important to mention that the amorphization of the thick GeTe film in an oven-based heating method is very hard if not impossible. This is another reason that to achieve multiple reversible transitions, we used

the Joule-heating approach through the rest of this thesis work to provide a more efficient heating and cooling process. The thicknesses of the GeTe films are maintained to be less than 60 nm in later designs to achieve more uniform and full transitions. Transmission-based devices, which are discussed in this chapter, however, can have thicker films thanks to the use of integrated metal grating heaters in between the GeTe gratings or patches.

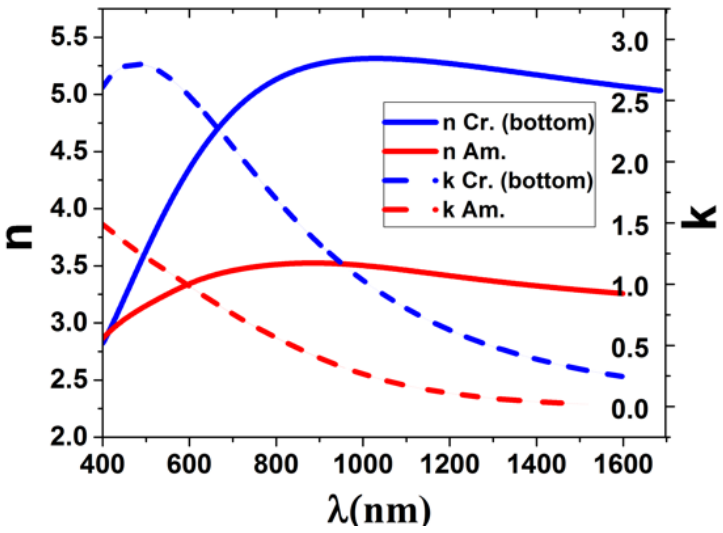


Figure 6. Optical refractive index of GeTe as a function of wavelength for amorphous and crystalline phases in the Visible and Near-IR frequency ranges. Data derived using Ellipsometry measurement from an as deposited amorphous film of 130 nm.

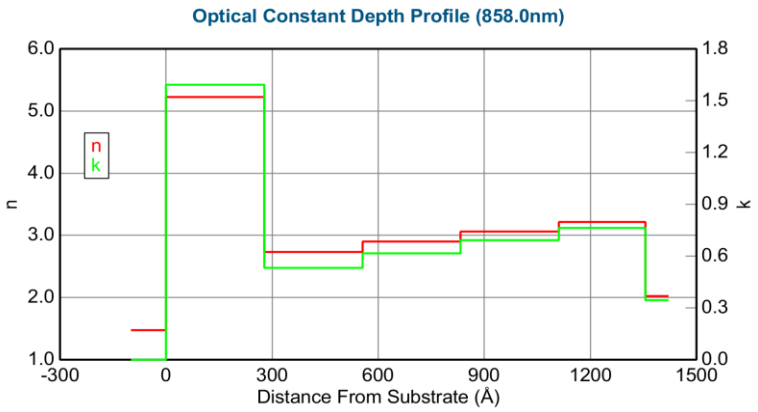


Figure 7. Modeled graded optical refractive index of c-GeTe for visible and NIR wavelengths based on experimental data, which is derived from ellipsometry measurement through the thickness of a 130 nm film. The GeTe film is crystallized using a convection oven from the as-deposited amorphous phase.

## 2.2. Basics and Structures

The transmissive shutter structure consists of a sub-wavelength metal grating, filled with GeTe (Figure 8). The grating structure supports two different optical resonance modes. These resonances are called surface plasmon polariton (SPP) and slit mode with low and high transmissivity, respectively [2.19, 2.20]. The same metal grating is also used as a nano-heater, which reduces the device area and simplifies the fabrication process compared to a grating-based device with a separate heater. Such integrated heater also provides a more effective heating approach compared to those of a bulk heater or direct heating approaches due to its proximity to the GeTe and localized heating profile [2.21].

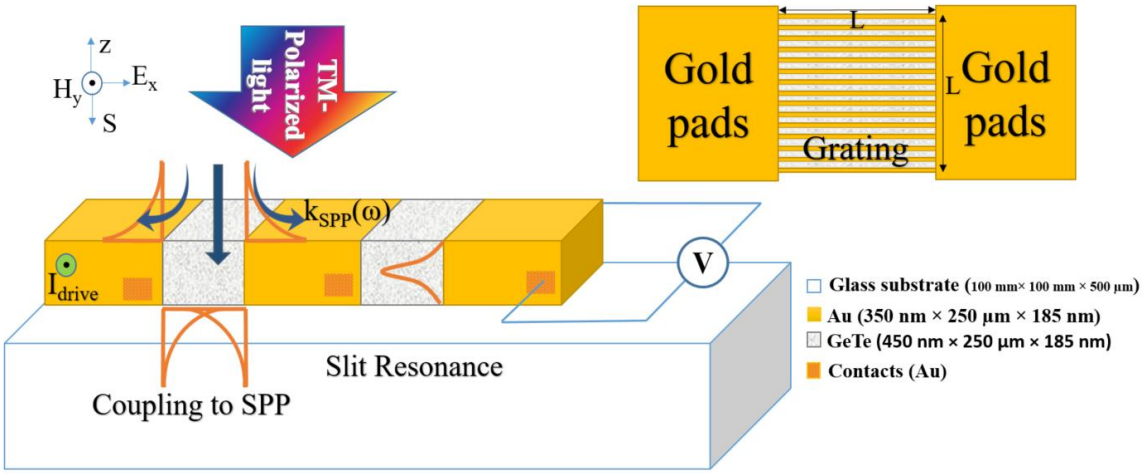


Figure 8. Schematic of shutter consisting of an array of gold lines filled with GeTe (grey parts in the figure). Figure is not drawn to scale.

Since the resistivity of gold lines is low, voltage pulses with the amplitude of 6.5 V and a 500 ns duration can be used for amorphization of a device with the following array dimensions: array pitch = 450 nm, filling ratio = 60%, array thickness = 200 nm, and total area = 500 µm × 500 µm. On the other hand, applying a voltage pulse with 1.25 V amplitude and 5 µsec period-crystallizes the GeTe in the same device (Figure 9). The voltage amplitude and pulse duration depend on the volume of the GeTe, the dimension of the grating, the material that is used as the heater, and the thermal boundary condition between the heater and the GeTe [2.22].

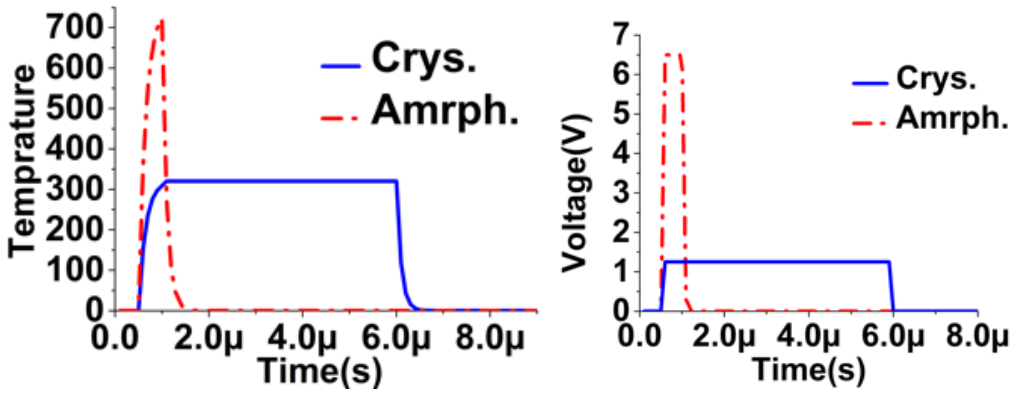


(a) (b)

Figure 9. (a) Annealing profile for crystallization (blue) and amorphization (red) of GeTe (b) applied pulses.

The inset of Figure 8 demonstrates intuitively how we employed the gold sub-wavelength grating as the heater to change the phase of the GeTe. There are two pads on either side of the gold lines, which are used to apply the Joule heating voltage pulses through the gold lines. The two main resonances of the metallic array are also shown in Figure 8. As shown here, the same array of gold lines can help to excite the SPP, which is utilized to improve the optical modulation contrast by improving the quality factor (Q-factor) of the slit resonance. The so-called slit resonance mode is positioned at the wavelength of 1.55 µm by tuning the thickness of the gold array for the a-GeTe and matching the grating to its top air interface and bottom glass substrate; this allows the transverse magnetic (TM) polarized light to pass through the structure at normal incident angle. The SPP mode, on the other hand, is excited at 1.1 µm for both a-GeTe and c-GeTe

and enhance the Q-factor of the slit mode when the GeTe is amorphous. The slit mode is moved to longer wavelengths (> 2 μm) when GeTe is transitioned to the crystalline state. This crystallization causes a large absorption at 1.55 μm due to the proximity of the SPP resonance that is located at 1.1 μm.

## 2.3. Modeling

Metal gratings have gained considerable interests in the recent two decades with the advancement of the nano-technology and lithography systems. Numerous integrated devices such as Bragg reflectors [2.23], waveguides [2.24], and filters [2.25], are introduced at the visible and IR regions, which operate based on the SPP excitation. The metallic grating is one of the easiest configurations to excite SPP quasi-particles, when a TM polarized light interacts with free electrons in the metal-dielectric interface. The SPP quasi-particles are responsible for extraordinary absorption of TM polarized light that is incident at a metallic array of holes or lines (Wood's anomaly) at a certain angle [2.26, 2.27]. The wave vector at which the light interact with the SPP resonance is derived from the Maxwell's equations:

$$k_z = \frac{\omega}{c}\sqrt{\frac{\varepsilon_m \varepsilon_d}{\varepsilon_m + \varepsilon_d}}, \tag{2-1}$$

where $\omega$ is the angular frequency, $c$ is the speed of the light in the vacuum, and $\varepsilon_d$is the permittivity of the dielectric. $\varepsilon_m$ is also the permittivity of the metal with a dispersion that is defined based on the Drude model [2.28]:

$$\varepsilon_{Au}(\omega) = \varepsilon_\infty - \frac{\omega_p^2}{\omega(\omega+i\gamma\omega)}, \tag{2-2}$$

Here $\omega_p$ is the plasma frequency of the SPPs, and $\gamma$ and $\varepsilon_\infty$ are the damping factor and the limit factor at the higher frequencies, respectively, which are extracted during the fitting of the optical properties of the metal. In order to excite the SPP resonance at a specific frequency and angle, the wavenumber of the surface plasmon polariton and that of the incident light need to be matched. The resulting SPP resonance shows itself in the form of dips in the transmission spectra of the incident light (Wood's anomaly).

The light reflection is almost identical for lossy or perfect metals for frequencies lower than the plasma frequency of the metal (e.g., frequencies < 300 THz for the gold [2.28]), where the dispersion is limited. Thus, the simpler equation of a perfect conductor can be used for the case of the gold at visible-NIR regions. This allows to model each layers of grating with an effective impedance, which depends on the refractive index of the materials that are used to form such a grating. The top air and the bottom layer that is sitting directly beneath the grating is also modeled with an effective impedance value. Such effective impedance value is simply the ratio of the electric to the magnetic field such that:

$$Z_l = \frac{E}{H} = \sqrt{\frac{\mu}{\epsilon}} = \sqrt{\frac{\mu_r \mu_0}{\epsilon_r \epsilon_0}} = \eta Z_0 \ , \tag{2-3}$$

where $Z_0$ is the effective impedance of the vacuum (or the air) and is equal to 377 Ω. To achieve the maximum transmission at the position of the slit resonance, the reflection coefficient of the light should be minimized at the surface of the grating:

$$\Gamma = \frac{Z_G - Z_0}{Z_G + Z_0} \, , \tag{2-4}$$

where $Z_G$ is the effective impedance, which is seen from the surface of the grating. The $Z_G$ value is derived from the refractive indices of the materials that are used within the grating and also all the layers that are underneath the grating. To calculate the $Z_G$, first, a model is needed to derive the effective refractive index of the grating. There are many models for the effective refractive index of the metallic grating based on a PEC model [2.20, 2.29]. Here a simple model [2.29] is used, which provides enough accuracy for an initial analytical design. This model calculates the effective refractive index of the metal grating that is filled with air. Refractive index of a grating with a period of "d" and a slit width of "a" is then equal to (these dimensions are shown Figure 10):

$$n_{eff} = \frac{1}{\sum_{-\infty}^{+\infty} \frac{a}{d} \sin c(m\pi \frac{a}{d}) \frac{1}{\sqrt{1-(m\frac{\lambda}{d})^2}}} \ . \tag{2-5}$$

As mentioned above, this model assumes the slits are filled with air which is different than the design where GeTe is filling the slits. However, by using this model a good match between the index of the grating layer to its top air and bottom glass layers is achieved to

maximize the transmission. This is further improved with the FEM simulations for the case of the GeTe-filled slits.

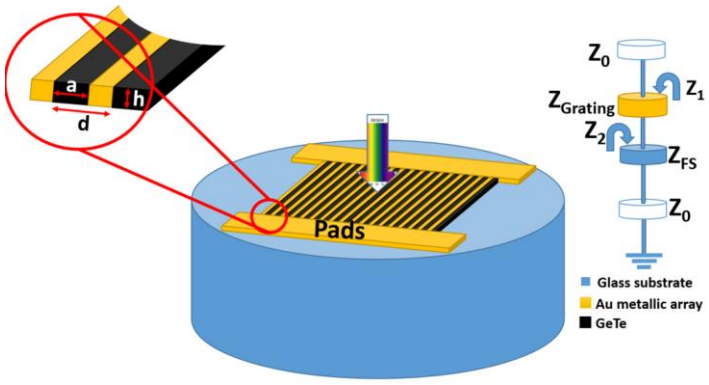


Figure 10. Left: Single layer of gold grating slits filled with GeTe; Right: The impedance model of the structure based on transmission line theory.

Due to the variation of the refractive index of the GeTe within the visible-NIR region, the effective refractive index needs to be calculated for each wavelength separately which is very time-consuming. It is worth mentioning that due to such dispersion of the refractive index of the GeTe at the visible and NIR, the matched slit resonance for a gold/GeTe grating has a higher Q-factor when compared to that of an air-filled grating. Finally, the input impedance from the surface of the grating can be derived from:

$$Z_G = \eta_{eff} \frac{Z_{sio} + \eta_{eff} \tanh(k_{eff} t_{eff})}{\eta_{eff} + Z_{sio} \tanh(k_{eff} t_{eff})} \quad , \tag{2-6}$$

which is used to minimize the reflection coefficient that is discussed earlier in the equation (2-4); The $\eta_{eff}$, $k_{eff}$, and $t_{eff}$ in (2-6) are the grating parameters, which are defined as:

$$\eta_{\mathrm{eff}} = n_{\mathrm{eff}} Z_0, k_{\mathrm{eff}} = \frac{\omega}{c} = n_{\mathrm{eff}} \frac{\omega}{c_0} = n_{\mathrm{eff}} k_0, t_{\mathrm{eff}} = \frac{d}{a}. \quad (2\text{-}7)$$

Here, $k_0$ is the free-space wavevector of the light and $Z_{sio}$ can also be found similarly from

$$Z_{\mathrm{sio}} = \eta_{\mathrm{sio}} \frac{Z_0 + \eta_{\mathrm{sio}} \tanh(k_{\mathrm{sio}} t_{\mathrm{sio}})}{\eta_{\mathrm{sio}} + Z_0 \tanh(k_{\mathrm{sio}} t_{\mathrm{sio}})}, \quad (2\text{-}8)$$

where $\eta_{sio}$, and $k_{sio}$ are defined similar to those in equation (2-7) and $t_{sio}$ is the thickness of the glass substrate underneath the grating. With the thickness, period, and slit size being optimized, the grating can be matched to the top and bottom air with minimum reflection. This obviates the need of the separate anti-reflection coating and simplifies the fabrication process.

Non-reflective grating can also be designed based on half-wavelength ($t_{eff} = r\,\lambda_0/2$) or quarter-wavelength ($t_{eff} = (2r+1)\,\lambda_0/4$) impedance matching approaches; $\lambda_0$ is the wavelength of light in vacuum, $t_{eff}$ is the effective thickness of the grating and $r$ is an integer number. Since the refractive indices of air and the substrate are not equal, we have to use quarter-wavelength matching, which dictates that the $n_{eff} = \sqrt{n_0 n_{Silica}}$ and $t_{eff} = \lambda_0/4n_{eff}$. These equations yield to the value of 1.204 and 195 nm for the effective refractive index and the effective thickness of the grating, respectively. These values are

further improved for the case of the GeTe-filled slits by using FEM to minimize the total reflection at the desired wavelength.

A unit cell of grating is modeled in the COMSOL® FEM tool by defining the Floquet periodicity condition and extract the far-field reflection of the linearly polarized light. The Drude model for the permittivity of the gold as well as the experimentally measured refractive indices of the a-GeTe and c-GeTe are also imported in the model for a more accurate design. The transmission of the TM-polarized light through the grating at the normal incidence is shown in Figure 11 for the case of the GeTe-filled gratings in the amorphous phase. The initial theoretical design is then optimized to maximize the transmission of the light at 1.55 μm wavelength with the a-GeTe inside the slits. As shown in Figure 11, an SPP dip also exist at 1.1 μm, which enhances the Q-factor of the slit resonance by reducing the out-of-band transmission power. Moreover, since the impedance matching is only optimized at 1.55 μm, the out-of-band transmission value is lower when compared to the slits that are filled with a material with a constant refractive index at visible and NIR wavelengths. The transverse magnetic field ($H_Z$) and orthogonal electric field ($E_y$) fields, which are shown in the inset of the Figure 11, proves the existence of the slit and SPP resonance modes and their effect on the transmission of the light transmission for the amorphous phase of the GeTe. The light transmission result is then plotted in Figure 12 for both phases of the GeTe film in the logarithmic scale.

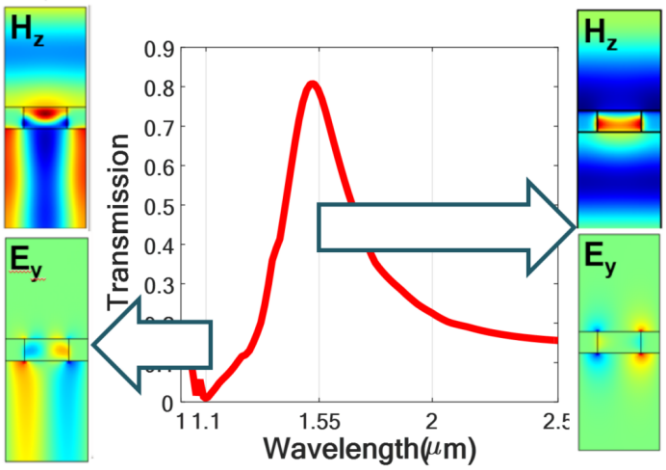


Figure 11. Modeled transmission of the gold grating filled with amorphous GeTe at NIR regions; inset shows the transverse H and orthogonal E fields at the position of the SPP (dip) and slit (peak) resonances for a grating with d=450 nm, a= 400 nm and $t=\lambda/4n_{eff}$.

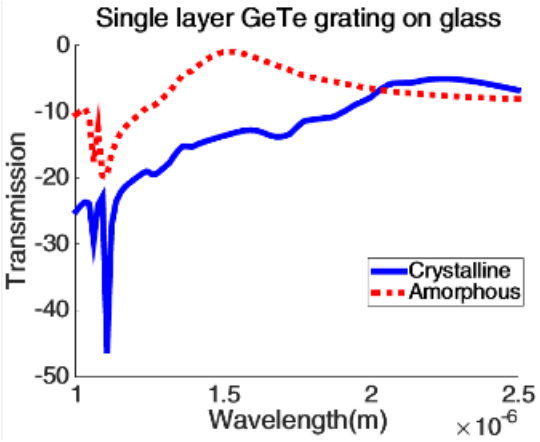


Figure 12. Transmission value of a single-grating layer shutter for both amorphous and crystalline phases of the GeTe in logarithmic scale.

## 2.4. Fabrication process and results for single layer shutter

The shutter is fabricated on a 515 µm thick borosilicate glass (Borofloat 33®) wafer from planoptik. A JEOL JBX-6300FS e-beam lithography system (JEOL Ltd.) is used to pattern the 950PMMa resist. The proximity and dose correction are performed prior to writing the pattern to achieve the most accurate dimensions and vertical sidewalls. The exposed resist is then developed in the 1:3 MIBK to IPA solution. Then a gold film with the thickness of 185 nm is deposited on top of the resist and the lift-off process with ultrasonic source is used to pattern the gold lines. The period of the grating is measured to be 450 nm period with a 200 nm slit opening (see the scanning electron microscope (SEM)

image of the device shown in Figure 13). Then, GeTe is sputtered on top the gold grating using a Kurt J. Lesker Lab-018 sputtering system at a rate of 0.833 Å/s from a 3-inch GeTe target (Mitsubishi Materials Corporation). The AC power is set to 60 W with 4.5 mT of chamber pressure for 60 sec to achieve a 100 nm thick amorphous GeTe film. The RC time constant for the structure is calculated and modeled using the thermal conductivity of gold, glass wafer, and assuming convection cooling. The required cool-down time for the structure is less than the amorphization pulse width, which is 1 μsec.

The voltage pulses provide the required heat to transition the GeTe patches in between the gold lines. The crystallization pulse has a 1.25 V amplitude and 5 μs period. The amorphization pulse, however has a shorter pulse width of 500 ns and 6.5 V amplitude.

The device is then mounted on a Fourier transform infrared spectroscopy (FTIR) system to measure the transmission of the light at normal incidents. A Perkin-Elmer Spectrum GX system is used along with a microscopic mountable polarizer at the NIR region. The Figure 14 shows the transmission of the TM-polarized light for both phases of GeTe at the room temperature. It is also important to mention that the objective that is used inside the microscopic mount of the FTIR system causes a blue shift in the wavelength of the SPP resonance due to the oblique angle of incident of the incoming light.

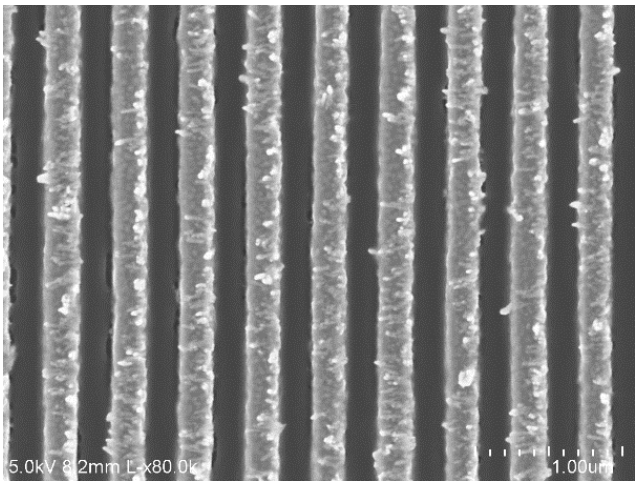


Figure 13. A top view SEM image of the shutter fabricated on glass (Period ≈ 450 nm and opening ≈ 40 nm, respectively). The sample is imaged by using a proprietary conductive liquid, which was coated on the surface of the device to reduce the charging effect and the blurriness.

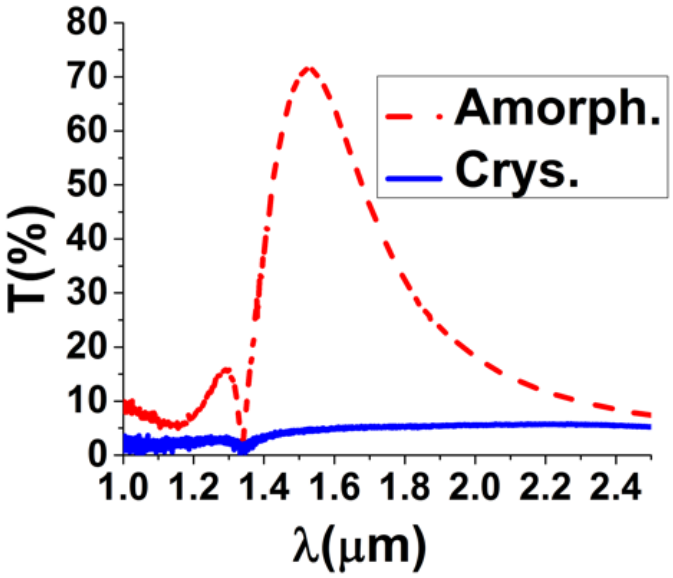


Figure 14. Measured transmission of the shutter vs. wavelength at the NIR regions for both a-GeTe (red) and c-GeTe (blue) by using FTIR spectroscopy [2.30].

## 2.5. Multi-layer transmissive shutter

As mentioned before, the contrast of the electro-optical shutter is the main limit when compared with the mechanical shutters. To enhance the contrast of the single layer PCM-based optical shutter that is presented in the previous part, a multi-layer device is made by stacking several gold gratings- filled with the GeTe film. The optical modes of each of these layers of the gratings have to match to maximize the transmission of the light at the desired wavelength (1.55 μm).

### 2.5.1. Design and modeling

The SPP modes for two layers of grating are shown in the cross-section view of the device in Figure 15(a). There is a thick silicon nitride ($Si_3N_4$) passivation layer between each layer of the gratings, which also ease the fabrication process of the multi-layer shutter. This nitride separator withstands high heat required when each of the GeTe-filled gratings undergoes phase transitions, selectively by applying the joule heating to the corresponding pads. Moreover, it has high chemical and mechanical resilience when it undergoes the harsh chemical and mechanical polishing process that is required by the e-beam lithography preparation steps. As discussed above, a single array of metallic lines with a period $d$ supports two different resonance: 1) the slit resonance, which has higher transmission of the light and a propagation constant of $\beta \approx 2\pi/d$ and 2) the SPP mode with propagation constant of $\beta \approx \pi/d$ (see in Figure 15(a)). The effective refractive index ($n_{eff}$) of the sub-wavelength ($\lambda/3$) metallic line array can be estimated by equation (2-5) and is used to impedance match each layer of gratings to achieve the maximum transmission of the light at 1.55 μm. The simplified characteristic impedance of each layer is then determined by:

$$Z_i = \frac{\eta_0}{\sqrt{n_i^2 - k_i^2}}, \tag{2-9}$$

where $n_i$ and $k_i$ are the refractive index and extinction coefficient of each of the layers, respectively. $\eta_0$ is the characteristic impedance of the vacuum (~377 Ω). The total

reflection coefficient of the stack can be minimized by matching each layer to the top and bottom layers.

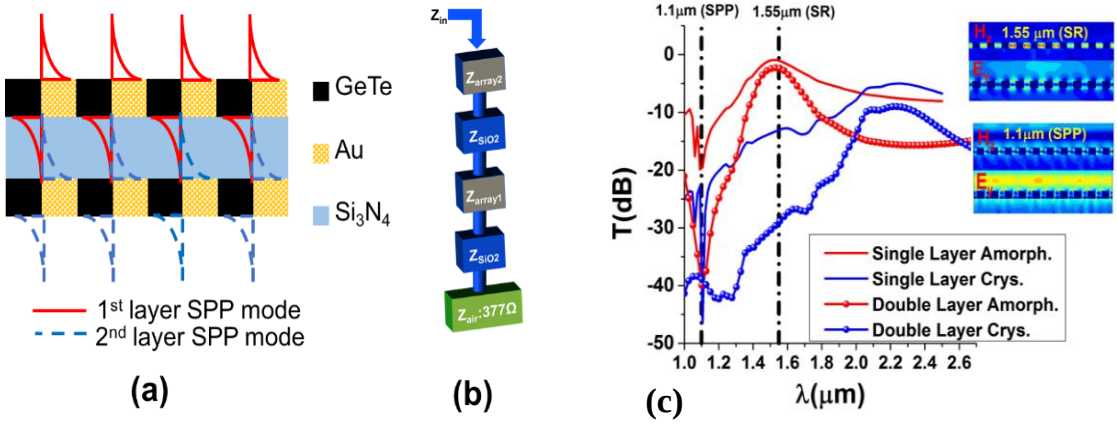


Figure 15. (a) Multi-layer grating with a $Si_3N_4$ separator, which shows the SPP resonance modes (in red for the first layer and blue for the second layer). (b) The equivalent circuit, which shows the characteristic impedance of each layers. (c) Modeled transmission of the TM-polarized light from a single- and a double-layer device for both a-GeTe and c-GeTe. Insets show magnetic field (Hz) and electric field (Ez) at the wavelength of the slit resonance (SR) ($\lambda_{SR}$= 1.55 μm) and SPP resonances ($\lambda_{SPP}$= 1.1 μm).

As shown in Figure 15(b) the equivalent circuit is used to minimize the total reflection of the light from the surface of the device at 1.55 μm. Matching each layer from top to bottom, uniquely determines the array thickness and gold width for each layer, which were kept constant at 190 nm and 150 nm, respectively, for a simpler process. The impedance matching provides the minimum reflection at 1.55 μm for slits that are filled with

amorphous GeTe as shown in Figure 15 (c). Crystallization of the GeTe, on the other hand, cause a large impedance mismatch at this wavelength and thus reduces the transmission of the light. Moreover, the higher loss (higher k value) of the c-GeTe improves the modulation index with a higher isolation (at the ON state of the shutter). Light coupling to the SPP also helps to increase the isolation by enhancing the Q-factor of the resonance at 1.55 μm. Figure 16 shows how the modulation index of the light transmission is enhanced with cascading up-to five layers of the grating with a glass spacers in between each two grating layers. This five-layer device shows a significantly higher isolation of the light (>75 dB) for the c-GeTe and only a 3 dB-loss for the a-GeTe when the impedance matching approach is employed at 1.55 μm. A thin silicon dioxide or silicon nitride separator is also considered in the impedance matching technique of each layers of the gratings. Assuming a value of 1.45 for the refractive index of glass and 1.204 for the first layer of the grating, the effective refractive index of the second layer needs to be equal to 1.74 for maximum transmission. The last layer of the grating must be matched to the thick bottom glass substrate, which yields a similar value of 1.204 for the effective refractive index of the bottom grating that is sitting directly on top of the glass substrate.

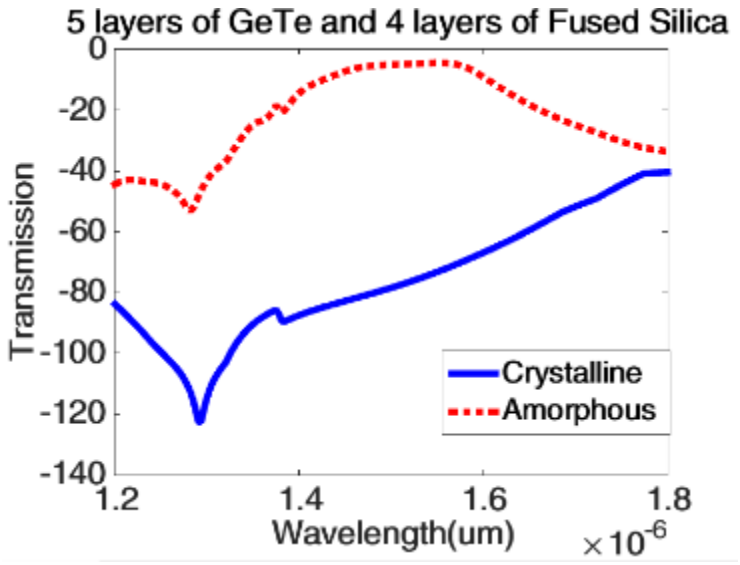


Figure 16. Transmission response of a shutter consisting of five layers of GeTe-filled grating arrays in crystalline and amorphous phases. The period of the standard cell is 450 nm, the width of the opening is varied between 390 nm and 600 nm by index matching of each layer to the previous layer.

### 2.5.2. Fabrication process of the multi-layer transmissive shutter

The fabrication process of the two-layer device is discussed here, which can be further developed to stack more layers of the gratings if needed. There are several challenges that must be addressed to cascade two layers of sub-wavelength metallic grating with the thickness of ~200 nm by using the e-beam lithography. The fabrication process starts with the deposition and lift-off of several gold alignment marks and the support structures on a 500 μm fused silica wafer using the traditional optical lithography (see Figure 17). Then, the first layer of the gold grating is patterned utilizing the e-beam lithography system and

a 400-nm thick PMMA-4% photo resist. This is followed by the Ti/Au deposition and lift-off processes, similar to that of a single layer shutter.

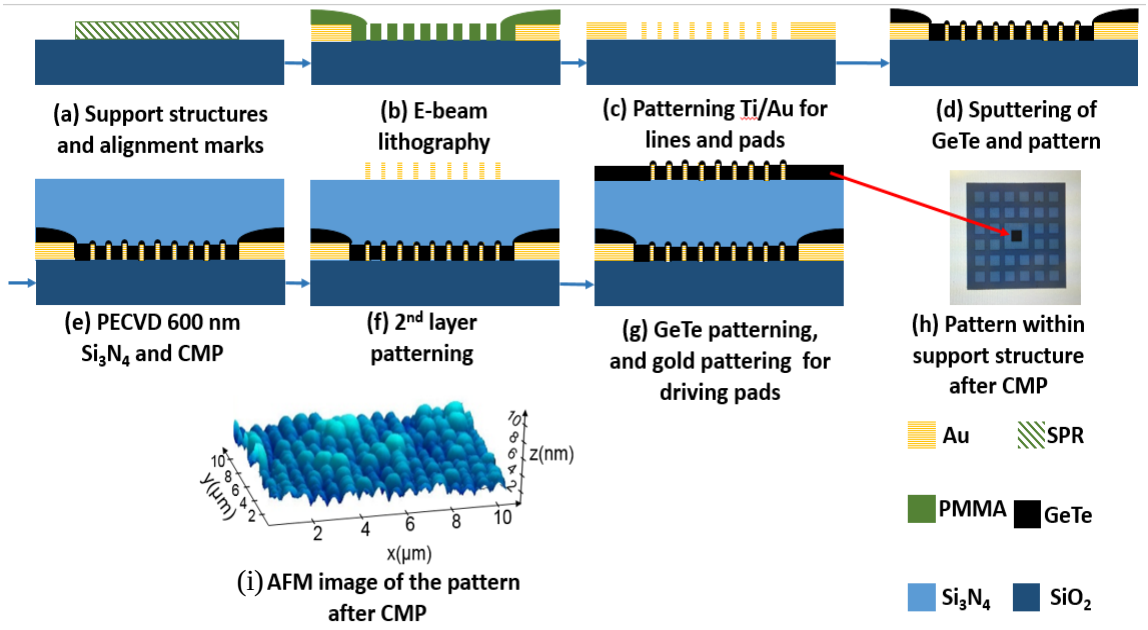


Figure 17. (a-g) Multi-layer shutter fabrication process flow (shown in cross section of the grating). (h) The top view of the modulator after the fabrication of the first layer. (i) An AFM picture showing the surface of the grating after the CMP process. The surface roughness is less than 5 nm.

Next, we deposit a 400 nm $Si_3N_4$ film by using the PECVD technique at ~200 ºC. This $Si_3N_4$ layer serves as the isolation layer for the second layer of the grating. The CMP process is then used to reduce the surface roughness to < 5 nm as required for the succeeding e-bean lithography step. This minimum surface roughness is verified along the

surface of the shutter by using the atomic force microscopy (AFM) from NanoMan AFM (Bruker Co.). The supporting structures that are adjacent to the grating area of the shutter help to reduce the sheer force on the gratings and thus improve the yield significantly (from single- to double-digit percentage). Figure 17 (h) shows the microscopic image of the patterned image after a successful CMP process before patterning the second layer of the shutter. The darker area in the center shows the active area of the device, which is surrounded by protecting gold pillars. Atomic force microscopy of the polished surface is also shown in Figure 17 (i) with < 5 nm roughness.

The second layer of the grating with the thickness of 195 nm, a period of 450 nm, and the line width of 150 nm is then patterned using the same e-beam lithography tool. E-beam exposure is calibrated using proximity effect correction with Beamer software (GenISys Inc.) to achieve more uniformity during the pattern writing. GeTe is then sputtered at a rate of 0.8 Å/s using the LAB-18 sputtering tool (Kurt J. Lesker Co.). The top view SEM image of the device with the top gold layer exposed is shown in Figure 18. The accuracy of the alignments for both layers can also be seen from this image showing bottom layer in the darker color. As mentioned before, a conductive liquid is used here to reduce the charging effect on the glass substrate and achieve a sharper SEM image.

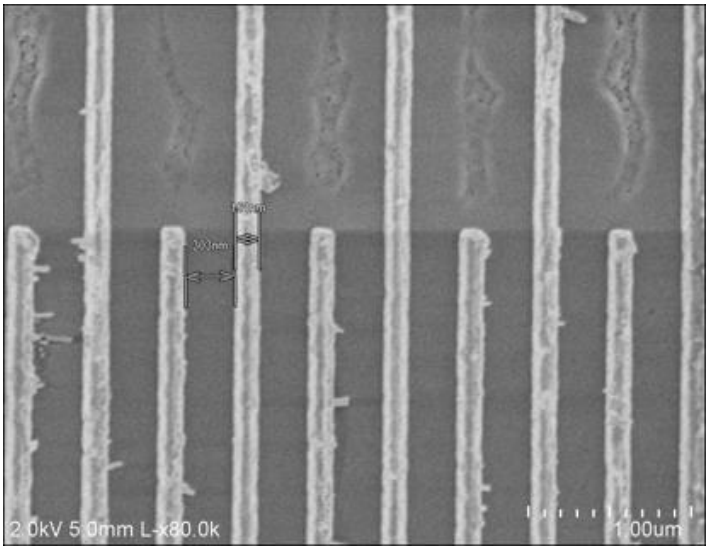


Figure 18. A top-view SEM image of the device, which shows both layers of gold arrays and the GeTe films in between them. Selected lines of gold slits are electrically connected to the pads to match the electrical resistance of the gold grating to 50 Ω for efficient Joule heating.

## 2.6. Optical measurements of the two-layer shutter

Compared to a single-layer design, the multi-layer stack offers 100% improvement in the modulation index (Figure 15 (c)) by exciting two SPP resonance modes (one in each of the layers) and coupling the incoming light to these surface resonance modes (Figure 15 (a)) [2.31]. To modulate the GeTe film from crystalline phase to the amorphous phase, a rapid cool down process is needed. The unconnected gold lines within the GeTe film provide the heat sink required for the fast cooling without the need for any active cooling approach. Crystallization on the other hand can be achieved much easier by heating the

GeTe film to the glass transmission temperature (~ 200 ºC). The measured crystallization energy is 10 pJ when a pulse with the frequency of 2 MHz is used. Cary 620 uFTIR (Agilent Technologies Inc.) is used here to measure the transmission of the TM-polarized light in an area of 100 μm × 100 μm within the shutter. These measurements show a remarkable modulation contrast of ~30 dB with forward loss of less than 2.5 dB for TM-polarized light (Figure 19) for a two-layer device. The slit resonance is located at 1.55 μm and the wavelength of the SPP excitation are in good agreement with the simulation results that are shown in Figure 15. It is also worth mentioning that the frequency of the SPP dip depends on the angle of the incidence light in the FTIR spectroscopy. The Cassegrain objective, which is used in the microscope sample mount of the Cary-620 system causes a red-shift in the SPP resonance as shown here [2.32]. The measurement data are plotted on top of the simulations for easier comparison.

In summary, a novel method of modulating the transmission of the light through sub-wavelength gold grating filled with a PCM was discussed in this chapter. The integrated PCM, which is GeTe in this device, undergoes the crystallographic phase transitions when it is annealed by passing the current through the integrated gold lines. the same sub-wavelength array of gold lines, improves the modulation index (contrast) by taking advantage of the so-called slit and SPP resonances.

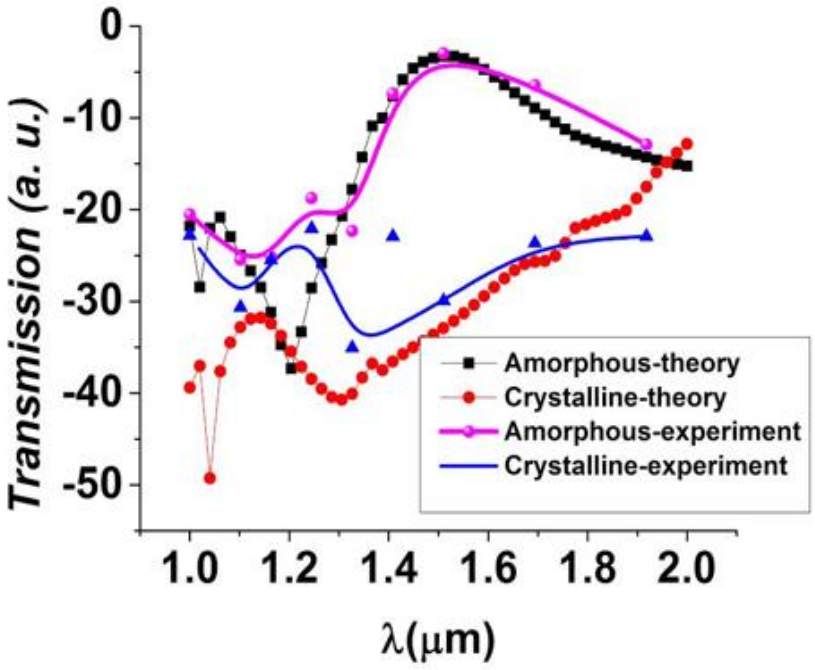


Figure 19. Modeled and experimental transmission of the TM-polarized light for both a-GeTe and c-GeTe in logarithmic scale. The dip resembles the coupling of the light to the SPPs while the peak corresponds to the slit mode. Experimental data are extracted using an uFTIR spectrometer. The error in near 1 μ m region is due to detector loss. Red shift in SPP resonance in the measured data is due to ~20° incident angle of the light in Cassegrain objective which is integrated in the microscope sample holder of the Cary 620.

## 2.7. References


[2.1] Margolis, H. S., Barwood, G. P., Huang, G., Klein, H. A., Lea, S. N., Szymaniec, K., & Gill, P. "Hertz-level measurement of the optical clock frequency in a single 88Sr+ ion". Science, 306(5700), 1355-1358(2004).

[2.2] Guo, T., Deng, K., Chen, X. and Wang, Z., "Atomic clock based on transient coherent population trapping." Applied Physics Letters, 94(15), p.151108.(2009)

[2.3] Vallone, G., Bacco, D., Dequal, D., Gaiarin, S., Luceri, V., Bianco, G., & Villoresi, P. " Experimental satellite quantum communications." Physical Review Letters, 115(4), 040502.(2015)

[2.4] Smith, N. R., Abeysinghe, D. C., Haus, J. W., & Heikenfeld, J. "Agile wide-angle beam steering with electrowetting microprisms." Optics Express, 14(14), 6557-6563. (2006).

[2.5] Carpi, F., Frediani, G., Turco, S., & De Rossi, D. "Bioinspired tunable lens with muscle-like electroactive elastomers." Advanced Functional Materials, 21(21), 4152-4158. (2011).

[2.6] Yang C, Shen W, Zhou J, Fang X, Zhao D, Zhang X, Ji C, Fang B, Zhang Y, Liu X, Guo LJ. "Angle robust reflection/transmission plasmonic filters using ultrathin metal patch array." Advanced Optical Materials, 4(12), 1981-6. (2016)

[2.7] Solgaard, O., Godil, A. A., Howe, R. T., Lee, L. P., Peter, Y. A., & Zappe, H. "Optical MEMS: From micromirrors to complex systems." Journal of Microelectromechanical systems, 23(3), 517-538. (2014).

[2.8] Y Byeong-Hun, et al. "Light shutter using dichroic-dye-doped long- pitch cholesteric liquid crystals." Optics express, 21(24), 29332- 29337. (2013).

[2.9] Decker, Manuel, Christian Kremers, Alexander Minovich, Isabelle Staude, Andrey E. Miroshnichenko, Dmitry Chigrin, Dragomir N. Neshev, Chennupati Jagadish, and Yuri S. Kivshar. "Electro-optical switching by liquid-crystal controlled metasurfaces." Optics express 21(7), 8879-8885. (2013).

[2.10] M. Jafari, M. Rais-Zadeh. "Zero-static-power phase-change optical modulator," Optics letter 41(6), 1177-1180, (2016).

[2.11] Wang, Muzhi, Feng Lin, and Mina Rais-Zadeh. "Performance measurements and non-linearity modeling of GeTe phase change RF switches with direct and indirect heating schemes." IEEE MTT-S International Microwave Symposium. IEEE, 1-4,(2015).

[2.12] J. Sun, Y. Chen, and S. T. Wu. "Submillisecond-response and scattering-free infrared liquid crystal phase modulators." Optics express 20.18 (2012): 20124-20129.

[2.13] J. W. McCargar, "Polymer dispersed liquid crystal infrared light shutter," J. Electron. Imaging 1, 22 (1992).

[2.14] J. L. West, "Characterization of Polymer Dispersed Liquid- Crystal Shutters by Ultraviolet Visible and Infrared- Absorption Spectroscopy," 7, 3785–3790 (1991).

[2.15] D. K. Yang, L. C. Chien, and J. W. Doane, "Cholesteric liquid crystal/polymer dispersion for haze-free light shutters," Appl. Phys. Lett. 60, 3102–3104 (1992).

[2.16] J. L. West, J. R. Kelly, K. Jewel, and Y. Ji, "Effect of polymer matrix glass transition temperature on the polymer dispersed liquid crystal electro-optics," Appl. Phys. Lett. 60, 3238–3240 (1992).

[2.17] J. De Feijter, J. Benjamins, and F. Veer, "Ellipsometry as a tool to study the adsorption behavior of syntetic and biopolyers at the air water interface," Biopolymers 17, 1759–1772 (1978).

[2.18] Němec, P., Moreac, A., Nazabal, V., Pavlišta, M., Přikryl, J., & Frumar, M. (2009). Ge–Sb–Te thin films deposited by pulsed laser: An ellipsometry and Raman scattering spectroscopy study. Journal of Applied Physics, 106(10), 103509.

[2.19] T. Ebbesen, H. Lezex, H. Ghaemi, T. Thio, and P. Wolff, "Extraordinary Optical Transmission Through Sub-Wavelength Hole Arrays," Nature 391, 667–669 (1998).
[2.20] J. T. Shen, P. B. Catrysse, and S. Fan, "Mechanism for designing metallic metamaterials with a high index of refraction," Phys. Rev. Lett. 94, 1–4 (2005).
[2.21] Wang, M., Shim, Y., & Rais-Zadeh, M. (2014). A low-loss directly heated two-port RF phase change switch. IEEE Electron Device Letters, 35(4), 491-493.
[2.22] M. Jafari and M. Rais-Zadeh,"A 1550 nm phase change electro-optical shutter array" in 29th IEEE International Conference on MEMS, China, p. 655-658 (2016).
[2.23] Z. Han and E. Forsberg, "Surface plasmon bragg gratings formed in metal-insulator-metal waveguides," IEEE Photonics Technol. Lett. 19, 91–93 (2007).
[2.24] V. Krasavin and A. V. Zayats, "Three-dimensional numerical modeling of photonic integration with dielectric-loaded SPP waveguides," Physical Review B. 78, 1–8 (2008).
[2.25] Q. Zhang, X.-G. Huang, X.-S. Lin, J. Tao, and X.-P. Jin, "A subwavelength coupler-type MIM optical filter.," Optic Express 17, 7533–7539 (2009).
[2.26] S. Collin, F. Pardo, R. Teissier, and JL. Pelouard,"Horizontal and vertical surface resonances in transmission metallic gratings." Journal of Optics A: Pure and Applied Optics 4.5 (2002): S154.
[2.27] Born, Max, and Emil Wolf. Principles of optics: electromagnetic theory of propagation, interference and diffraction of light. Cambridge university press, 1999.
[2.28] P. B. Johnson, R. W. Christy, and R. W. C. p. b. Johnson, "Optical Constants of the Noble Metals," Phys. Rev. B 6, 10 (1972).
[2.29] J. Zhou and L. J. Guo, "Transition from a spectrum filter to a polarizer in a metallic nano-slit array," Scientific report 4, 2014.
[2.30] Jafari, M., and M. Rais-Zadeh, "Zero-static-power phase-change optical modulator." Optics letters, 41(6), pp. 1177-1180, 2016.
[2.31] Jafari, M., & Rais-Zadeh, M. (2017, August). An ultra-high contrast optical modulator with 30 dB isolation at 1.55 μm with 25 THz bandwidth. In Photonic fiber and crystal devices: advances in materials and innovations in device applications XI (Vol. 10382, p. 1038211). International Society for Optics and Photonics.
[2.32] J. M. Foley, "Subwavelength Dielectric Grating-based Broadband Reflectors and Narrowband Transmission Filters." Ph.D. thesis, University of Michigan, 2014.

# Chapter 3: Reflective Shutter Based on the Thin Film Resonance Effect

To achieve an electro-optical shutter with higher contrast, an optical cavity such as one made using a sub-wavelength layered structure may be used. The higher contrast is a result of the cavity resonances that have high absorption only at particular wavelengths [3.1]. Such a device is useful in many different applications including tunable mirrors, modulators, and photo-detectors [3.2-3.4]. A distributed Bragg reflector (DBR), which consists of layers of different films (thickness~$\lambda/4n$) or sub-wavelength meta-surfaces are often used to trap light inside the cavity. The multi-layer nature of DBR enhances the internal reflections of the light from the interior interfaces of the cavity. However, DBRs usually have either a thick stack of films, very complex designs [3.5], or complicated fabrication/growth processes [3.6]. A simpler approach to achieve high absorption in a thin structure is to use a perfect absorber using the total light absorption (TLA) phenomenon. The TLA effect is shown to occur in a very thin layer of a lossy dielectric on a metal surface [3.7-3.9]. A light reflector based on the same TLA effect was shown recently by using a relatively thin vanadium oxides ($VO_x$) film as the tunable optical material. However, a real-time reversible switchable (reconfigurable) device has not been demonstrated to-date. Moreover, $VO_x$ requires a steady supply of power to maintain its

insulator state at >68 °C. This results in an unnecessary high-power consumption in applications where a low rate of transitions is required [3.10]. In addition, the change in the refractive index of the $VO_x$ is only pronounced at IR regions and it is not significant at the visible range. Thus, it is not suitable for visible and NIR range applications targeted in this work [3.11].

This chapter introduces a high-contrast reflective optical shutter that exploits the TLA phenomenon in a thin GeTe film on a metal reflector. The change in the refractive index of the GeTe causes a shift in the wavelength of maximum light absorption, which corresponds to a dip in the reflection response of the device. This wavelength-shift accordingly modulates the reflection amplitude at the wavelengths of maximum absorption before and after the phase transition. So, the reflection-based electro-optical shutter switches between "ON" and "OFF" states when the GeTe film undergoes phase transitions by exhibiting significantly different optical responses due to the shift in the resonance frequency in the amorphous vs. crystalline GeTe film. Similar to transmission-based shutters, the GeTe film switches between its amorphous and crystalline phase by using the joule heating approach. The heat required to transition the thin layer of sputtered GeTe is provided by passing DC current through an integrated heater that is located underneath the whole stack. As mentioned previously, the memory-like behavior of the phase transitions of the GeTe results in zero static power consumption in either "ON" or "OFF" phases of the shutter. Thus, such PCM-based shutters can find application in ultra-low power and

portable optical systems. The design and fabrication of this shutter is discussed next, followed by the experimental measurements.

## 3.1. Basics and structure

A top-view schematic of the shutter is shown in Figure 20 (a) along with its cross-section in Figure 20 (b). As shown in these figures, the GeTe-based shutter consists of a thin (thickness ~ $\lambda/22$) GeTe layer, which is located above a gold reflecting film. A 200 nm-thick silicon nitride ($Si_3N_4$) layer is located on top of the heater, which serves as an electrical isolator. Underneath this nitride layer, a NiCr film is deposited, which serves as the heater. This heater is used to transition the phase of GeTe by employing the Joule heating approach. Two gold pads are used to connect the NiCr heater to the power supply to apply the voltage pulses with the period of a few microseconds. The amplitude of the reflected light is modulated when GeTe transitions between amorphous (ON) and crystalline (OFF) phases. TLA causes a dip in the reflection of the light from the surface of the 40-nm-thick GeTe film on top of the gold reflector. This dip is located at 780 nm when GeTe is amorphous and is red-shifted to longer wavelengths when GeTe is crystallized. The dip in the reflection at 780 nm is due to the minimal reflection from the GeTe/air interface trapping the incident light inside the amorphous GeTe film, which is shown with the red arrow in Figure 20 (b). When GeTe is crystalline, more than 40% of the light reflects back from the GeTe/air interface at the same 780 nm wavelength. This is

due to the fact that the TLA resonance is red-shifted and is located at 1.2 μm for the case of the c-GeTe. For the same reason (higher reflections), the stack with c-GeTe has a shiny metallic surface at the visible range.

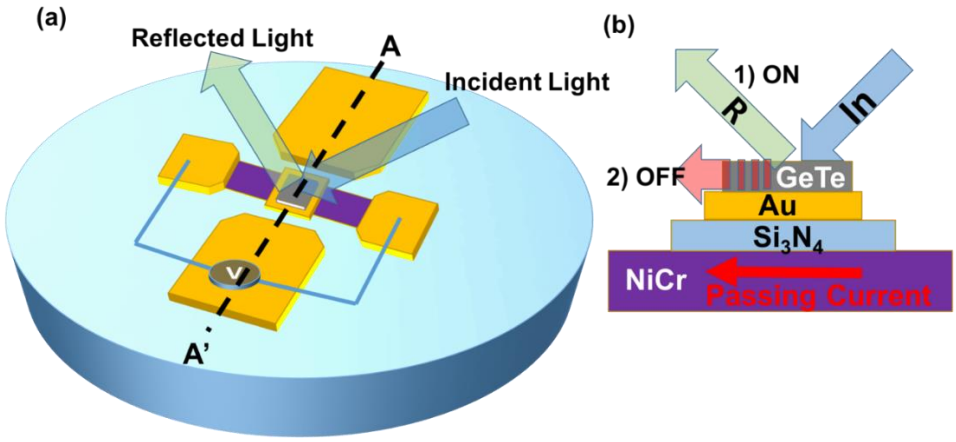


Figure 20. Schematics of the shutter appear above demonstrated on top of a fused silica wafer. The NiCr heater is shown in purple color, which is sitting under the $Si_3N_4$ passivation layer and the gold mirror (in yellow). The gray film demonstrates the GeTe patch that is grown on top of the stack. (b) A-A' cross-section of the switch, which shows the stack of the films and the light path in ON (crystalline) and OFF (amorphous) states of the shutter.

## 3.2. Modeling

Any number of thin-film dielectrics on top of a metallic surface form an asymmetrical Fabry-Perot cavity, which supports many resonance points with low reflections. The wavelengths of these resonances are determined by the thicknesses of the dielectric films and the dispersion of their refractive indices [3.12]. To model the wavelengths of these

reflection dips (high absorption points), a transfer matrix method is used. With "NL" being the number of dielectric layers, the total transmission matrix is defined as [3.13]:

$$\mathbf{M} = \mathbf{M_1} \times \mathbf{M_2} \times ... \times \mathbf{M_{NL+1}} \times \mathbf{M_{NL+2}}, \tag{3-1}$$

where $(NL+2)^{th}$ layer is the glass substrate that is sitting under the metallic layer. $M_i$ is the transfer matrix of each of the layers and is defined as:

$$\mathbf{M_i} = \frac{1}{t_{ii}} \begin{bmatrix} \mathbf{1} & \mathbf{r_{ii}} \\ \mathbf{r_{ii}} & \mathbf{1} \end{bmatrix} \begin{bmatrix} \mathbf{e^{-i\delta_{i+1}}} & \mathbf{0} \\ \mathbf{0} & \mathbf{e^{i\delta_{i+1}}} \end{bmatrix}, \tag{3-2}$$

where, $t_{ii}$ and $r_{ii}$ are the Fresnel coefficients of transmission and reflection, respectively. These coefficients are defined as:

$$\mathbf{t_{ii}} = \frac{\mathbf{2k_i}}{\mathbf{k_i + k_{i+1}}}, \tag{3-3}$$

$$\mathbf{r_{ii}} = \frac{\mathbf{k_i - k_{i+1}}}{\mathbf{k_i + k_{i+1}}}, \tag{3-4}$$

where $\mathbf{k_i} = \mathbf{n_i cos(\theta_i)}$ ($\mathbf{k_i} = \mathbf{n_i / cos(\theta_i)}$) for TE(TM) polarization. One can easily derive the total transmission and reflection value from eqn. (3-1) as:

$$\mathbf{T} = \frac{\mathbf{k_{NL+2}}}{\mathbf{k_1}} \frac{\mathbf{1}}{\mathbf{|M_{11}|^2}}, \tag{3-5}$$

$$\mathbf{R} = \frac{\mathbf{|M_{21}|^2}}{\mathbf{|M_{11}|^2}}. \tag{3-6}$$

Finally the reflection and transmission of the light for a device, which consists of a thin GeTe film over an optically thick gold film is simplified as:

$$\mathbf{R} = \left( \frac{\mathbf{r_{12} + r_{23} e^{2i\beta}}}{\mathbf{1 + r_{12} r_{23} e^{2i\beta}}} \right)^{\mathbf{2}}, \tag{3-7}$$

$$\mathbf{T} = \frac{\mathbf{k_{NL+2}}}{\mathbf{k_1}} \left( \frac{\mathbf{t_{12} t_{23} e^{i\beta}}}{\mathbf{1 + r_{12} r_{23} e^{2i\beta}}} \right)^{\mathbf{2}}. \quad (3\text{-}8)$$

The reflection spectra of the devices with different thicknesses of the a-GeTe and c-GeTe are shown in Figure 21 (a) and (b), respectively. As shown in this figure, the reflection of the device has a dip, which corresponds to the TLA effect that is located within the visible and NIR regions. The wavelength of such a dip depends strongly on the thickness of the GeTe, as shown in Figure 21. This low reflection region (dip) that is shown with a darker blue color is a direct result of destructive interference of the consequential reflections within the thin GeTe film. This thin film resonance is slightly red shifted (moves to longer wavelengths) as the GeTe gets thicker. To experimentally demonstrate the dependence of the TLA wavelength to the thicknesses of the GeTe films, different films with thicknesses ranging from 20 nm to 60 nm are sputtered over an evaporated gold film. These pieces having different thicknesses of the GeTe film show different colors, as shown in Figure 22.

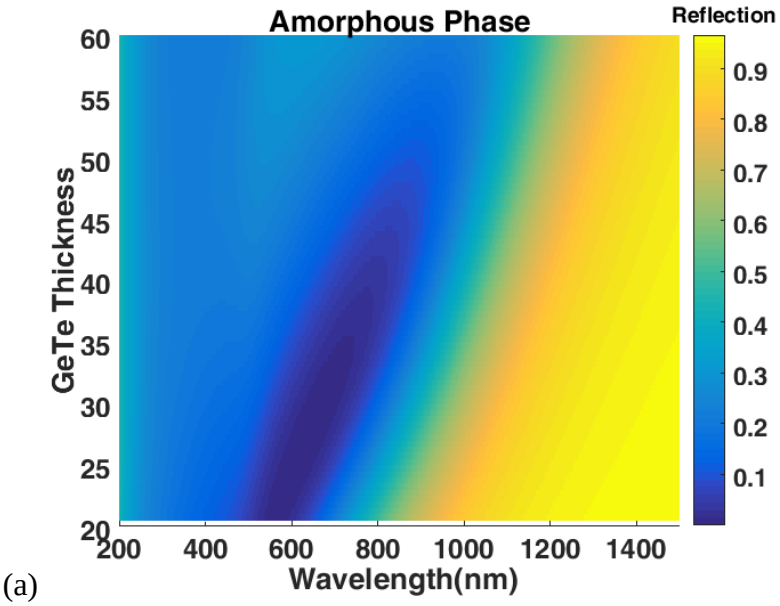


(a)

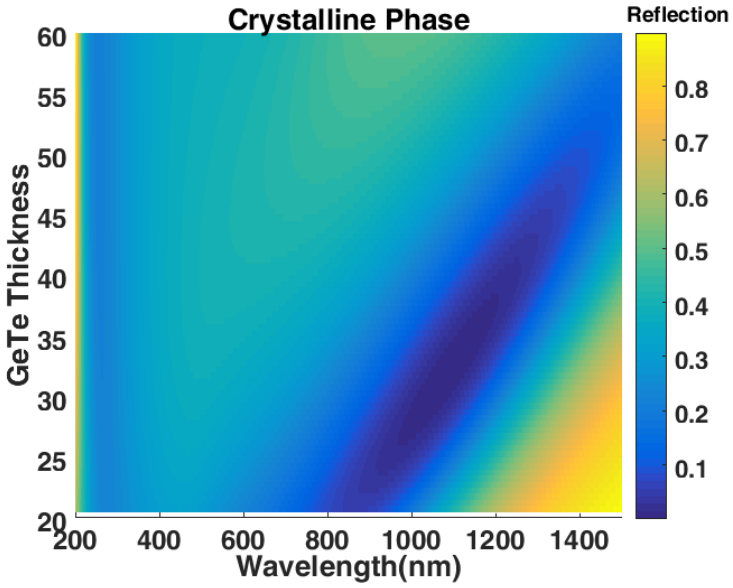


(b)

Figure 21. Reflection of the GeTe films with different thicknesses at visible-NIR region for (a) amorphous and (b) crystalline GeTe. Dark blue color indicates the wavelength of minimum reflection. For example, for the 40 nm film, the wavelength shifts from 780 nm for amorphous film to ~1200 nm for the crystalline film.

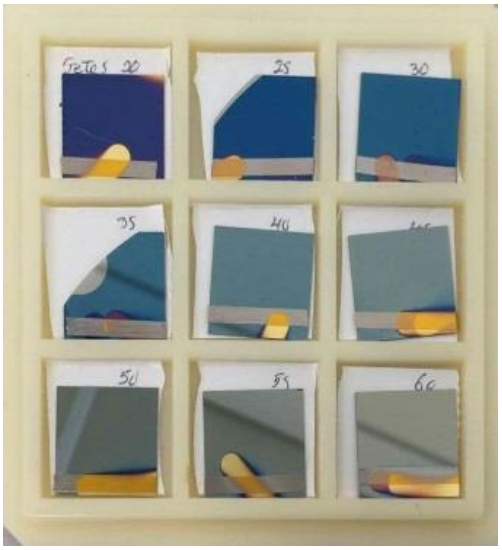

Figure 22. Different reflected colors for GeTe films of different thicknesses deposited over gold. The change in the perceived color is due to the change in the wavelength of the TLA.

## 3.3. Fabrication process and challenges

The fabrication process of the shutter is shown in Figure 23. A NiCr layer is deposited on a fused silica substrate with the thickness of 515 µm using an Enerjet electron beam evaporator to serve as the integrated Joule heater. The input impedance of the NiCr heater is matched to the DC probes with 50-Ω input impedance for maximum power transfer. To achieve this, the heater is patterned using the traditional optical lithography using the SPR 220-3 and LOR-3A lift-off photoresists, both from MicroChem Corp. (MA, USA). A passivation silicon nitride film is then deposited on top of the heater using the PECVD process. The surface of the shutter is subsequently polished using the CMP process to

achieve a uniform deposition of the successive layers. This is followed by reactive ion etching (RIE) of silicon nitride to access to the integrated heater by utilizing a Plasmatherm-790 RIE system. Next, an optically thick (~150 nm) titanium/gold film is deposited using the Enerjet electron beam evaporator. This Ti/Au film covers the active area of the shutter, which is 400 μm ×400 μm, two other 2 cm×2 cm calibration areas, as well as the vias to the pads.

Then an amorphous GeTe film with 40 nm thickness is sputtered on top of the gold reflector. The GeTe is sputtered using a Kurt J. Lesker sputtering tool at 0.66 Å/s from a 3-inch target (from Mitsubishi Materials Co.) at a 4.5 mTorr pressure, with a 60 W power, and at the room temperature. Thickness of the deposited film is verified at each step by using the ellipsometry measurement of a control sample. The control sample consists of a silicon substrate passivated with a $SiO_2$ film with the thickness of 250 nm mounted next to the main sample for a simpler and more accurate measurement. Multiple control samples are prepared and measured to achieve ~1 nm thickness accuracy with the same chamber conditions that are used for the main device.

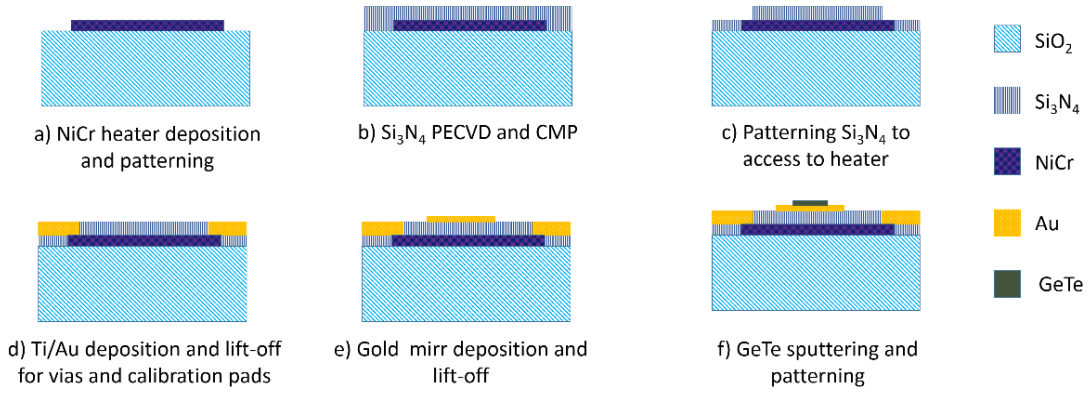


Figure 23. The fabrication process of the reflective GeTe-based shutter.

## 3.4. Results and discussion

Measurements are performed using a DC probe station to apply pulsed voltages to the shutter for electrical transitioning of the GeTe film. The electrical pulses with an amplitude of 100 V and a period of 200 ns ($f$ = 5 MHz) are used for the amorphization of the device. The geometry of the shutter, having a large body of metal underneath the GeTe layer, facilitates fast cooling rate required for amorphization. This comes from the smaller RC time constant when there is a metallic film near the PCM films compared to stacks that the GeTe is sitting in between thick dielectrics. This obviates the need for an extra active cooling element for amorphization. To achieve full crystallization of the GeTe film, electrical pulses with 20 V amplitude and 2 μs period ($f$ = 0.5 MHz) are applied from the pads and through the NiCr heater. The thin GeTe film is transitioned electrically using this

NiCr heater for several cycles. The reflection of the linearly polarized light from the surface of the shutter is measured using the Woollam M-2000 ellipsometer for both crystalline and amorphous phase of the GeTe to extract the modulation contrast of the reflected light (Figure 24). As shown in this figure, the reflection of the light is modulated by > 20 dB, which is a new record for a PCM-based shutters at 780 nm. The 20 dB is not the modulation index of the device but rather the limitation of the tool used. It is envisioned that the theoretical value of 40 dB could be achieved by using a more accurate optical measurement system.

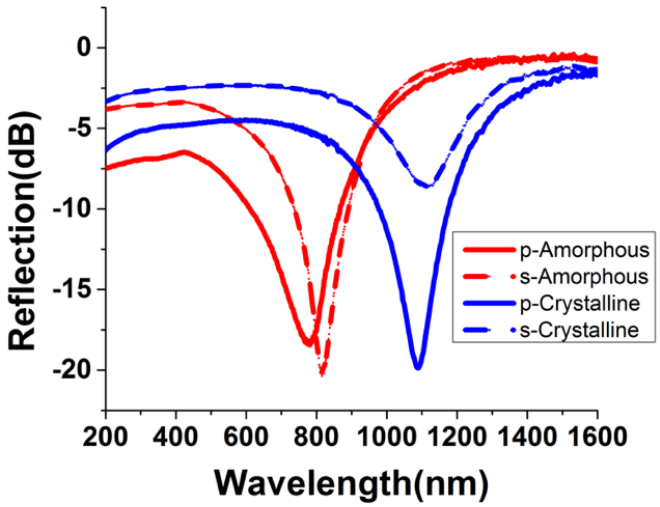


Figure 24. The reflection of the TM (p) and TE(s) linear polarization of the light from the surface of the shutter at the visible and NIR regions. The crystalline phase of GeTe (shown in blue curves) supports a TLA dip at 1100 nm, while amorphous phase (shown in red curves) has dip in the reflection spectrum at 780 nm which comes from the TLA resonance.

The performance comparison of the proposed reflective shutter in this chapter as well the transmission-base optical shutters introduced in the previous chapter (all in italic), are compared with the devices reported in the literature in Table 3.1. As listed in Table 3.1, both the multi-layer transmissive and the reflective shutter of this work shows a remarkable high contrast compared to other devices based on thermochromic materials. Also, note that the reflective shutter presented in this chapter is the only shutter that works at 780 nm using phase change material.

Table 3.1. Performance comparison of the GeTe-based shutters of this work with the devices reported in the literature.

| Device | Modulation index | Switching time | Energy | λ (μm) |
|---|---|---|---|---|
| $VO_2$ absorber [3.14] | 9 | N/A | N/A | 10 |
| GST modulator [3.15] | 10 | N/A | N/A | 3.5 |
| Shutter [3.16] | 15 | N/A | N/A | 1.5 |
| Shutter [3.17] | 10 | N/A | N/A | 1.5 |
| Memory [3.18] | 3 | 0.1 μs | 533 PJ | 1.5 |
| *Shutter [3.19]* | *12* | *2 μs* | *4 pJ* | *1.5* |
| *Shutter [3.20]* | *27* | *2 μs* | *10 pJ* | *1.5* |
| *This work [3.21]* | *21* | *2 μs* | *10 μJ* | *0.78* |

## 3.5. References


[3.1] Rensberg, J., Zhang, S., Zhou, Y., McLeod, A. S., Schwarz, C., Goldflam, M., ... & Basov, D. N. “Active optical metasurfaces based on defect-engineered phase-transition materials.” Nano letters, 16(2), 1050-1055. (2016).

[3.2] Zaugg, C. A., et al. "Ultrafast and widely tuneable vertical-external-cavity surface-emitting laser, mode-locked by a graphene-integrated distributed Bragg reflector." Optics express 21(25), 31548-31559. (2013).

[3.3] Szyszka, A., et al. "Enhanced ultraviolet GaN photo-detector response on Si (111) via engineered oxide buffers with embedded Y2O3/Si distributed Bragg reflectors." Applied Physics Letters 104(1), 011106. (2014).

[3.4] Rahman, M. M., Marsal, L. F., Pallarès, J., & Ferré-Borrull, J. “Tuning the photonic stop bands of nanoporous anodic alumina-based distributed Bragg reflectors by pore widening.” ACS applied materials & interfaces, 5(24), 13375-13381.(2013)

[3.5] Vafapour, Z., and A. Zakery. "New approach of plasmonically induced reflectance in a planar metamaterial for plasmonic sensing applications." Plasmonics 11(2), 609-618.(2016).

[3.6] Jafari, M., & Rais-Zadeh, M. “A 1550 nm phase change electro-optical shutter.”IEEE 29th International Conference on Micro Electro Mechanical Systems (MEMS), 655-658. IEEE. (2016).

[3.7] Kats, Mikhail A., and Federico Capasso. "Optical absorbers based on strong interference in ultra-thin films (Laser Photonics Rev. 10 (5)/2016)." Laser & Photonics Reviews 10(5), 699-699.(2016)

[3.8] Sturmberg, Björn CP, et al. "Total absorption of visible light in ultrathin weakly absorbing semiconductor gratings." Optica 3(6),556-562. (2016)

[3.9] Mirshafieyan, Seyed Sadreddin, and Junpeng Guo. "Silicon colors: spectral selective perfect light absorption in single layer silicon films on aluminum surface and its thermal tunability." Optics express 22(25), 31545-31554. (2014).

[3.10] Rensberg, Jura, Shuyan Zhang, You Zhou, Alexander S. McLeod, Christian Schwarz, Michael Goldflam, Mengkun Liu et al. "Active optical metasurfaces based on defect-engineered phase-transition materials." Nano letters 16(2), 1050-1055.(2016).

[3.11] Scherer, D. R., Lutwak, R., Mescher, M., Stoner, R., Timmons, B., Rogomentich, F., Taylor, D. “Progress on a Miniature Cold-Atom Frequency Standard.” arXiv preprint arXiv:1411.5006.(2014).

[3.12] Raoux, Simone, and Daniele Ielmini. "Phase change materials and their application to nonvolatile memories." Chemical reviews 110(1), 240-267.(2009).

[3.13] M. Born and E. Wolf, “Principles of Optics, 7th ed.” Cambridge University Press, (2003).

[3.14] Kats, M. A., Sharma, D., Lin, J., Genevet, P., Blanchard, R., Yang, Z., ... & Capasso, F. (2012). Ultra-thin perfect absorber employing a tunable phase change material. Applied Physics Letters, 101(22), 221101.

[3.15] A.Tittl, et al. “A switchable mid-infrared plasmonic perfect absorber with multispectral thermal imaging capability,” Advanced Materials 27(31), 4597-4603. (2015).

[3.16] Heinilehto, S. T., Lappalainen, J. H., Jantunen, H. M., & Lantto, V. (2011). IR-wavelength optical shutter based on ITO/VO 2/ITO thin film stack. Journal of electroceramics, 27(1), 7-12.

[3.17] Y Byeong-Hun, et al. "Light shutter using dichroic-dye-doped long- pitch cholesteric liquid crystals." Optics express, 21(24), 29332- 29337. (2013).

[3.18] C. Ríos, M. Stegmaier, P. Hosseini, D. Wang, T. Scherer, C. D. Wright, H. Bhaskaran, and W. H. Pernice, "Integrated all-photonic non-volatile multi-level memory." Nature Photonics, 9(11), 725-732. (2015).

[3.19] M. Jafari, and M. Rais-Zadeh. “Zero-static-power phase-change optical modulator,” Optics letter 41(6), 1177-1180, (2016).
[3.20] Jafari, M., & Rais-Zadeh, M. (2017, August). An ultra-high contrast optical modulator with 30 dB isolation at 1.55 μm with 25 THz bandwidth. In Photonic fiber and crystal devices: advances in materials and innovations in device applications XI (Vol. 10382, p. 1038211). International Society for Optics and Photonics.
[3.21] Jafari, M., Guo, L. J., & Rais-Zadeh, M. (2017, February). An ultra-fast optical shutter exploiting total light absorption in a phase change material. In Optical components and materials XIV (Vol. 10100, p. 101000I). International Society for Optics and Photonics.

# Chapter 4: Zero Static-Power Tunable Color Filter

This chapter introduces a novel tunable color reflector for low-power display systems, which employs GeTe within a sub-wavelength layered structure. Optical index modulation of GeTe tunes the reflection spectrum of the light at the visible range and thus permits vivid color change with zero static power dissipation. Specifically, ultra-thin layers of GeTe films are sandwiched between a bottom metallic mirror and a top high-index dielectric film, which is usually a metal oxide such as a Titanium oxide. To enhance the sensitivity of the reflected colors to the refractive index of GeTe, a 250 nm thick phase-shift $SiO_2$ layer is placed in between the GeTe layer and the bottom metal reflector. Low sensitivity to angle and polarization of the incident light is useful for standalone and portable applications with limited power supplies, which are addressed with the presented device.

## 4.1. Background

Display systems and color filters are among the most commonly used optical components which produce tunable colors. The core principle in most of these systems is either the emission of light at a single wavelength or the filtering of part of the spectrum when the white ambient light reflects back from the device surfaces or passes through them [4.1-4.4]. Active displays, which need constant power to produce a tunable color, have been well-developed and utilized within the past decades in consumer electronics and

commercial market [4.5]. Light emitting diodes (LED) are commonly used in active display units with improving performance and lowering cost as the technology matures. Due to their low production cost and high performance, LED-based displays are among the most widespread components in commercial products and have replaced old liquid crystal display (LCD) technologies [4.6]. State-of-the art organic LED (OLED) technology can address cost, power, refresh rate, and durability issues that were experienced with the use of traditional LCDs [4.7]. However, even with recent advancement in display technologies, active displays still consume the greatest amount of power in electronic systems. Conversely, passive displays, which reflect back the ambient light, only consume power during color switching. The passive displays are among the most important alternatives to LEDs due to their almost zero static power; and are especially useful in power-starved applications having bright ambient condition and low refresh rate requirements.

Most of the modern display systems, such as those using microelectromechanical (MEMS) mirrors [4.8], colored e-ink [4.9], and OLED [4.10], use three or more sub-pixels with red, green, and blue colors to produce a single pixel of an image with an arbitrary color. However, producing an arbitrary color in a single pixel by changing the characteristic of the pixel element (and not dividing the pixel to more sub-pixels) is a more efficient way to produce more vivid and dense displays [4.11]. An example of such a system is single mirror interferometrics (SMI) displays, where a moving MEMS mirror is used to tune the color of the pixel [4.12-4.14]. Unfortunately, integrated movable objects have proven to be

a major limitation of SMI devices in terms of durability, dynamic power consumption, and reliability against mechanical shocks in portable electronics. To address this, structural-based color filters may be used to improve the endurance and ease the fabrication process. These types of color filters cannot generate all desired colors from the same area of the device [4.15]. As an alternative, chemical-based color pixels provide a wide range of color by employing changes in the optical index of the materials. The change in the chemistry of the electro-chromatic, photo-chromatic, or thermos-chromatic materials [4.16, 4.17], such as chalcogenide glasses [4.18], can be used in a photonic cavity to provide a more versatile reflective display. The tunability of such materials adds another dimension to the passive or active optical components to achieve smart, light, and durable devices. The gradual change of their optical and/or electrical properties in the presence of an external stimulus is very useful in neuromorphic systems [4.19]. Recently, an organic–based protein called reflectine, which is extracted from cephalopods, has also demonstrated color tuning at the visible and camouflage visible-NIR ranges. This organic film is useful for generating colors in milder environments when durability is less critical [4.20]. Non-organic materials, such as the liquid crystals [4.21, 4.22], Germanium (Antimony) Telluride [4.23, 4.24], and Vanadium Dioxide [4.25] are among the most used commonly materials in reconfigurable optical devices for applications used in harsh environments due to their high index contrast and controllable phase transition processes. With two significantly different refractive index values at two different phases, high amplitude modulation can be achieved by

employing both real and imaginary parts of the refractive index. Here, Germanium Telluride (GeTe) was used in a layered photonic structure to produce a color reflector. High optical loss of GeTe in the visible-NIR region must always be considered as a potential limitation for its use in transmission-based devices. This complication was avoided by using a very thin layer of GeTe and utilizing a reflection-based device for ultra-low power displays. As a result, four vivid colors were achieved, which have been switched more than 100 times with application of electrical pulses. Ultra-thin GeTe films that are used in these devices undergo a smoother, more complete, and more reliable crystallographic phase transition with considerably lower loss than what has been observed in devices with thicker films. An additional consideration is that unlike vanadium dioxide or liquid crystal, both phases of GeTe are stable at room temperature without the existence of external stimuli, resulting in zero static power consumption [4.26]. Apart from its color tunability, the presented structure does not require any sub-wavelength lithography, which results in low cost for large-area applications [4.27].

## 4.2. Device modeling and fabrication process

The schematic of the single-layer device is shown in Figure 25. As shown here, the device consists of a thin layer of GeTe, which is sitting on top of a $SiO_2$ phase shift layer. This $SiO_2$ separates the PCM layer from the bottom metal to improve the color contrast by employing an RGB color filtering scheme. By physically separating the GeTe layer from

the bottom metal reflector using the oxide spacer, the reliability of the device is improved compared to the case where GeTe sits directly on the metal [4.28- 4.30].

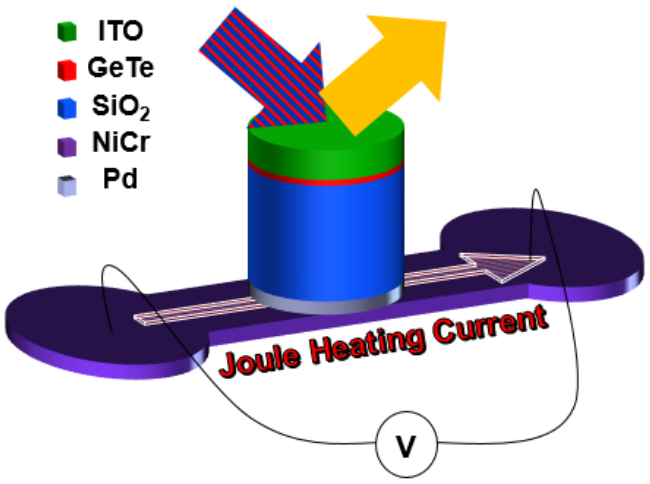


Figure 25. Schematic of the device, which consists of a buried NiCr heater connected to a gold electrode to apply the current. $SiO_2$ phase shift layer (shown in light blue) helps to improve the color tenability with the phase transitioning of the GeTe film (shown in red). Moreover, the top ITO layer is used as an anti-reflection coating to further enhance the color contrast.

A thick palladium reflector is positioned at the bottom, which serves as the bottom reflector of the Fabry Perot cavity. The buried NiCr film is used to apply heat, which is needed for a joule heating-based phase transition. The total reflection of the polarized light can be derived from the transfer matrix method. The total matrix M of the stack is defined as:

$$\mathbf{M} = \prod_n \begin{bmatrix} e^{\beta_n} & r_n e^{\beta_n} \\ r_n e^{-\beta_n} & e^{-\beta_n} \end{bmatrix}, \tag{4-1}$$

Where $r_n$ is the light reflection from $n^{th}$ interface. $\beta_n$ is also the phase accumulation in the $n^{th}$ layer. These parameters are defined as:

$$\mathbf{r_{n,n+1}} = \left(\frac{k_n - k_{n+1}}{k_n + k_{n+1}}\right) , \tag{4-2}$$

$$\boldsymbol{\beta_n} = \mathbf{e}^{ik_n t_n} , \tag{4-3}$$

where $k_n$ is the wavevector of the light in $n^{th}$ layer and $t_n$ is thickness of the $n^{th}$ layer. This wavevector ($k_n$) is defined as $n_n \times \cos(\theta)$ and $n_n/\cos(\theta)$ for s-polarization and for p-polarization, respectively. $n_i$ here is refractive index of $i^{th}$ layer (i=1, 2, 3 and 4) and $\theta$ is the incident angle of the polarized light. One can mathematically derive the reflection of the light by expanding eq. (4-1) as:

$$\mathbf{R} = \left|\frac{\mathbf{M_{01}}}{\mathbf{M_{00}}}\right|^2, \tag{4-4}$$

The total reflection of the light is dependent on the thickness and the refractive index of the phase-shifter layer ($SiO_2$) layer. The lossy GeTe film, which is sitting on top of the $SiO_2$ acts as a node for electromagnetic waves. This node acts as a filter, which only permits the light to reflect back constructively when its wavelength is twice the node spacing. Thus, it is clear that the change in the thickness of the $SiO_2$ layer shifts this node up and down with respect to the bottom palladium reflector. This shift consecutively tunes the wavelength of this peak as shown in Figure 26 for different thicknesses of the $SiO_2$ layer.

This Figure shows how the reflection peak is tuned with different thicknesses of the phase shift layer as following:

$$\boldsymbol{\lambda_{maximum} = 2 \times h_{PS} \times n_{PS}},\tag{4-5}$$

where $h_{PS}$ and $n_{PS}$ are the thickness and the refractive index of the phase shift layer, respectively. For the case of 250 nm $SiO_2$ in the single layer device (shown in Figure 25), this peak is located at ~ 700 nm. As shown in Figure 26 this peak in the reflection exists for both amorphous and crystalline GeTe. This means that this peak is not tunable with phase transitioning of the GeTe due to high optical loss of both phases at the visible range. However, with proper design one can produce a dip in the reflection spectrum within the visible range by employing the thin-film resonance effect that was discussed in the previous chapter. This resonance is the direct result of making the numerator zero in the closed form formula for a thin-film on a metal substrate:

$$\mathbf{r} = \frac{\mathbf{r_{12}+r_{23}e^{i\phi_1}}}{\mathbf{1+r_{12}\times r_{23}e^{i\phi_1}}},\tag{4-6}$$

where $\varphi_1$ is phase accumulation of the light phase in the thin GeTe film, which is equal to $2\pi n_2 h_2/\lambda$. $r_{12}$ and $r_{23}$ are the reflection coefficients at the first and the second interfaces (see Figure 28 (a)) following eq. 4-2. Once cascaded, eq. 4-5 can be used for two thin films sitting on a metallic substrate in which $r_{23}$ changes to the following:

$$\bar{\mathbf{r}}_{\mathbf{23}} = \frac{\mathbf{r_{23}+r_{34}e^{i\phi}}}{\mathbf{1+r_{23}\times r_{34}e^{i\phi}}},\tag{4-7}$$

This total reflection then could be minimized by making its numerator zero with proper values for the thicknesses and refractive indices of the films. The thin film resonance frequency and hence the corresponding dip in the reflection spectrum is tunable with the phase transitioning of the GeTe film. By switching the phase of this thin GeTe layer from amorphous to crystalline and changing its refractive index values, two different colors are achieved. These two colors are produced by shifting the dip in the reflection spectrum from ~450 nm to ~650 nm. Despite the fact that the thicknesses of the films are fixed, the tunable refractive index of GeTe results in the change in the reflection spectrum for both s and p polarizations.

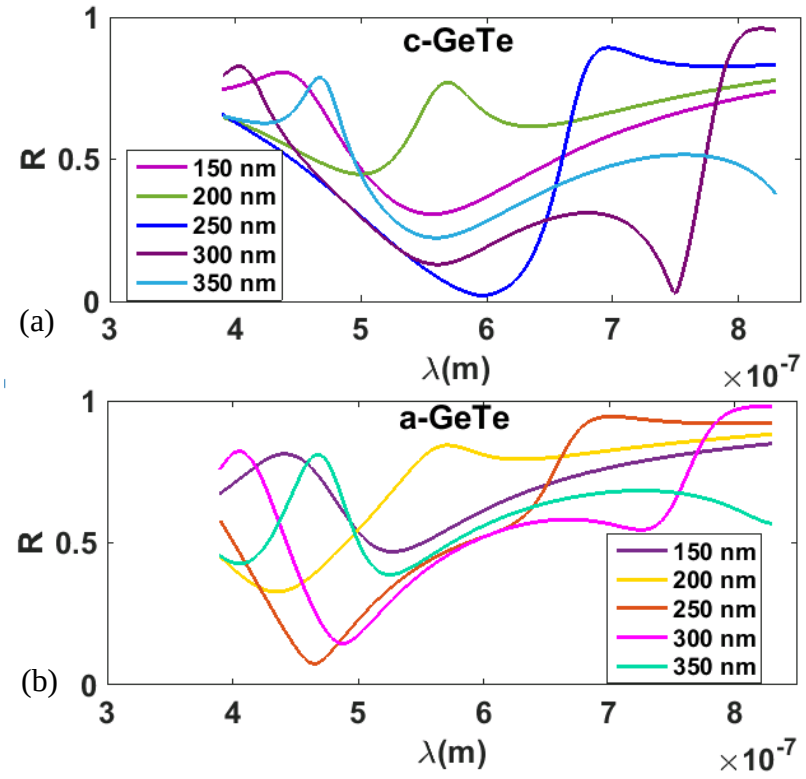


Figure 26. Different thicknesses of the $SiO_2$ phase shifter and the change in the reflection spectra for crystalline (a) and amorphous (b) GeTe films.

## 4.3. Chromaticity measurement

The desired structure to achieve red and blue colors is shown in Figure 28(a). The thicknesses of the films are noted in the same figure: the bottom palladium reflector, which is separated from the PCM layer by the $SiO_2$ layer, has a 250 nm thickness. Another indium tin oxide (ITO) layer is on top of the PCM layer and serves as anti-reflection coating to

enhance the color contrast. Using the standard of the International Commission on Illumination (CIE) that was created in 1931, colors can be quantitatively determined for such a structure. CIE standard uses X and Y coordinates to determine the reflected or transmitted color of the structure. Device reflection spectra were extracted using an ellipsometer for visible-NIR regions. Device reflection is extracted from the measured value of the $\Phi$ and $\Delta$ parameters at different angles ranging from 45° to 75°. To determine the actual color seen from these reflection spectra, a common CIE 1931-2° standard is used. Typical human eyes have three different types of cone cells located inside the fovea that perceive the colors mostly around 2° arc. Normalized spectral sensitivities of these three types of cone cells (S, M, and L) are extracted for a CIE standard observer. Three standard observer color matching functions are then derived from these sensitivities which are defined as: $\bar{x}(\lambda)$, $\bar{y}(\lambda)$, and $\bar{z}(\lambda)$ (Figure 27).

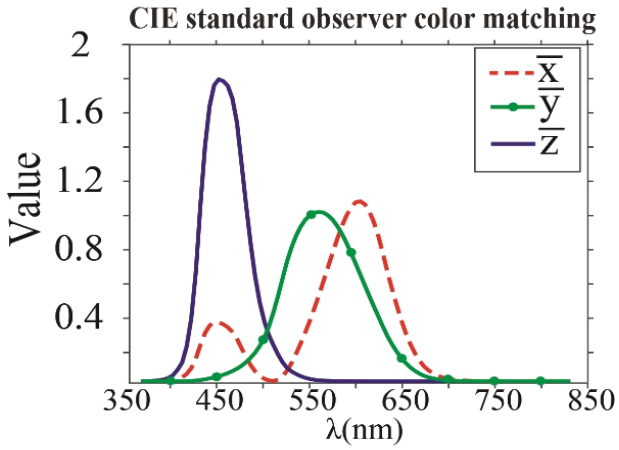


Figure 27. CIE color matching function obtained for the standard observer for the sensitive 2° arc inside fovea.

These matching functions are then integrated over the visible spectrum (390 nm-830 nm) and multiplied by the sample's measured reflection times spectral power distribution of the illuminant to determine X, Y and Z as following:

$$\mathbf{X} = \frac{\mathbf{K}}{\mathbf{N}} \int \mathbf{R}(\boldsymbol{\lambda}) \times \mathbf{I}(\boldsymbol{\lambda}) \times \bar{\mathbf{x}}(\boldsymbol{\lambda}) \mathbf{d}\boldsymbol{\lambda} \tag{4-8}$$

$$\mathbf{Y} = \frac{\mathbf{K}}{\mathbf{N}} \int \mathbf{R}(\boldsymbol{\lambda}) \times \mathbf{I}(\boldsymbol{\lambda}) \times \bar{\mathbf{y}}(\boldsymbol{\lambda}) \mathbf{d}\boldsymbol{\lambda} \tag{4-9}$$

$$\mathbf{Z} = \frac{\mathbf{K}}{\mathbf{N}} \int \mathbf{R}(\boldsymbol{\lambda}) \times \mathbf{I}(\boldsymbol{\lambda}) \times \bar{\mathbf{z}}(\boldsymbol{\lambda}) \mathbf{d}\boldsymbol{\lambda} \tag{4-10}$$

where K is a scaling factor and N is:

$$\mathbf{N} = \int \mathbf{I}(\boldsymbol{\lambda}) \times \bar{\mathbf{y}}(\boldsymbol{\lambda}) \mathbf{d}\boldsymbol{\lambda} \tag{4-11}$$

X, Y, and Z are calculated from these integrals and used to define the normalized chromaticity coordinates x and y, as well as the brightness or luminance of the color (Y). These sets of two coordinates (x,y) and their brightness (Y) are enough to show all colors human eyes can sense using the three types of cone cells. These coordinates are defined as:

$$\mathbf{x} = \frac{\mathbf{X}}{\mathbf{X+Y+Z}}\,, \tag{4-12}$$

$$\mathbf{y} = \frac{\mathbf{Y}}{\mathbf{X+Y+Z}}\,. \tag{4-13}$$

These coordinates are used to locate the actual reflected color of the sample for the brightest colors (i.e. maximum Y). Numbers on the outer curve boundary show the wavelengths of monochromatic light reflection (see Figure 28(d) for an example). It is also important to note that colors, which are seen in this Figure and all other CIE graphs, depend on the display or printer RGB calibration as well as other specifications.

The reflection spectra of the light with s and p polarizations are shown in Figure 28(b) for both amorphous and crystalline GeTe at a 45° incident angle. Even though the PCM film is very thin (20 nm), the change in the CIE coordinates is drastic when the GeTe layer undergoes phase transitions. The CIE chromaticity graph of the device is shown in Figure 28(d) for both phases of the GeTe layer. The reflection of the light with the p polarization is less sensitive to refractive indices of the GeTe layer when compared to the s-polarized light. To achieve vivid reflective color for the unpolarized light, one can coat

the design with a polarizer to filter the p-polarization of the light and enhance the color contrast.

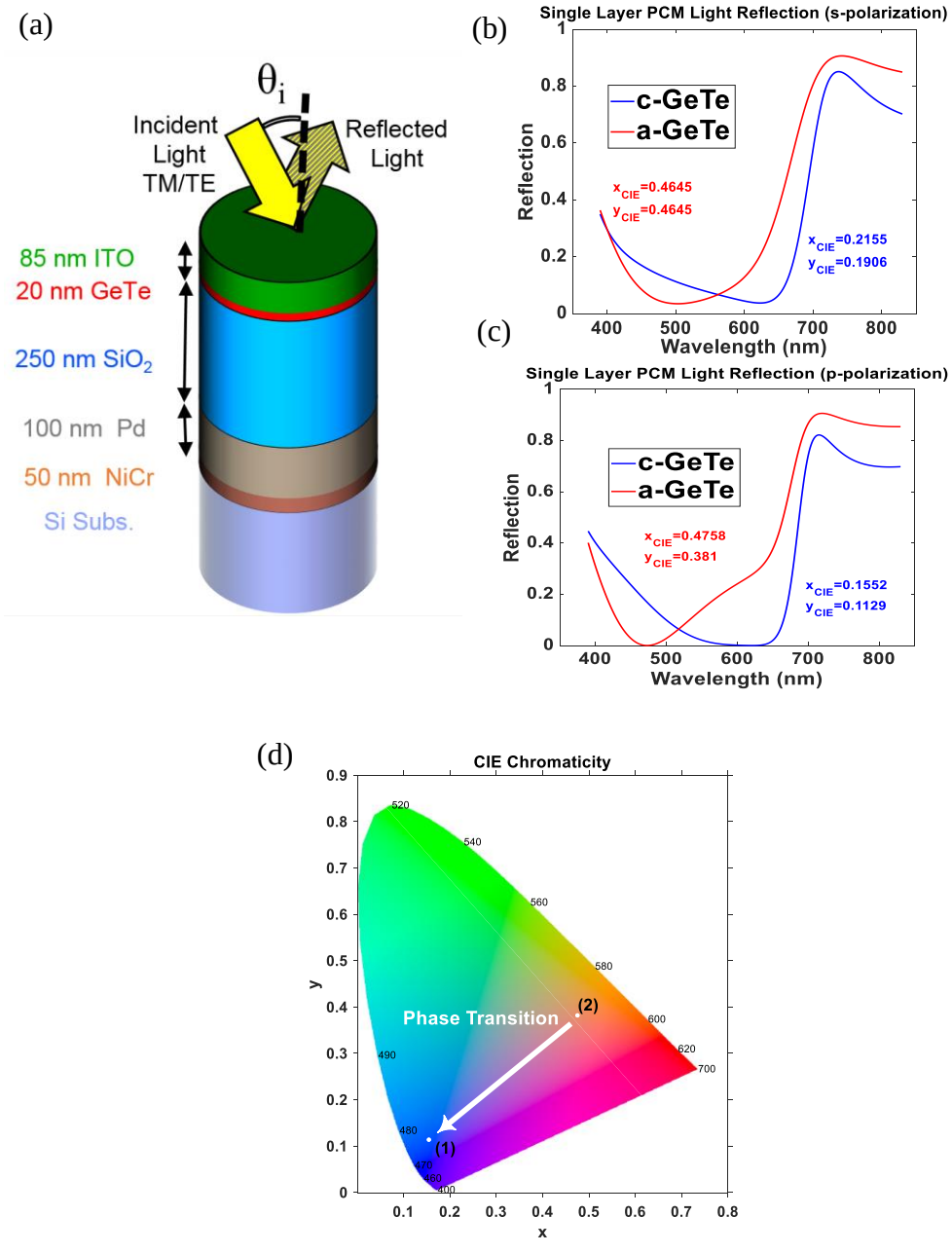

Figure 28. (a) The schematic of the single layer color reflector using 20 nm of GeTe film; (b, c) reflection of s (shown in b) and p (shown in c) polarized light for crystalline (blue) and amorphous (red) phases of the GeTe (insets show CIE chromaticity coordinates). Incidence angle of the light for all graphs is 45º. (d) CIE diagram for s polarized light showing the change in the reflected color due to phase transitioning of the GeTe.

## 4.4. Stack characterization and phase transition

As shown in Figure 28(d), vivid red and blue colors were achieved by using a very thin layer of PCM (GeTe) within a photonic cavity. The geometry of the design, especially the use of $SiO_2$ layer, helps to improve the sensitivity of the reflected light to the refractive index of the GeTe. This higher sensitivity results in higher color contrast that permits the use of a thinner layer of the GeTe with lower loss. The top ITO with a lower refractive index serves as an anti-reflection coating. The underlying palladium was used both as the bottom reflector and for the joule heating. When connected to gold contacts, the palladium film provides the heat that is required for phase transitioning of the GeTe layers by passing current. The indirect phase transition approach discussed here yields a device with higher reliability and less degradation, delamination, and film defects when compared to the direct heating method. The reflection of the single layer color reflector is measured using ellipsometry and plotted at different angles in Figure 29.

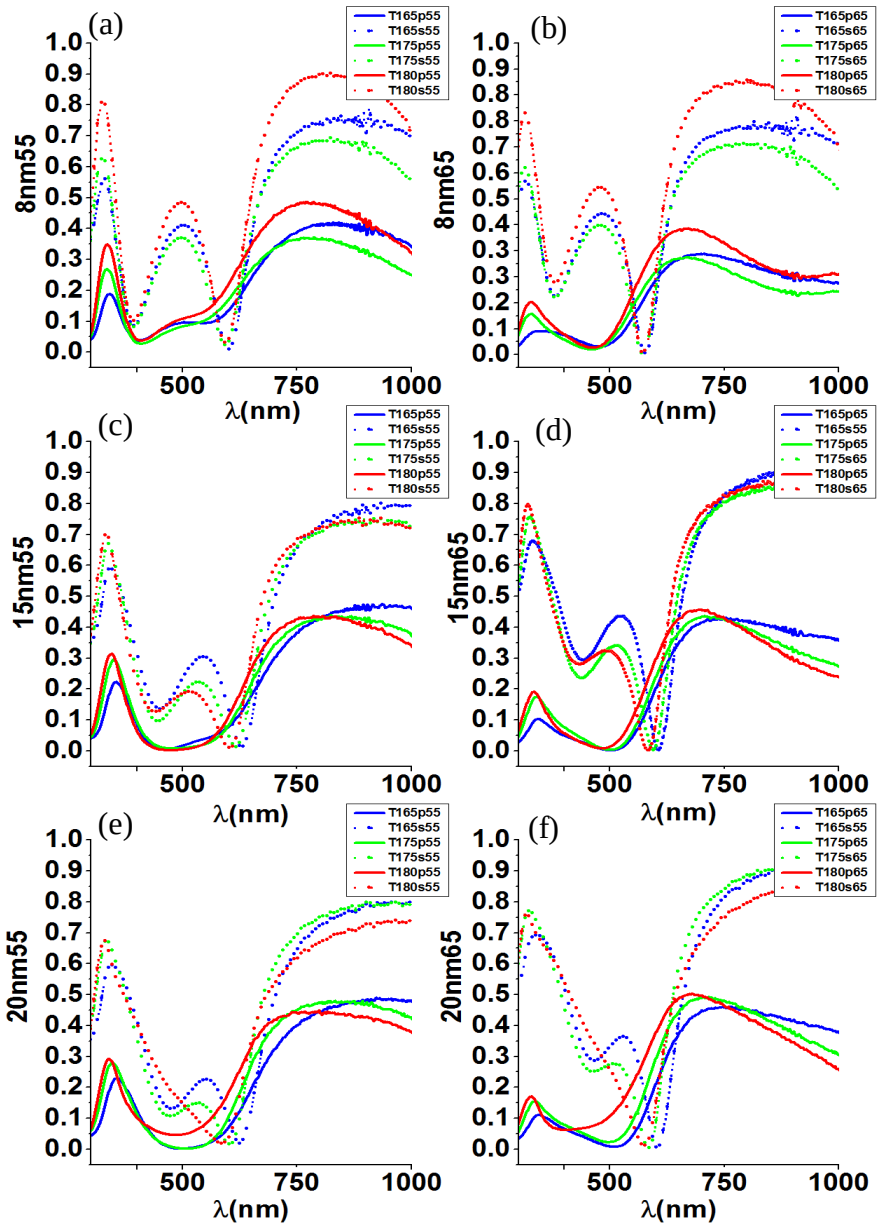


Figure 29. The reflection of the linearly polarized light (s polarization: dotted lines, p polarization: solid lines) of devices that consist of GeTe with 8 nm (a, b), 15 nm (c, d), and 20 nm (e, f) thicknesses when they are annealed to three different temperatures: 165 ºC, 175 ºC, and 180 ºC.

## 4.5. Thickness dependent crystallization of the thin GeTe film

The relationship between glass transition temperatures of the GeTe to its film thickness is an important consideration to enable phase transition of a selected GeTe layer in a device with multiple layer of GeTe. Here, this important feature of the GeTe films is used to selectively transition the GeTe layers between amorphous and crystalline phases in a stack that consists of two GeTe layer to produce 4 different colors. The thinner GeTe films have higher glass transition temperature as shown in Figure 30. The Tx of GeTe shows an increase as GeTe thickness is decreased for films thinner than ~ 20 nm. A substrate that consists of a 60 nm of $MgF_2$ anti-reflection (AR) coating on a GeTe layer with 8 nm, 15 nm or 20 nm thickness, a $SiO_2$ spacer of 250 nm , and a 100 nm thick Pd/NiCr reflector is used to verify this theory (Figure 30(a)). Each sample was heated to the target temperature in a 10-minute heating ramp time and was then annealed for 30 minutes at the target temperature. The samples were then cooled down in a slow cooling process that took 20 minutes to return to room temperature. Figure 30(b) compares the reflected colors of these sampled at room temperature and all at a10 degree angle after annealing. The Figure shows the reflected colors of devices with different thicknesses of GeTe films: 8 nm (top row); 15 nm (middle row); 20 nm (bottom row). Different shades of green, red, and blue colors were achieved for 8 nm, 15 nm, and 20 nm, respectively. Even though different shades of colors were seen during the partial crystallization of the film, full crystallization occurs at

different temperatures for GeTe films with different thicknesses. Figure 30(c) shows these measured Tx for a single layer color reflector with different GeTe film thicknesses. The thicknesses of the films were monitored using ellipsometry with a control sample after each sputtering. The surface morphology of the films was also studied using atomic force microscopy (AFM) to ensure that the GeTe layer sputtered over the plasma deposited silicon dioxide layer was uniform as shown in Figure 30(c). The surface roughness of the films was less than 1.5 nm for all sputtered films which verifies the high quality of the sputtering process. This roughness value is small enough to achieve a continuous film as thin as 8 nm which was used in this design. To reduce the roughness further, thermal oxide and slower growth of GeTe could also be considered. Figure 30(d) shows the in-situ X-ray diffraction (XRD) of this stack during the phase transitioning of the GeTe films with thicknesses of 8 nm, 15 nm, and 20 nm. To show the crystallization temperature tuning for different thicknesses of GeTe, several samples were analyzed when annealed to a temperature range of 170 °C to 190 °C inside a high-temperature stage filled with $N_2$ gas. An Ultima IV diffractometer (Rigaku Co.) is used to study the in-situ XRD of the crystal structures. Fully crystalline GeTe creates a distinctive peak in the XRD intensity pattern at 2tetha angle of 30 degrees. As shown here, the peak located at 2tetha equal to 30 degree appears at a higher temperature for a thinner GeTe film compared to those measured for a 20 nm thick GeTe (shown with the horizontal dashed lines).

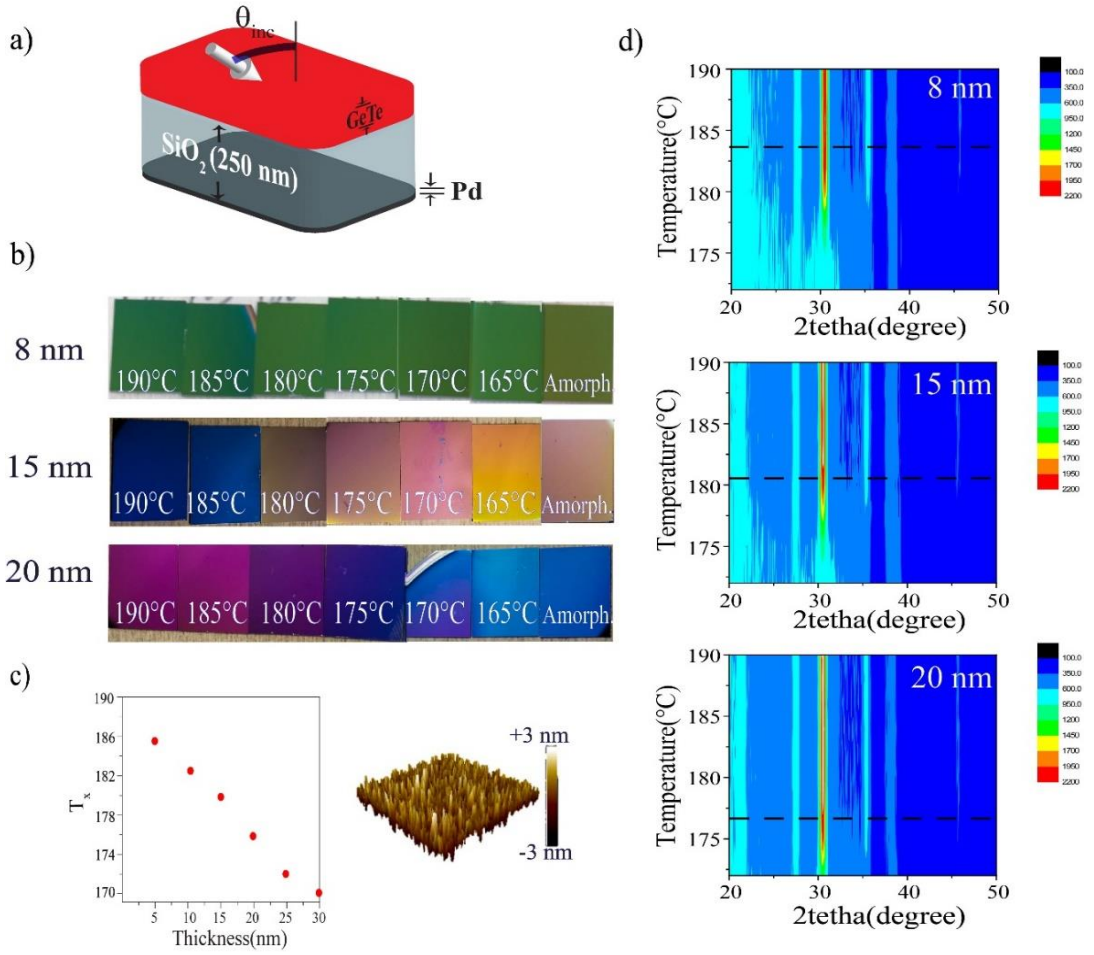


Figure 30. (a) The device structure used for measuring the glass transition temperature vs. thickness of GeTe consists of GeTe, $SiO_2$, and a bottom Pd reflector. (b) The reflected color of the sample at different temperature for GeTe with thickness values of 8 nm (top), 15 nm (middle), and 20 nm (bottom). (c) The shift in the Tx for different thicknesses of the GeTe film (Inset: surface morphology using AFM that shows <1.5 nm roughness). (d) The color-coded in-situ XRD patterns for different thicknesses of the GeTe film: (top) 8 nm, (middle) 15 nm, and (bottom) 20 nm at a temperature range between 170 °C and 190 °C. The

black horizontal dashed lines inside the color XRD patterns show complete crystallization for each film (the crystallization peak at 2theta ~ 30˚).

To achieve a better annealing process, several samples were annealed at different temperatures (165ºC to 190ºC) in a convection oven with a steady nitrogen gas flowing inside it. The change in the Tx for different thickness of the GeTe film is most likely due to the difference in the residual stress, which is applied from the rest of the stack. Moreover, GeTe layers with different thickness values experience different residual stress within themselves. PCM films that are under residual stress exhibit different phase transition temperatures than those under no stress, as reported previously in Ref. [4.31]. For the same reason, a highly stressed GeTe film with a thickness larger than 25 nm has a lower phase transition temperature as shown in Figure 30(c).

The applied current to reach the phase transition temperature is specific to each of the different types of metallic heaters and the type of metal that is used for the pads. For the heaters made out of Pd that are connected to the gold pads with a resistance of ~80 Ω, full crystallization of both layers is achieved at 186 ℃ by applying pulses of ~1 V magnitude. No damage is observed in the heater or the film stack with more than 2000 pulses repeatedly applied to the device.

## 4.6. Multi-layer color reflector

### 4.6.1. Design and modeling

Using more than one layer of the GeTe within an optical cavity provides more than two states for the whole structure from only two stable phases of the GeTe films. For example, devices with two GeTe layers demonstrate four stable room temperature (25°C) states: both GeTe layers are amorphous (AA); the top layer amorphous and bottom layer crystalline (AC); top layer crystalline and bottom layer amorphous (CA); both layers are crystalline (CC). One can achieve multiple stable states at room temperature by increasing the number of GeTe films. Expanding the same idea that is used for single layer color reflector, one can achieve a multi-color reflective device by integrating more than one layer of GeTe film within the cavity as shown in Figure 31. The top $MgF_2$ thin film reduces the reflection from the top surface and thus increases the color contrast by matching the top air to the $TiO_2$ film impedance that is positioned directly underneath. The cavity was closed on the bottom side by a reflective palladium film and a thin NiCr adhesion layer. Using an indirect heating approach, selective phase transition was achieved for each layer of GeTe. This will consequently produce multiple reflective colors from the surface of the device. In this indirect heating scheme, the current was passed through another resistive film and produced the heat required for crystallographic phase transition. This indirect approach results in better reliability and repeatability for the phase transitioning of the GeTe films.

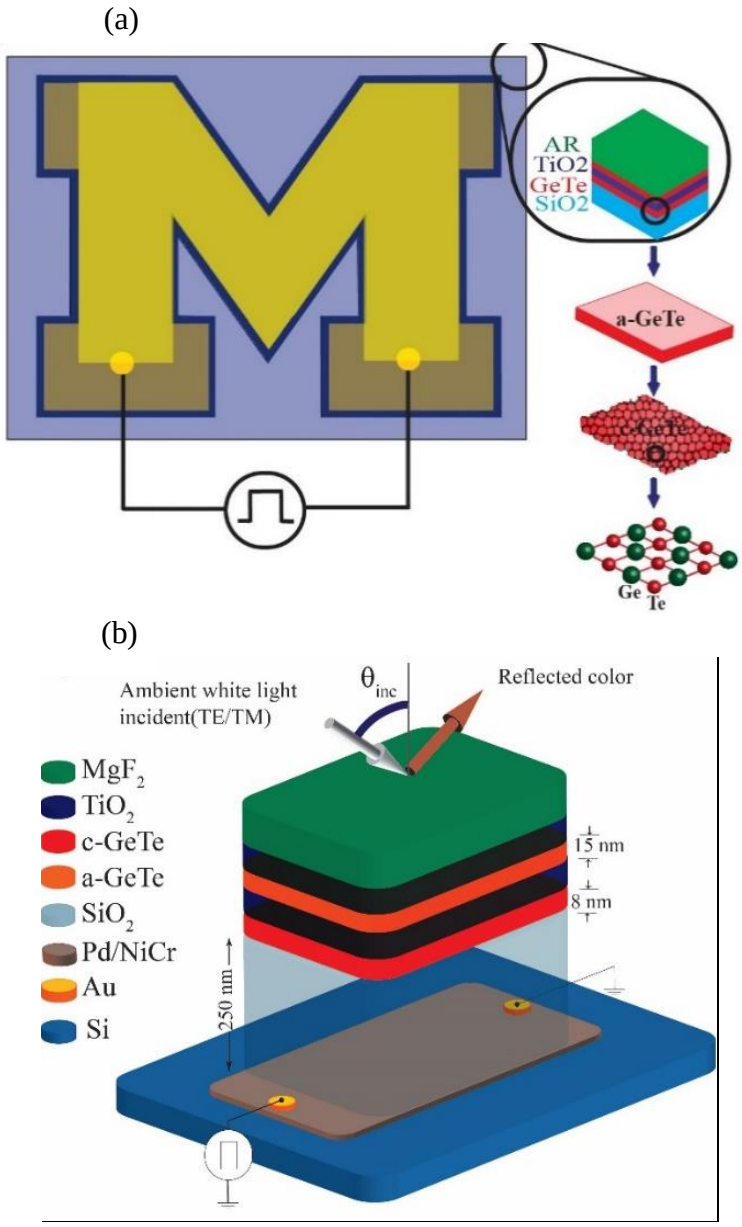


Figure 31. (a) The top view of the device that shows the "M" sign heater under multi-layer stack. (b) The schematic of the device that includes all the layers and the 250-nm $SiO_2$ phase shifter.

The electromagnetic response of the device is simulated using FEM modeling (COMOSL Multiphysics ®). Device reflection spectra in each of the four different states are shown in Figure 32. Both reflection and absorption are shown for each of these four states. As shown below, the device supports a wide absorption in the 450 nm to 675 nm range. This wide range of absorption is created by the thin film resonance located at these two wavelengths. The wide absorption window, which is located exactly at the edge of blue and red colors, increases the device color sensitivity to modulation of GeTe refractive index by the tuning of two ultra-thin GeTe films integrated in the structure. The reflection peak located at 550 nm appears when the bottom GeTe layer is amorphous and is not dependent upon the phase of the top layer. In the amorphous state, light propagates through the optical phase shift layer between the bottom GeTe layer and bottom reflector of the cavity (Figure 31(a)). The reflected light is green in color when the top GeTe layer is crystalline and absorbs most of the red color. This green color is most visible when the bottom layer is amorphous. When both top and bottom films are amorphous, a large reflection of red color is produced. The peak located at 380 nm is fixed within the structure and provides reflection of blue color, which is only visible when both films are crystalline and are absorbing the remainder of the spectrum as shown in the first state. The electric and magnetic fields of these different modes are shown in Figure 33 for different wavelengths in visible range.

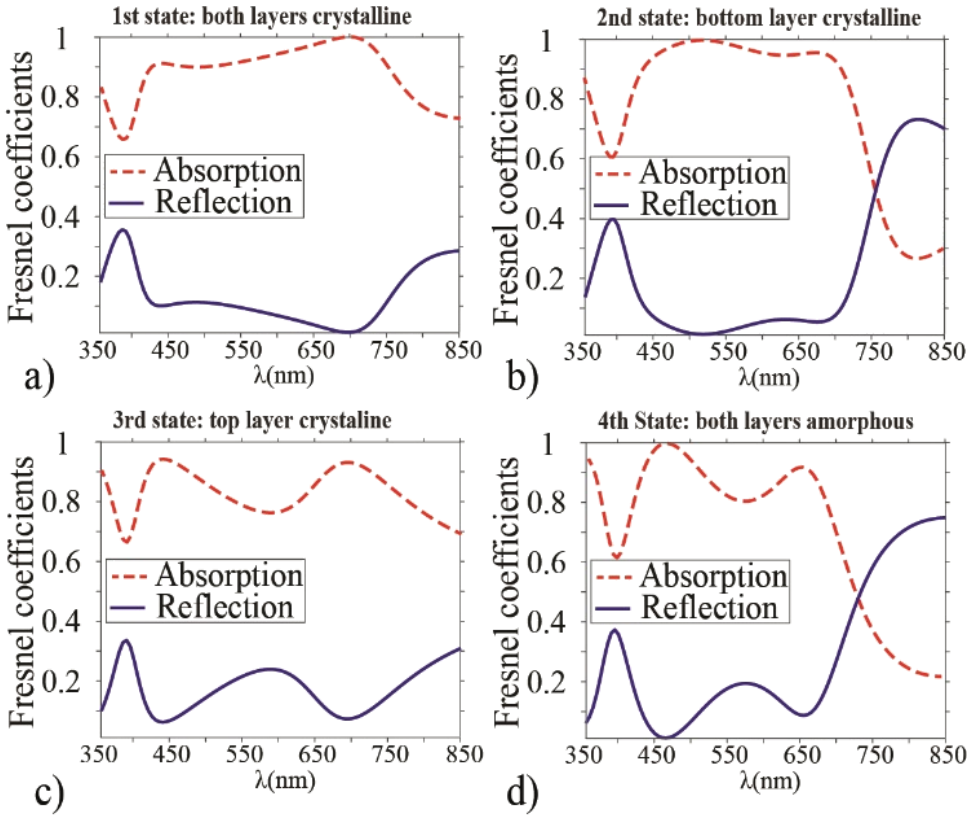


Figure 32. Theoretical modeling of absorption and reflection spectra for four different states of the device in the visible range.

As shown in Figure 33(c), for an effective reflection of red color, the structure must support a peak in electric field at the position of the top GeTe layer. The absence of properties necessary to support a peak when the top layer is crystalline (first and third states) diminishes the red color reflection from ~70 % to 30 %.

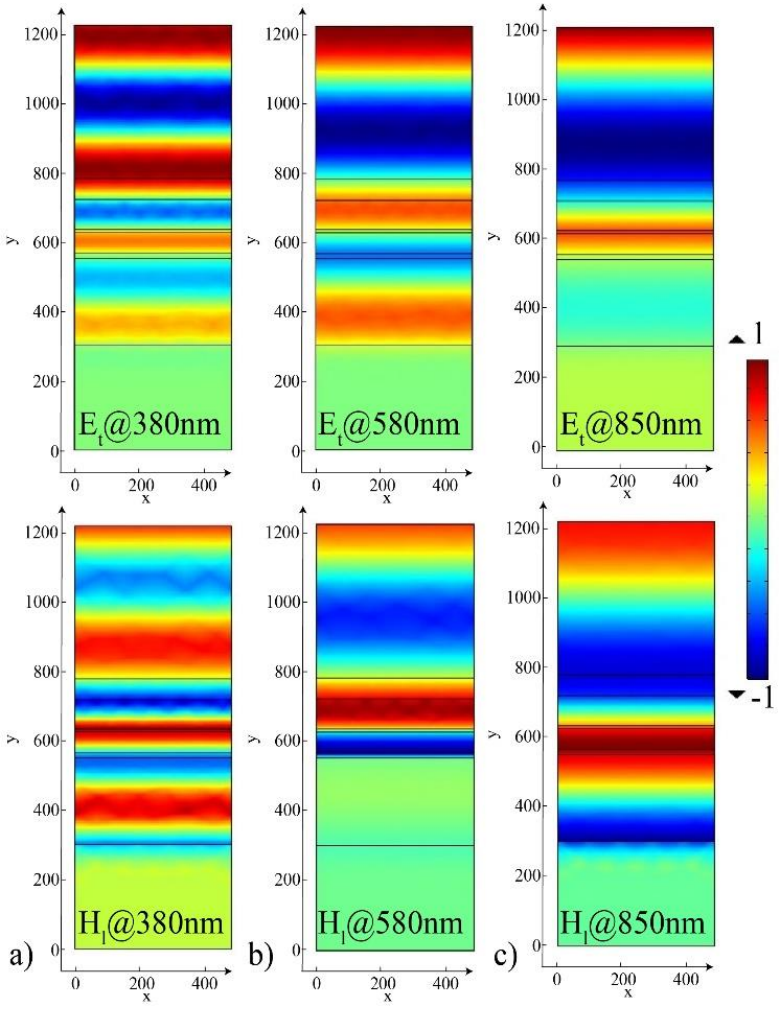


Figure 33. Patterns of normalized electric (top) and magnetic (bottom) fields shown for the cross-section of the device at wavelength of 380 nm (a), 580 nm(b), and 850 nm(c); blue (red) regions represent the minima (maxima) of each field when GeTe films are amorphous.

This decrease produces majority blue and green colors in these two states with a top layer that is in the crystalline phase. The green colors are most easily seen by a human eye due to greater sensitivity of green cone cells, as further explained in the next section. The multi-layer device reflections in all four states are shown in Figure 34 (a-d). Due to high reflectivity of the top GeTe layer when it is crystalline, the tunability is very significant for the CC and CA states (see Figure 34 (a and b)). However, this cavity response dependency on the $SiO_2$ layer is clearly shown for the case of AC and AA states when the top GeTe layer is amorphous in Figure 34 (c, and d). Figure 34(c) shows how the reflection peak is tuned with different phase shift layer thicknesses.

For the case of $SiO_2$ with 250 nm thickness, this peak is located at ~ 700 nm, causing the maximum color dynamic dependency on refractive indexes of GeTe layers. As shown in Figure 34(d), the peak exists at the same wavelength for both AC and AA states. The position of the peak is not tunable with GeTe phase transitions as the mode is more confined in when the bottom layer is crystalline (AC state as shown in Figure 34(c)).

Adding more layers to this equation allows multiple thin film resonances within the visible wavelength depending on the thicknesses of the different layers. The total device reflection in different states of the GeTe layers (CC, CA, AC, and AA) when bottom $TiO_2$ (with nominal thickness of 60 nm) layer thickness is varied between 40 nm to 100 nm is shown in Figure 35. The change in the thickness of bottom $TiO_2$ layer which separates the two GeTe layers has a higher impact on tuning the light reflection at the visible region.

This figure shows that the multi-layer device supports three thin film resonances within the visible region. The wavelength of these near perfect absorptions depends on the thicknesses and refractive indices of each layer. Thus, tuning the refractive index of the GeTe layers results in multi-color by tuning the position of these reflection dips. The shift in the wavelength of these dips, when GeTe undergoes phase transitions depends on the $TiO_2$ spacer that is sandwiched between GeTe layers, the $SiO_2$ phase shifter layer, as well as the top antireflection coating. However, it is clear that the maximum color sensitivity to $TiO_2$ thickness is when both GeTe layers are amorphous and thus less lossy (see the oblique line in Figure 35(d)).

The other dip which is located at 380 nm is attributed to the top GeTe layer, which is why it exists in all four states. The corresponding reflection dip and the peak at 400 nm are not significantly tunable with GeTe phase transition due to low contrast in the real part of the refractive index. However, by switching the state of these thin GeTe films from crystalline to amorphous, its refractive index is modulated and subsequently the amount of reflected red color could be enhanced. This results in a reddish color reflected from the surface of the device.

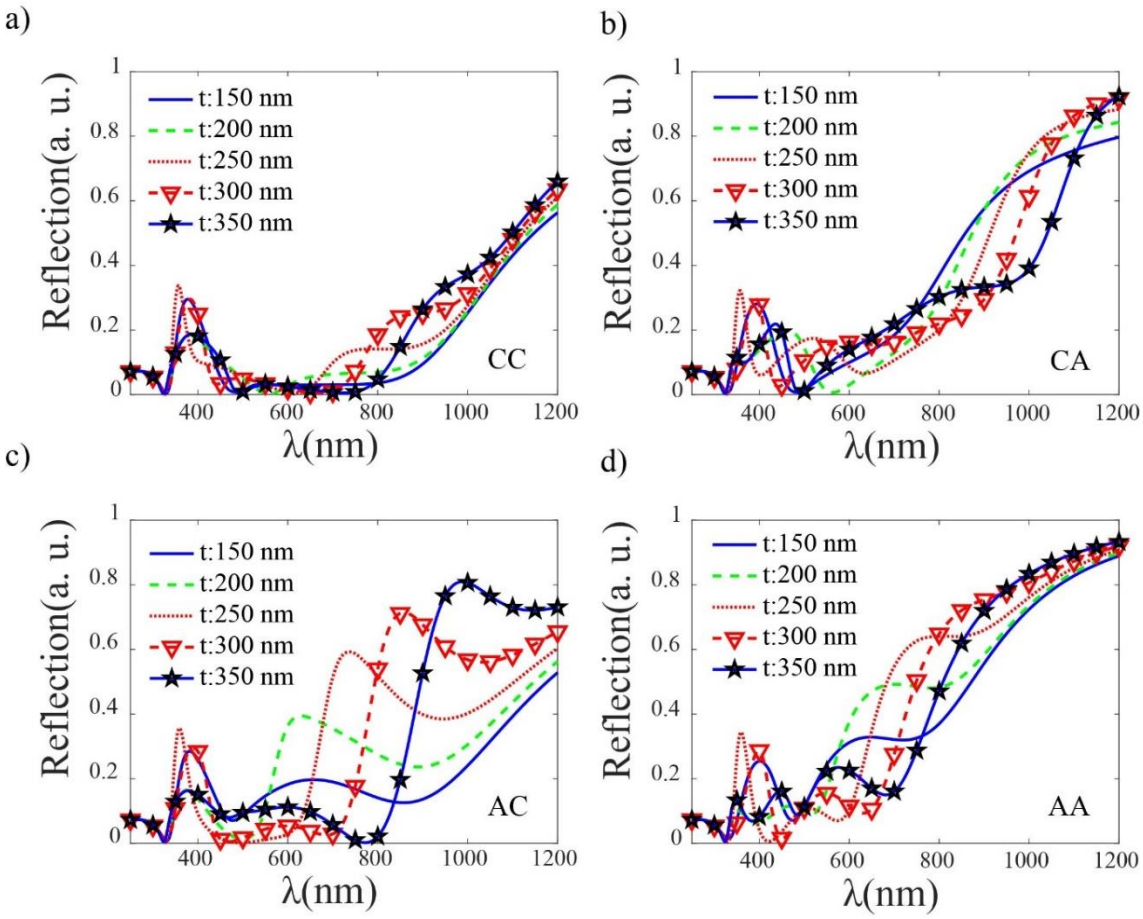


Figure 34. The reflection device at vis-NIR region with different thicknesses of the $SiO_2$ (Incident angle: 50º).

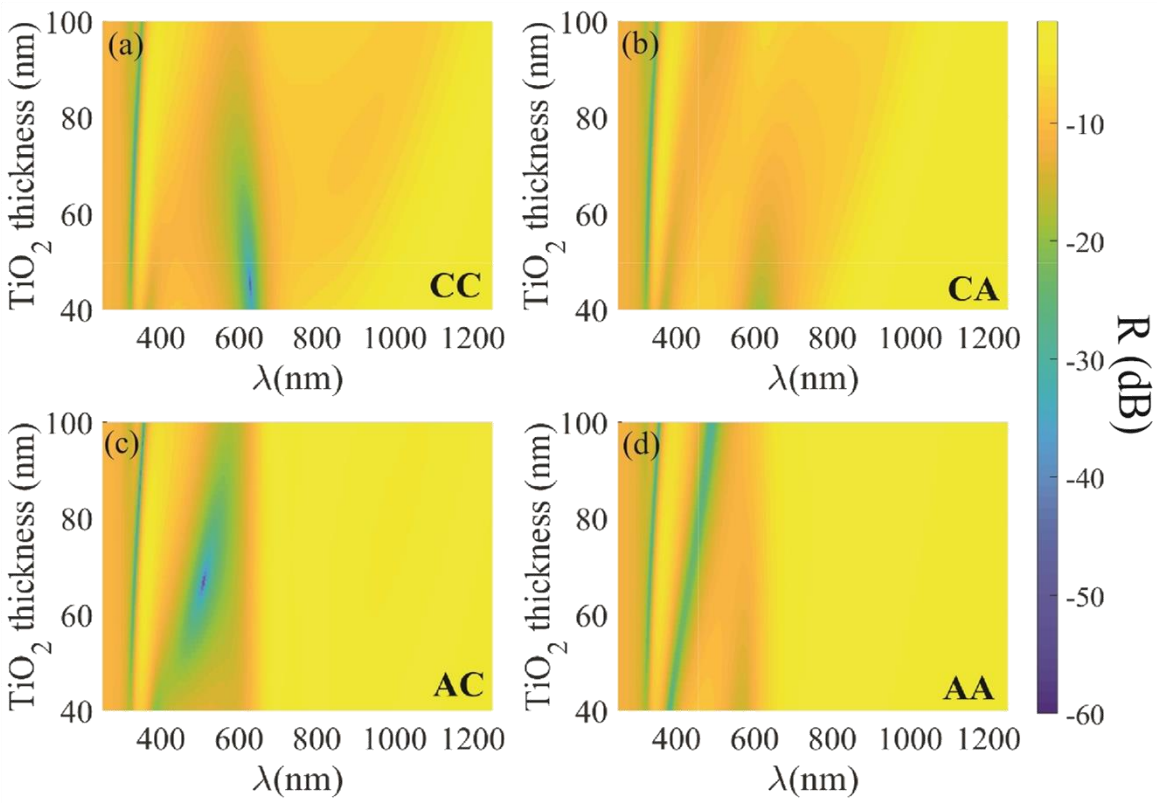


Figure 35. The reflection of the multi-layer device in the logarithmic scale to show the thin film resonances with different thicknesses of the bottom $TiO_2$ layer. The dips in the reflection spectra correspond to the total light absorption, which is mostly visible when both GeTe layers are amorphous (shown in d) with almost 50 dB absorption within the visible wavelengths at 50° incident angle.

### 4.6.2. Selective phase transition of the thin films

To demonstrate the selective transitioning of GeTe films within the stack using joule heating, a thermal model is studied employing FEM. Temperature dependent densities,

heat capacities, and thermal conductivities measured or estimated experimentally were incorporated into the model for crystalline and amorphous states. Figure 36 shows the required temperature distribution within the stack in order to achieve four different states mentioned in the main paper. Slow CA pulse with 1 μs pulse width and 200 nm rise and fall times heats the whole stack to 175 °C which only transitions the top thick layer; the fast CA pulse with 50 ns rise time and 500 ns duration heats the bottom layer to 183 °C and crystalizes it. The top GeTe layer is kept at 166 °C, well below its Tx in the amorphous state. The CC state is achieved by a slow 1 μs pulse and higher amplitude to heat up the whole stack to 186 °C above the Tx of both GeTe layers.

The power consumption for full crystallization (CC) is 12.5 mW for each arm of the "M" sign with an area of $200 \times 10\ \mu m^2$. The experimental crystallization pulse for CC state is 1 μs long with a 50% duty cycle (with total period of 2 μs). Therefore, total energy consumption for each crystallization event is 12.5 nJ. The stack discussed here is more susceptible to degradation during the amorphization process (AA) because of the higher temperature needed. The 500 ns voltage pulses of 20 V are used for resetting the devices to their original color (AA). Devices consisting of films with lower contamination showed several reset cycles. The total energy consumption for each reset process for the area mentioned above is 200 nJ, which is due to the lower resistance of the heater after crystallization of the GeTe layers. The CA state was achieved with application of 0.9 V pulses applied for 1 μs with a period of 2 μs heating the device to ~ 175 ºC. This would

keep the thicker top GeTe layer in the crystalline state and thin bottom layer in the amorphous state. On the other hand, the AC state is achieved by applying a faster pulse with 500 ns width (period: 1 µs) and 1 V amplitude, while keeping the top layer in the amorphous state.

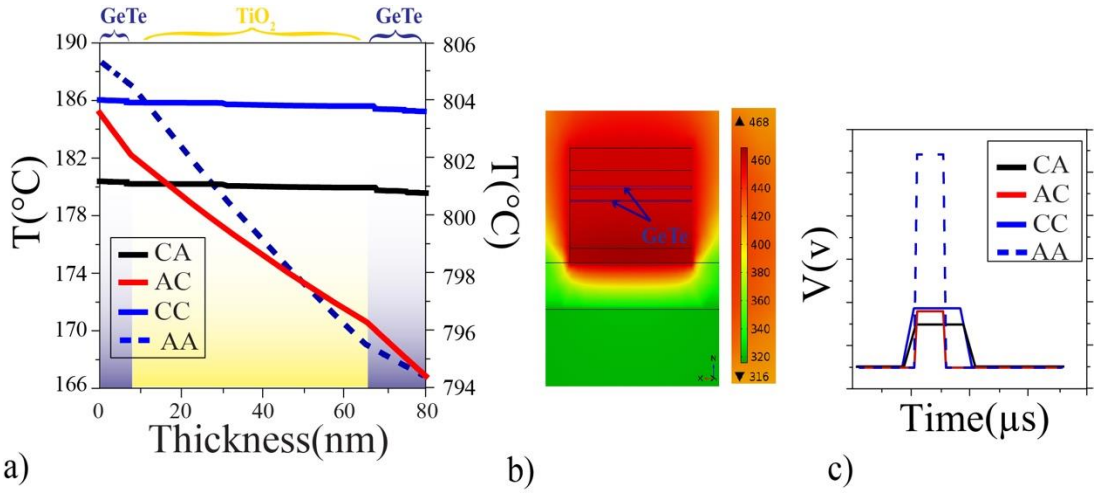


Figure 36. Temperature profile versus thickness within the stack of the films between two GeTe films (b) Temperature profile within the stack for AC state. (c) Four different voltage pulses used to achieve AA, AC , CA , and CC states (the vales are not to scale).

These temperature profiles were achieved by applying the voltage pulses across the Pd heater underneath the stack of the films. Different pulses are used to achieve AA, AC, CA, and CC states and are also demonstrated in Figure 36(c).

### 4.6.3. Fabrication and results

The fabrication starts with pattering of the first metal layer on a single side polished silicon wafer. A 100-nm-thick palladium film with a NiCr adhesion layer with 10 nm thickness are evaporated and patterned using the lift-off process. The phase-shift oxide layer is deposited using a Plasmatherm 790 PECVD tool (Plasma-Therm Co.) at 200 ºC with a rate of 7.5 Å/s. Then a GeTe film with 15 nm thickness is sputtered using a LAB-18 deposition system (Kurt J. Lesker® Co.) from a 3-inch $Ge_{50}Te_{50}$ target (Mitsubishi Material Co.) using $Ar^+$ carriers at a rate of 0.66 Å/s at room temperature. Deposition at an ultra-low rate improves the film uniformity to achieve an amorphous film with low loss at visible region. The $TiO_2$ separators are evaporated using a SJ-20 evaporator at room temperature and $2\times10^{-6}$ torr chamber pressure. An antireflection coating consist of $MgF_2$ film is also evaporated using the same SJ-20 system with an ultra-low deposition rate of 0.4 Å/s to reduce the stress.

The parameters of $MgF_2$ deposition are tuned to achieve a stable, low-loss and low-stress film at room temperature. Two main challenges in the previous designs that consist of GeTe were the integration of the heater and the selection of a material with proper resistivity and thermal stability. NiCr film, which is a thermally stable material with resistivity of $150 \times 10^{-8}$ Ω.m, is used as the heater which is underneath the palladium reflector. As mentioned previously, using refractory metals such as Pd instead of unstable

noble metals, these devices show improved reliability and a higher number of successful transitioning cycles.

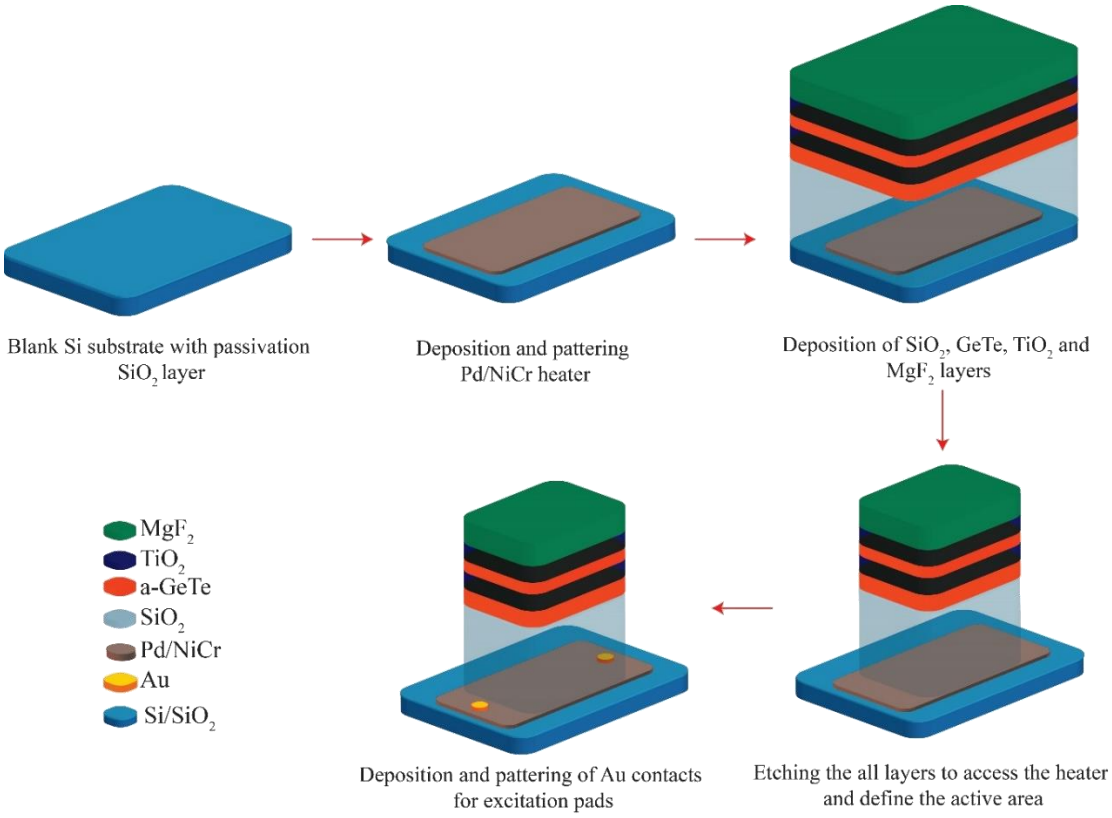


Figure 37. The fabrication process that is used to make the tunable color reflector with two layers of GeTe

The reflection measurements were performed by using a Woollam M-2000 spectroscopic ellipsometer (J.A. Woollam Co.). The reflection spectra of the device for the un-polarized light and incident angle of 50° in all four states are shown in Figure 38. The

experimental data confirms the model that was used for the simulation of the device for all four states. Figure 38 (b) shows the “M” sign with maize color (left) and blue color (right) in AA and CC, respectively.

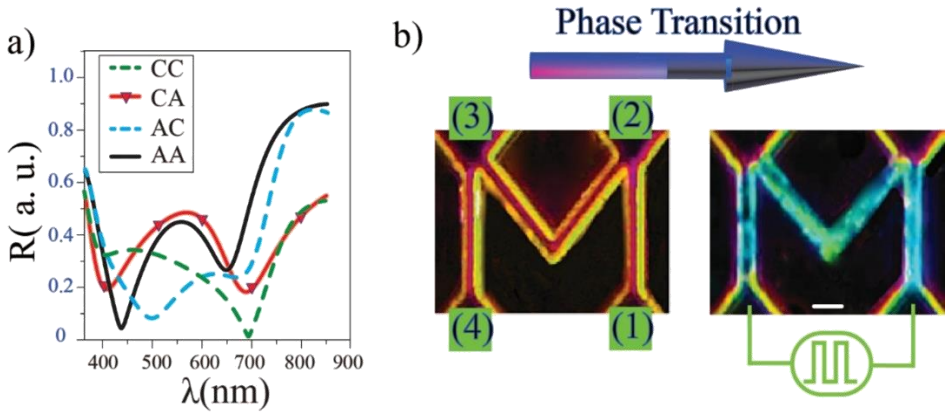


Figure 38. The reflection spectra for the proposed color reflector in its four different states for un-polarized light with the angle of incident of 50°. The reflection of the device in all states are measured at room temperature and in the ambient light.

The reflective color of the device with two layers of GeTe films is extracted by using the CIE-1931 standard and its chromaticity graph as shown in Figure 39. Four distinct colors are shown here by switching the phases of the two GeTe films separately. These colors consist of dark blue, green, orange and red, which are indicated by CC, CA, AC, and AA in the CIE graph (see Figure 39) [4.32].

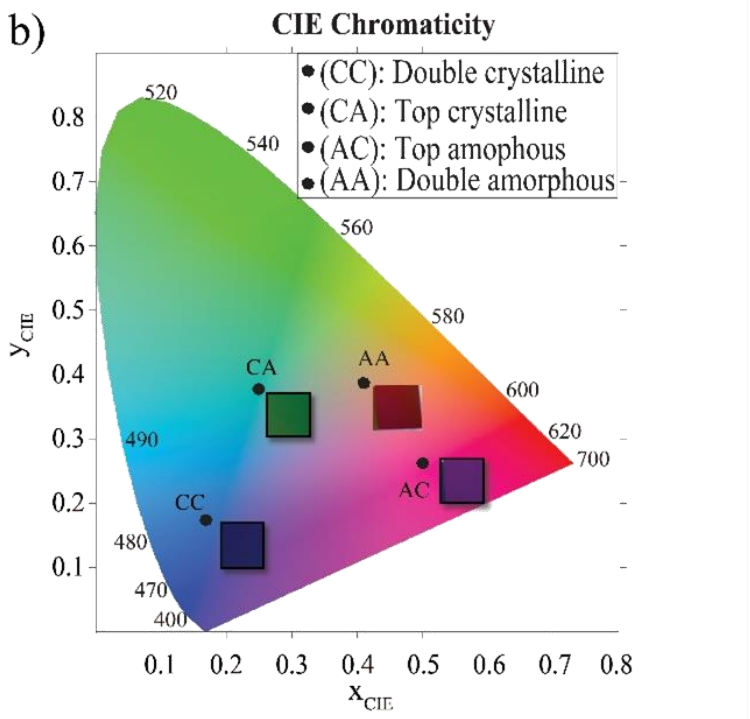


Figure 39. The reflection color of the multi-layer tunable color reflector extracted from the reflection spectra and plotted on a CIE chromaticity graph. The boxed areas show the actual color of the device at different phases for each layer of the GeTe films.

Utilizing such an approach, we demonstrated four different colors for the left arm of the "M" sign as shown in Figure 40. Having four different pads to apply electrical pulses, permitted partial phase transitioning for the left arm. Figure 40 (a) shows the color change when the ports that are labeled by (1) and (3) are excited by an electrical pulse. Thus, only

the three arms in between these ports experience a color change (transitioned to CC state). This device is then used to show four different colors in the left arm of the “M” sign. Figure 40 (a-d) shows four different colors: red-pink, yellow, and green-blue, and blue for the left arm of the “M” sign when the bottom pads were excited and current was flowing through the “M” sign. The energy consumption per each transition is different for each part of the “M” sign due to resistance change of the arms after phase transition. One can abruptly change the total color of the “M” sign by applying the voltage pulse to the bottom excitation pads (pads labeled “(1)” and “(4)” in Figure 39 (b)). Smaller voltage pulses are required for abrupt color changes because the resistance of the whole heater is changing abruptly with a single pulse. The sequential process, on the other hand, needs sequential excitation of the pads starting with right and middle arms (Figure 40 (a)), using bottom right pad (1) and top left pad (3) (see Figure 39 (b)), and finally bottom pads that are labeled as (1) and (4).

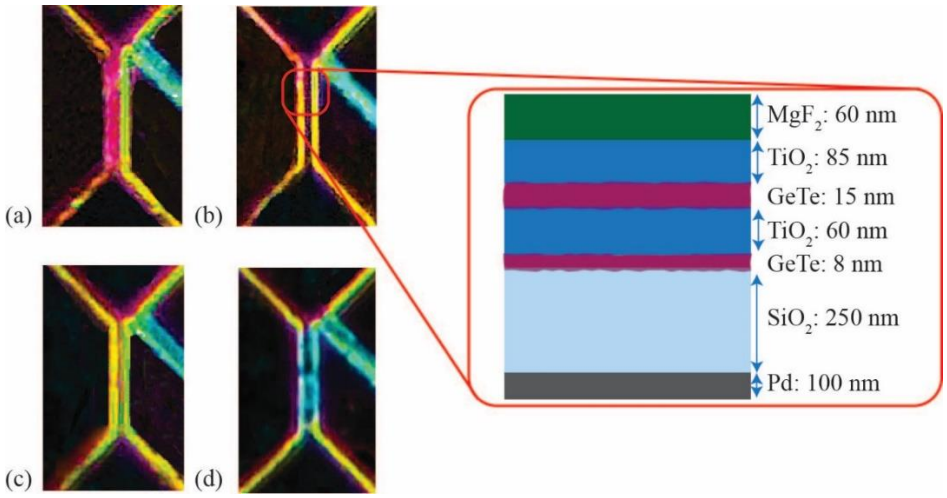


Figure 40. The transition of the reflected colors for the left arm of the "M" sign, when the device is excited from the port (1) and (4); (a): Right and middle arms were already transitioned to CC state and both GeTe layers are still amorphous in the left arm (AA); (b and c): Two intermediate states were achieved by applying controlled voltage pulses between port (1) and (4) to transition the left arm to AC (b) and CA (c) states, respectively. The other three arms were kept at CC state with higher conductivity during these transitions. (d): Finally, the left arm is transitioned to CC states from (c), after this transition the color of the left arm is matched to all other three arms, which were kept at CC state during all these transitions with no damage to the heater. These images were digitally zoomed due to limitation of the optical zoom.

### 4.6.4. Angle sensitivity and reliability

The reflection spectra versus the incident angles is measured using ellipsometry and the calculated CIE coordinate variation is shown in Figure 41(a) to illustrate the color change versus angle. The same coordinates are plotted versus angle of incidence in

Figure 41(b). The total crystallization energy is summarized in Table 4.1 for each arm for both sequential and abrupt color change. The total energy to change the color of all four arms is obviously higher in sequential process. This table also shows different combination of excitation ports used to partially crystallize each arm of the "M" sign.

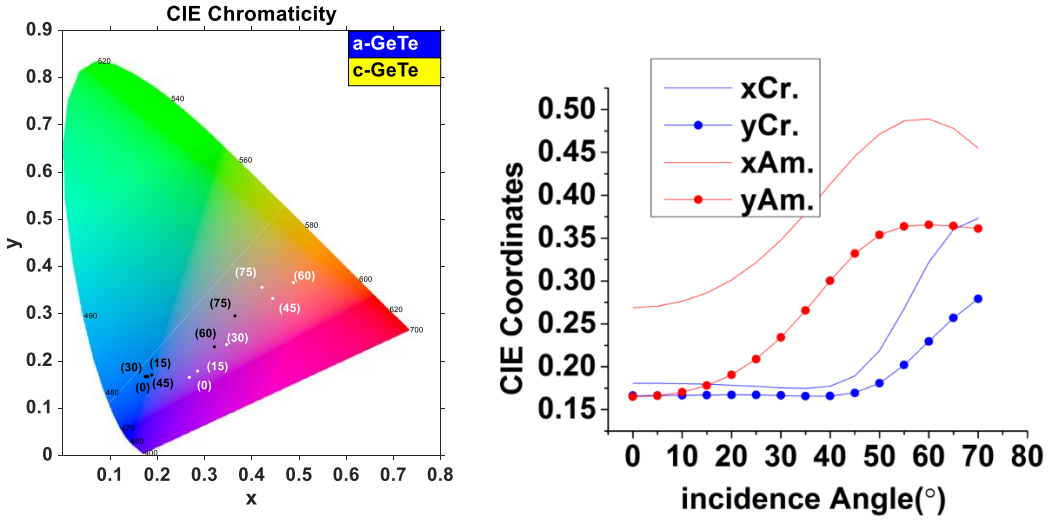


Figure 41. (a) The experimental data demonstrating angle sensitivity of the reflective colors for both phases of the GeTe layer from spectroscopic ellipsometry (white dots represent the amorphous phase and black dots show crystalline GeTe at the room temperature). (b) The variation of the CIE standard coordinates versus incident angles for designs that consist of GeTe films with amorphous (Am.) and crystalline (Cr) phases.

Table 4.1. The energy consumption of the phase transition and the resistance of the heater for sequential and abrupt color transition of the “M” sign.

| | Transitions | Excitation ports | $R_0$ (Ω) | $R_{post\text{-}cryst.}$ (Ω) | E (nJ) |
|---|---|---|---|---|---|
| Sequential | Right Arm | (1) and (2) | 80 | 50 | 25 |
| | Right & middle arms | (1) and (3) | 150 | 98 | 8.2 |
| | All Arms | (1) and (4) | 180 | 125 | 11.2 |
| Abrupt | All Arms | (1) and (4) | 220 | 124 | 11.6 |

The reliability of the color reflector is an important factor in its long-term performance. The device under test (DUT) was connected to a pulse generator to simulate accelerated aging. Several hundreds of pulses were applied to the device and the color tunability of the device was analyzed after testing using ellipsometer spectroscopy. The (x,y) coordinates of the samples after different numbers of applied pulses are shown in Figure 42. As shown below, the device performance remains the same after hundreds of pulses are applied to it. “X” and “Y” coordinates did not show much variation, even after 200 pulses were applied to the heater for each of the four different states (with 800 total number of pulses). The bottom layer was crystallized with the application of 0.9 V and the top layer was crystallized with the application of 1.2 V. The reset pulses were applied to the device with the magnitude of 6.5 V. The heater was also tested and found to tolerate 20 V high voltage operation before any device failure could occur. The experiment was stopped due to time constrains (it takes a significant amount of time to take ellipsometry and convert the data to CIE coordinate) and the device was still functional after 800 cycles.

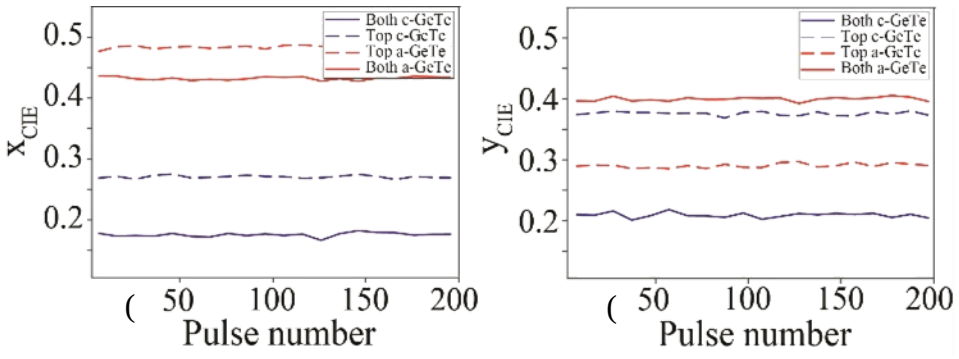


Figure 42. The variation of the CIE coordinates with up to 200 number of pulses applied to the heater. XCIE and YCIE coordinates are shown in (a) and (b) respectively with minimum degradation to prove the reliability of the colors.

## 4.7. Waveguide Grating Color Reflector

### 4.7.1. Design and modeling

An array of GeTe nano-slits were employed in an optical waveguide grating design (Figure 43) in order to enhance the reflected color dynamic, reduce the loss, and ease the electrical switching. A thin transparent silver film with low resistivity [4.33], which was passivated by a 3-nm $SiO_2$ spacer, was developed to withstand high temperatures and was placed adjacent to GeTe gratings to serve as the localized joule heater. The refractive index modulation through joule-heating utilizing this thin silver film is demonstrated for the first time to achieve different colors from a-GeTe and c-GeTe. Additionally, the resonant modes

of the asymmetrical Fabry-Perot cavity are used to enhance the color contrast when ultra-thin GeTe film (thickness <λ/16) undergoes this phase transition.

Figure 43 shows the device structure, which consists of an optical waveguide between a bottom metallic reflector (Pd) and the top GeTe grating. The waveguide consists of a $Si_3N_4$ core, which is encapsulated by $SiO_2$ cladding on either side. The waveguide is closed by a thin film silver (12 nm) under the GeTe grating. This silver film also serves as the conductor needed for the joule heating approach. There is a thin (2 nm-3 nm) wetting layer under Ag film for better stability and uniformity at higher temperature. Recently it is found that plasmonic metals diffuse into the PCM layer, which results in degradation of the film and reducing the number of switching cycles [4.34]. Thus, the thin Ag film is passivated by a ~ 5-nm sputtered oxide film to improve the number of the phase transitioning of the GeTe film by reducing the inter-diffusion of the silver atoms into the PCM film.

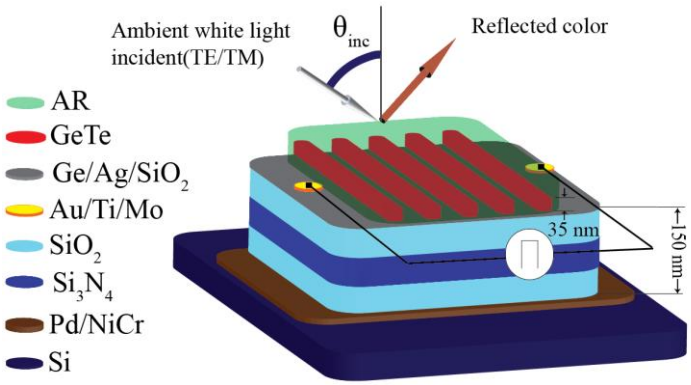


Figure 43. Schematic view of the device utilizing waveguide grating.

The top magnesium fluoride ($MgF_2$) (80 nm) and $TiO_2$ (60 nm) films function together as anti-reflection layers for the 40-nm GeTe grating below to ultimately improve the color contrast. The GeTe grating could be modeled with an equivalent isotropic dielectric with effective refractive index $n_{eff}$ to simplify the design. The effective permittivity of the sub-wavelength grating can be derived using the effective medium theory [4.35]:

$$\varepsilon_{\parallel} \approx f\varepsilon_1 + (1-f)\varepsilon_2, \tag{4-14}$$

$$\varepsilon_{\perp} \approx \left(\frac{f}{\varepsilon_1} + \frac{1-f}{\varepsilon_2}\right)^{-1}, \tag{4-15}$$

where $\varepsilon_{\parallel}$ and $\varepsilon_{\perp}$ are tangential and orthogonal part of the permittivities. f is the filling factor defined as a/p where a is the line width and p is the period of the grating. Optical refractive indices of the grating in tangential $(n_{\parallel}, k_{\parallel})$ and orthogonal $(n_{\perp}, k_{\perp})$ directions are then derived such as:

$$n_{\parallel} \approx \sqrt{\frac{|\varepsilon_{\parallel}|+\varepsilon_{\parallel}^{r}}{2}}, k_{\parallel} \approx \sqrt{\frac{|\varepsilon_{\parallel}|-\varepsilon_{\parallel}^{r}}{2}}, \tag{4-16}$$

$$n_{\perp} \approx \sqrt{\frac{|\varepsilon_{\perp}|+\varepsilon_{\perp}^{r}}{2}}, k_{\perp} \approx \sqrt{\frac{|\varepsilon_{\perp}|-\varepsilon_{\perp}^{r}}{2}}, \tag{4-17}$$

$|\varepsilon_{\parallel,\perp}|$ here is the complex modulus, which defined as:

$$|\varepsilon_{\parallel,\perp}| = \sqrt{\left(\varepsilon_{\parallel,\perp}^{r}\right)^2 + \left(\varepsilon_{\parallel,\perp}^{i}\right)^2}, \tag{4-18}$$

and $\varepsilon_{\parallel,\perp}^{r}$ and $\varepsilon_{\parallel,\perp}^{i}$ are the real and imaginary parts of the permittivity, respectively. Using (4-16) and (4-17), the grating could be modeled as a uniaxial dielectric slab to simplify the

design when the period is much smaller than the wavelength ($p<<\lambda$). The total transfer matrix of the structure is then derived by multiplying the wave matrices of all layers such as:

$$M_T = \begin{bmatrix} e^{\beta_n} & r_{n,n+1}e^{\beta_n} \\ r_{n,n+1}e^{-\beta_n} & e^{-\beta_n} \end{bmatrix}, \tag{4-19}$$

where $\beta_n = ik_nt_n$ is the electric thickness of the nth layer. $k_n$ here is the wavevector which is defined as $n_n \times \cos(\theta)$ for s-polarization and $n_n \times \cos(\theta)^{-1}$ for p-polarization of the light. $r_{n,n+1}$ is also Fresnel coefficient of reflection of the nth interface defined as:

$$r_{n,n+1} = \frac{k_n - k_{n+1}}{k_n + k_{n+1}}, \tag{4-20}$$

The total transfer matrix (MT) is derived by simply multiplying M matrix of each layer from eq. (4-19) from which the total device reflection (R) is then defined as:

$$R = \left|\frac{M_{T_{10}}}{M_{T_{00}}}\right|^2. \tag{4-21}$$

From these equations, it is evident that the device reflection depends on the thickness and the effective refractive index of each layers. Therefore, using amorphous and crystalline GeTe films with two different refractive index values results in two different colors. More number of colors could be achieved using gratings with different filling ratios (f). However, when the period is in the same order as the wavelength ($p \sim \lambda$), equations (4-14) and (4-15) do not hold anymore. The effective refractive index of such grating cannot be simply derived and used in transfer matrix method. Thus, a numerical approach is used to further

study the existing modes.

The device reflected color is studied using finite element modeling (FEM) for different periods of GeTe grating (Figure 44(a)). As before, the change in the refractive index of GeTe tunes the resonance wavelengths and thus the total reflected color at normal incidence. The extracted colors using CIE standard are located on the color map as shown in Figure 44(b).

Angle sensitivity of grating is the main issue when using them in color filters [4.36]. This could be improved (i.e. angel sensitivity is reduced) by the use of a top antireflection coating. The change in the reflection at an oblique incidence is reduced by the use of high index materials such as GeTe and $TiO_2$ in this design. The smaller the period of grating, the less angle sensitive the design will be. This is due to the fact that the sub-wavelength grating cannot be modeled as an effective medium when $p \sim \lambda$. The reflected color of the device is shown on a CIE graph in Figure 45 at different angles of incidence for a-GeTe (A-250, A-450) and c-GeTe (C-250, C-450) grating with period of 250 nm and 450 nm. Even though the angle sensitivity is higher when $p \sim \lambda$ ($p$=450 nm), the crystallization of only 40 nm of GeTe still causes large blue shift in the reflected color. This is due to higher absorption of red light in c-GeTe.

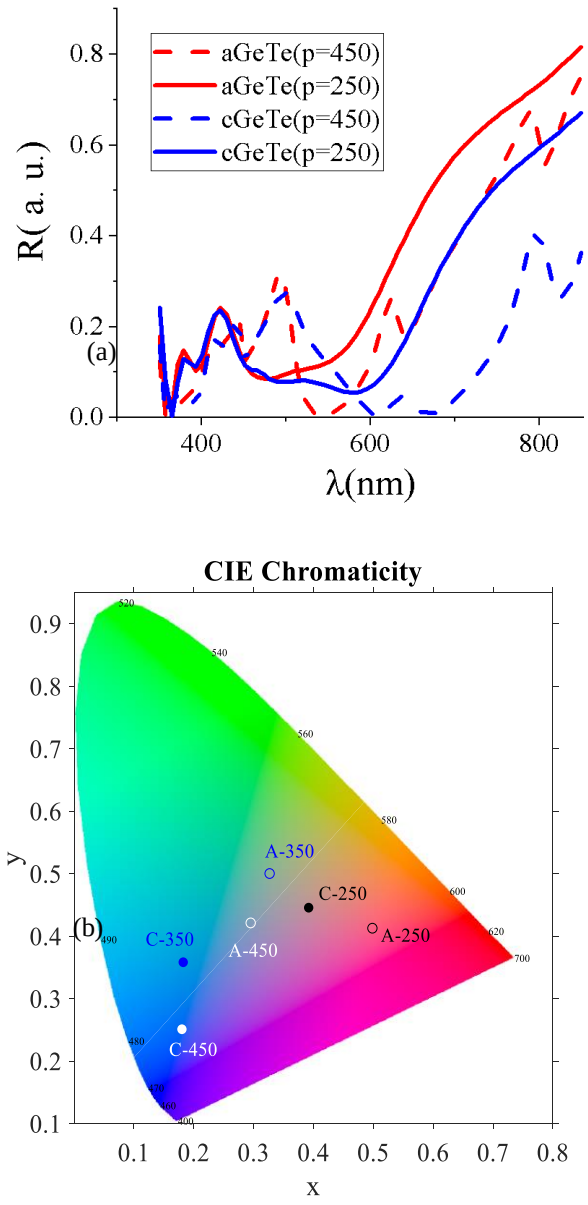


Figure 44: (a): Reflection spectrum for different period of grating consists of GeTe on 12 nm Silver film at normal incidence. (b): Extracted CIE chromaticity graph.

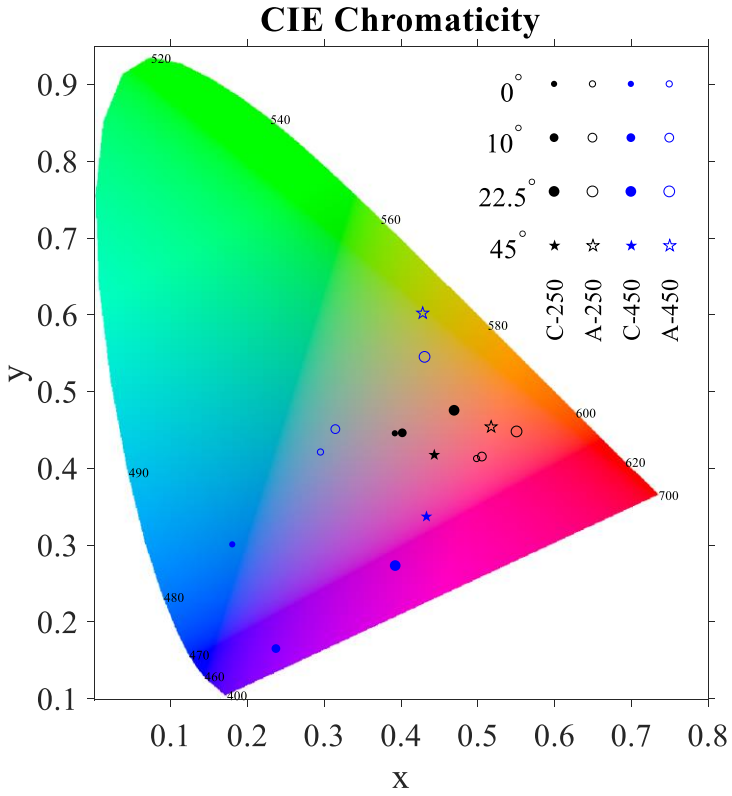


Figure 45: CIE chromaticity graph showing the device reflected colors for two period of 250 nm(black) and 450 nm (blue), which is extracted from modeled reflection of the device from FEM. Device color change with respect to angle is show for GeTe in both amorphous (empty dots) and crystalline (filled dots) states.

Angle sensitivity of the device could be improved in a waveguide with higher refractive index. As shown here, the angle sensitivity is very negligible for smaller periods and all dots on CIE graph are located close to each other for the case of p = 250 nm.

Fabrication and resultsFigure 46 shows the device fabrication process which starts with the deposition of 250 nm $SiO_2$ passivation layer on a Si wafer using a PECVD at 350 ºC. Next, bottom Nickel-Chrome and Palladium films are evaporated. Same PECVD chamber is used to deposit $SiO_2$ and $Si_3N_4$ for the waveguide at 300 ºC. An ultra-thin high conductive silver film on top of a 3-nm Ge wetting layer is then evaporated at a rate of 0.5 Å/s to serve as the integrated heater (15 nm total thickness). This thin layer is then patterned using photolithography and lift-off process. The Ge layer is then passivated with a 3-nm sputtered $SiO_2$ film. Next, a GeTe film is sputtered using Lab-18 sputtering machine (Kurt J. Lesker Co.) at room temperature and 3 mTorr chamber pressure using 60-W RF power source with low 0.6-Å/s deposition rate. This GeTe film is patterned to form the gratings using ZEP etching resist employing e-beam lithography (Jeol-6300). This is followed by $TiO_2$ and $MgF_2$ evaporation to serve as antireflection layer and patterning step of the Au pads.

SEM images of the device is shown in Figure 47 for Michigan logo for the grating with a 450-nm period. The reflected light spectrum is measured using Woollam M-2000 ellipsometer utilizing focusing beam objectives for an area of 500 μm by 500 μm at a 45° angle of incidence.

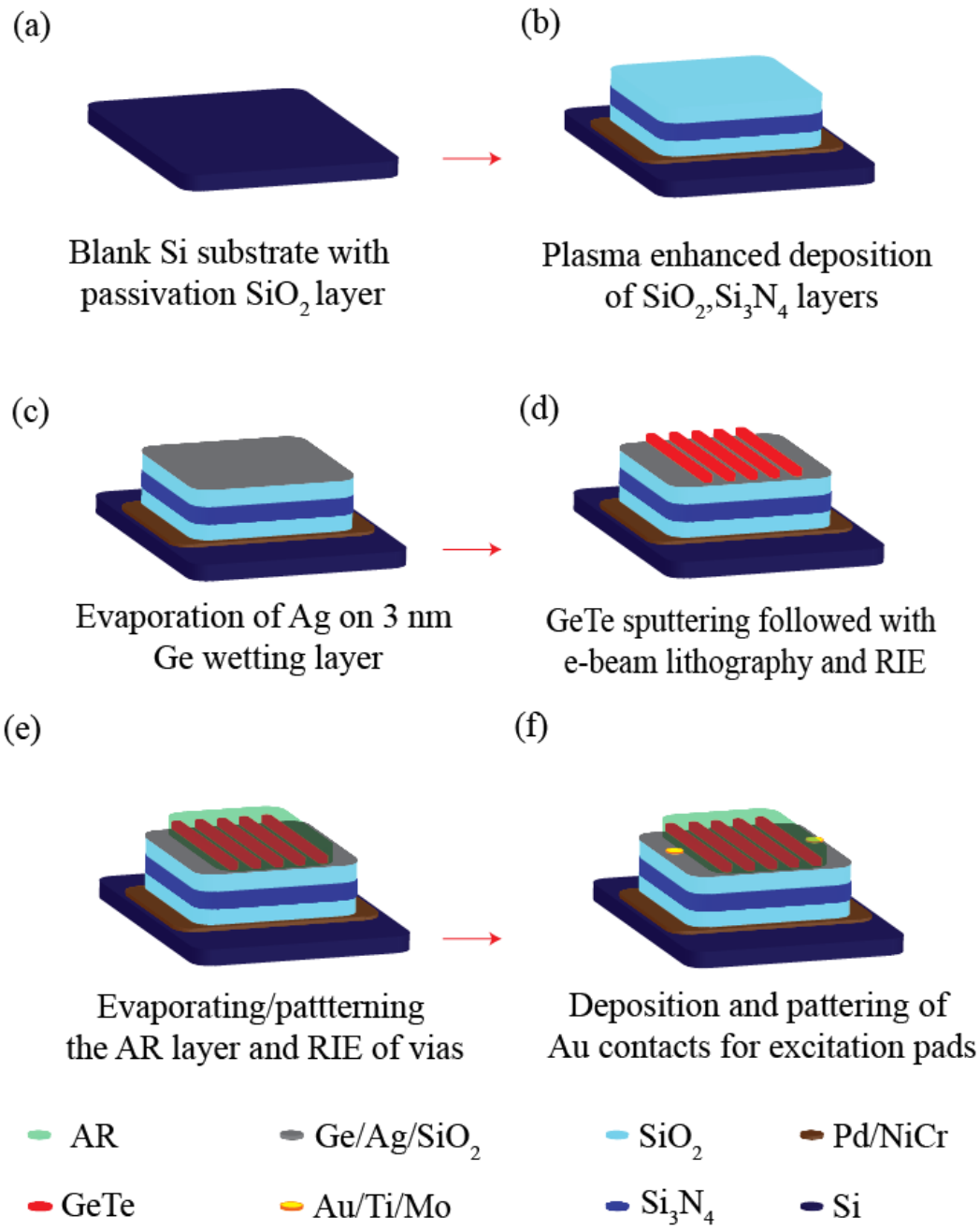


Figure 46: Fabrication process of the device.

The reflected spectra are shown in Figure 48 for c-GeTe verifying the modeling (stars in Figure 45). The actual reflected colors of devices with different grating periods at each state of GeTe is shown in Figure 49. The Joule heating voltage applied for complete crystallization of all gratings was 3.4 V. As shown here red, green, orange, and blue colors were achieved using different grating periods and different phases of GeTe.

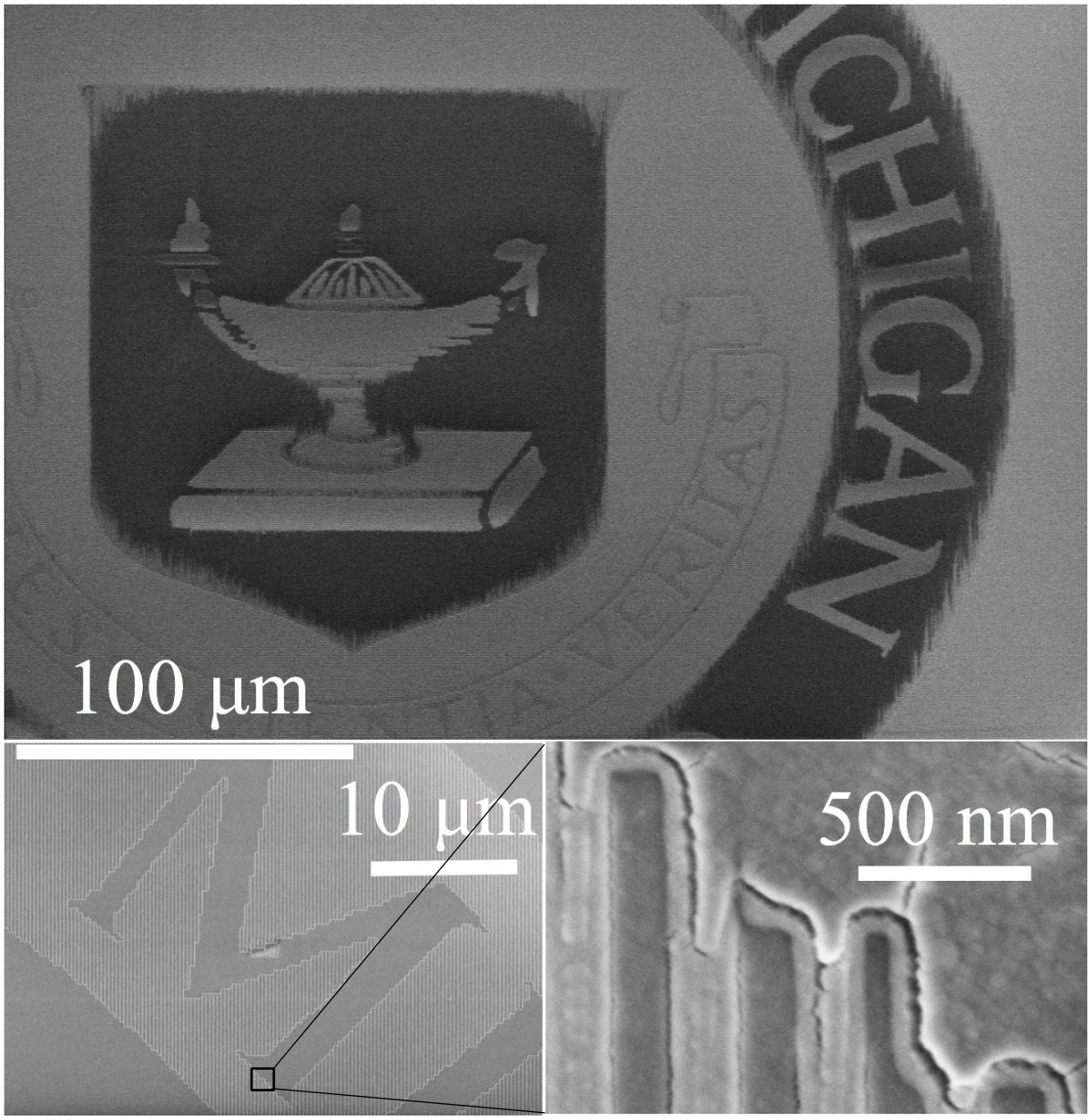

Figure 47. SEM micrograph of Michigan logo made with GeTe grating.

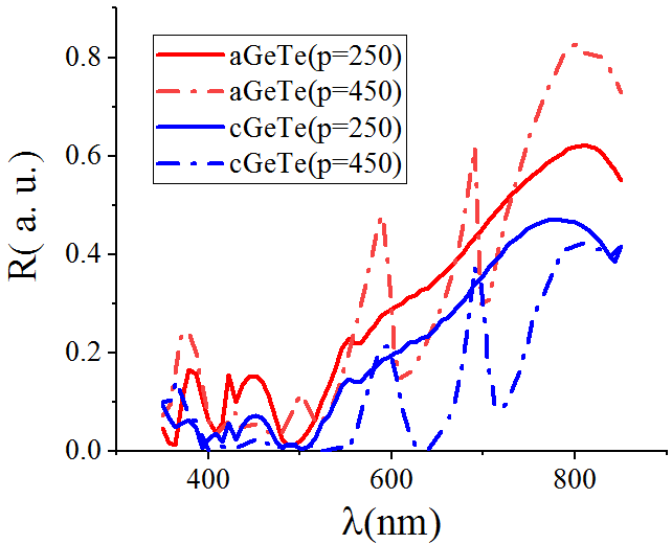


Figure 48: Device reflections at 45º angle of incidence using ellipsometry measurement; blue, green and red colors achieved with different periods and phase of GeTe gratings.

A large contrast of red to orange color tuning is achieved with transitioning the GeTe for the devices with 250 nm period of the grating. Yellow and dark green colors were also transitioned to light green and blue for the case of 350 nm and 450 nm periods, respectively.

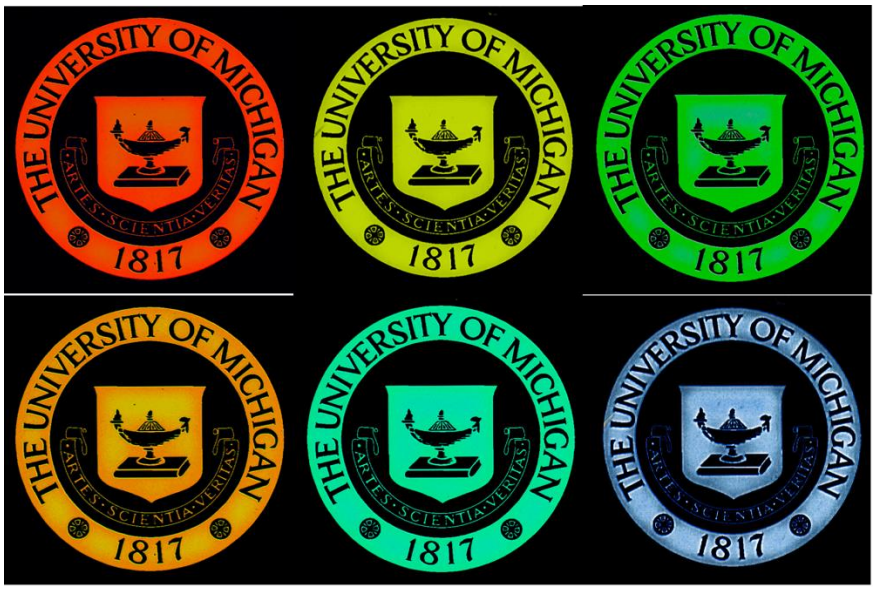


Figure 49: Reflected color of the devices with grating period of 250 nm (left), 350 nm (middle) and 450 nm (right) for amorphous (top) and crystalline (bottom) phases of GeTe. The diameter of the Michigan Logo is 350 μm.

To conclude, within this chapter, several color reflectors were demonstrated by using multiple layers of GeTe sandwiched between $TiO_2$ films. Design and modeling details were discussed along with the fabrication methods. Multiple colors ranging from blue to red were achieved within the same pixel area by selective transitioning of two GeTe films (of 8 and 20 nm) using the same heater with zero power needed to remain in each color. Moreover, a waveguide grating color reflector was presented to enhance the quality of the reflected colors. Such a device consists of a grating of GeTe with sub-wavelength period

and a glass waveguide with $Si_3N_4$ cladding to enhance the color dynamics. A thin silver film was used under the grating for a more efficient joule heating approach.

## 4.8. References


[4.1] Li, Jie, et al. "Highly Efficient Organic Light-Emitting Diode Based on a Hidden Thermally Activated Delayed Fluorescence Channel in a Heptazine Derivative." Advanced Materials 25.24 (2013): 3319-3323.

[4.2] Zhu, Minrong, and Chuluo Yang. "Blue fluorescent emitters: design tactics and applications in organic light-emitting diodes." Chemical Society Reviews 42.12 (2013): 4963-4976.

[4.3] Lee, Kyu-Tae, et al. "Strong Resonance Effect in a Lossy Medium-Based Optical Cavity for Angle Robust Spectrum Filters." Advanced Materials 26.36 (2014): 6324-6328.

[4.4] Do, Yun Seon, et al. "Plasmonic Color Filter and its Fabrication for Large-Area Applications." Advanced Optical Materials 1.2 (2013): 133-138.

[4.5] Gelinck, Gerwin H., et al. "Flexible active-matrix displays and shift registers based on solution-processed organic transistors." Nature materials 3.2 (2004): 106.

[4.6] Sekitani, Tsuyoshi, et al. "Stretchable active-matrix organic light-emitting diode display using printable elastic conductors." Nature materials 8.6 (2009): 494-499.

[4.7] Cho, Himchan, et al. "Overcoming the electroluminescence efficiency limitations of perovskite light-emitting diodes." Science 350.6265 (2015): 1222-1225.

[4.8] Chan, Edward K., et al. "Erratum to “Continuous Color Reflective Display Fabricated in Integrated MEMS-and-TFTon-Glass Process”." Journal of Microelectromechanical Systems 26.2 (2017): 464-465.

[4.9] Chang, Lingqian, Feng Chen, Xiaokang Zhang, Tairong Kuang, Mi Li, Jiaming Hu, Junfeng Shi, Ly James Lee, Huanyu Cheng, and Yiwen Li. "Synthetic Melanin E-Ink." ACS Applied Materials & Interfaces (2017).

[4.10] Lee, J., Chen, H. F., Batagoda, T., Coburn, C., Djurovich, P. I., Thompson, M. E., & Forrest, S. R. (2016). Deep blue phosphorescent organic light-emitting diodes with very high brightness and efficiency. Nature materials, 15(1), 92.

[4.11] Yoo, S., Gwon, T., Eom, T., Kim, S., & Hwang, C. S. (2016). Multicolor changeable optical coating by adopting multiple layers of ultrathin phase change material film. Acs Photonics, 3(7), 1265-1270.

[4.12] Hong, J., Chan, E., Chang, T., Fung, T. C., Hong, B., Kim, C., Wen, B. (2015). Continuous color reflective displays using interferometric absorption. Optica, 2(7), 589-597.S

[4.13] Ma, J. (2015). Advanced MEMS-based technologies and displays. Displays, 37, 2-10.S

[4.14] Chen, C. P., Li, Y., Su, Y., He, G., Lu, J., & Qian, L. (2015). Transmissive Interferometric Display With Single-Layer Fabry–Pérot Filter. Journal of Display Technology, 11(9), 715-719.

[4.15] Lee, Kyu-Tae, et al. "Subwavelength nanocavity for flexible structural transmissive color generation with a wide viewing angle." Optica 3.12 (2016): 1489-1495.Mortimer, Roger J. "Electrochromic materials." Chemical Society Reviews 26.3 (1997): 147-156.

[4.16] Raymo, Françisco M., and Massimiliano Tomasulo. "Optical processing with photochromic switches." Chemistry-A European Journal 12.12 (2006): 3186-3193.

[4.17] Granqvist, Claes-Göran. "Electrochromic materials: out of a niche." Nature materials 5.2 (2006): 89-90.

[4.18] Zakery, A., and S. R. Elliott. "Optical properties and applications of chalcogenide glasses: a review." Journal of Non-Crystalline Solids 330.1 (2003): 1-12.

[4.19] Wang, Zhongrui, et al. "Memristors with diffusive dynamics as synaptic emulators for neuromorphic computing." Nature materials 16.1 (2017): 101-108.

[4.20] Ordinario, David D., et al. "Protochromic Devices from a Cephalopod Structural Protein." Advanced Optical Materials (2017).

[4.21] Humar, M., et al., “Electrically tunable liquid crystal optical microresonators,” Nature Photonics, 3(10), pp. 595-600. (2009).
[4.22] Yang, DK., “Fundamentals of liquid crystal devices,” John Wiley and Sons, (2014).
[4.23] Ramesh, K., et al. "Electrical Switching in germanium telluride glasses doped with Cu and Ag." Applied Physics A: Materials Science & Processing 69.4 (1999): 421-425.
[4.24] Hosseini, P., Wright, CD., and Bhaskaran, H., “An optoelectronic framework enabled by low-dimensional phase-change films”. Nature, 511(7508), pp. 206-211. (2014).
[4.25] Liu, Mengkun, et al. "Terahertz-field-induced insulator-to-metal transition in vanadium dioxide metamaterial." Nature 487.7407 (2012): 345.
[4.26] Jafari M. and Rais-Zadeh M., “Zero-static-power phase-change optical modulator,” Optics letter, pp. 1177-1180. (2016).
[4.27] Jafari, M. and Rais-Zadeh, M., “A 1550 nm phase change electro-optical shutter.” In IEEE 29th International Conference on Micro Electro Mechanical Systems (MEMS), pp. 655-658. IEEE. (2016)
[4.28] Tittl A., et al. “A switchable mid-infrared plasmonic perfect absorber with multispectral thermal imaging capability.” Advanced Materials 27.31, pp. 4597-4603. (2015).
[4.29] Chen, Yiguo, et al. "Tunable near-infrared plasmonic perfect absorber based on phase-change materials.” Photonics Research 3.3, pp. 54- 57. (2015).
[4.30] Jafari, M., Guo, LJ., and Rais-Zadeh, M., "An ultra-fast optical shutter exploiting total light absorption in a phase change material." In Proc. of SPIE Vol, vol. 10100, pp. 101000I-1. (2017).
[4.31] X. Zhou, J. Kalikka, X. Ji, L. Wu, Z. Song, and R. E. Simpson ”Phase-Change Memory Materials by Design: A Strain Engineering Approach.” Advanced Materials, 28(15), pp.3007-3016.
[4.32] Jafari, M., Guo, L. J., & Rais-Zadeh, M. (2019). A Reconfigurable Color Reflector by Selective Phase Change of GeTe in a Multilayer Structure. Advanced Optical Materials, 7(5), 1801214.
[4.33] C. Zhang, D. Zhao, D. Gu, H. Kim, T. Ling, Y. K. R. Wu , and L. J. Guo, “An ultrathin, smooth, and low-loss Al-doped Ag film and its application as a transparent electrode in organic photovoltaics”, Adv. Mater., vol. 26(32), pp. 5696-5701, 2014.
[4.34] Lu, L., Dong, W., Behera, J. K., Chew, L., & Simpson, R. E. (2019). Inter-diffusion of plasmonic metals and phase change materials. Journal of materials science, 54(4), 2814-2823.
[4.35] P. Lalanne, Philippe, and J. P. Hugonin, “High-order effective-medium theory of subwavelength gratings in classical mounting: application to volume holograms.” JOSA A, vol 15.7, pp. 1843-1851, 1998.
[4.36] J. Zhou, and L. J. Guo, “Transition from a spectrum filter to a polarizer in a metallic nano-slit array”, Sci. rep., vol. 4, pp. 3614, 2014.

# Chapter 5: Future Work

The previous three chapters discussed the active modulating of the light intensity and phase at the NIR and visible regions for optical shutters, modulators, and passive reflective devices. However, several challenges remain in making an integrated product for commercial applications. Among these remaining impediments, phase transition reliability, durability, and large optical loss at the visible range stand out. Reliable electrical or optical phase transitions for several cycles are desirable for all of these devices. The resistive-based PCM devices and memories have been developed and improved within the last two decades to achieve several millions of reliable cycles. However, for the case of the optical PCM-based devices described here, the entire area of the tunable film needs to undergo complete and reversible phase transitions. This is indeed harder than the application employing the resistivity change, where only a crystallization of a filament within the PCM film is sufficient. Even though we have demonstrated several devices with electrical crystallization, amorphization, or both, there is still a considerable deficit in foundational knowledge regarding the material properties required to achieve more reliable optical component based on PCM. In this chapter we briefly outline the reliability issues with the proposed devices and the manner in which we intend to improve the phase transitions, optical contrast, and integration method both through material studies and design modifications.

## 5.1. Reliability and phase transition improvement

Incomplete phase transitions and inability to transition back to fully-amorphous film are the most challenging issues affecting reliability of optical PCM-based devices. Moreover, the change in the compound stoichiometry and degradation of the stack throughout the life-time of the device result in a lower dynamic change for optical and electrical properties that come from phase transitions of the GeTe films. It is important to mention that since electrical devices work based on GeTe resistivity, they do not necessarily require complete crystallization of GeTe film. This is because of the fact that the electrical resistivity switches to low as soon as a small filament of c-GeTe is grown within the film. Since degradation in the GeTe film and the change in the stoichiometry mostly affect the incomplete crystallization process, the resistivity-based devices usually offer better reliability and durability compared to optical devices that were presented in this thesis. To achieve the highest contrast with the uniform optical properties over the surface of the tunable optical devices, the whole area of the GeTe needs to be transitioned effectively.

There are several ways to enhance the phase transitioning of the GeTe films in the optical devices. Integrating nano-meter size heaters within the structure, such as the design discussed in Chapter 2, helps to achieve effective heating and cooling. However, low optical loss of the heater is needed for both modulators and color reflectors. To minimize

the complexity of the design and obviate the need for a matching circuit, the resistivity of the heater needs be designed in the range of 50 Ω. Recently, ultra-thin layers of silver have been developed by adding <5% of aluminum during sputtering [5.1]. By integrating such a thin heater within the GeTe layers as shown in Figure 50 we can potentially achieve more reliable and faster transitions with more control over the input resistance of the device.

Another important method to achieve better crystallization is growing single crystalline films instead of the common approach of sputtering as-deposited amorphous films. Sputtering, although being cheaper and more applicable for large-area devices, results in a lower quality and less uniform compound in the bulk film. High temperature sputtering (>200 °C) of the GeTe could also greatly enhance the optical properties of the film by growing the as-deposited crystalline films.

Furthermore, the degradation of the bulk GeTe film due to the change of the compound stoichiometry during the lifetime of the device results in lower optical contrast due to the mobile Te atoms. A super-lattice structure, such as those with GeTe-$Sb_2Te_3$, could further improve the switching time, energy, and reliability [5.2]. Using $TiO_2$ or other types of high-temperature ceramics can also help to enhance the stability and transitioning of the devices even further. Multiple depositions of layered structures of ultra-thin $TiO_2$ and GeTe films could further improve the phase transitions as well as the optical performances of the tunable devices proposed through this thesis. The optical responses of these designs are yet to be optimized depending on the film properties of the sputtered $TiO_2$ film.

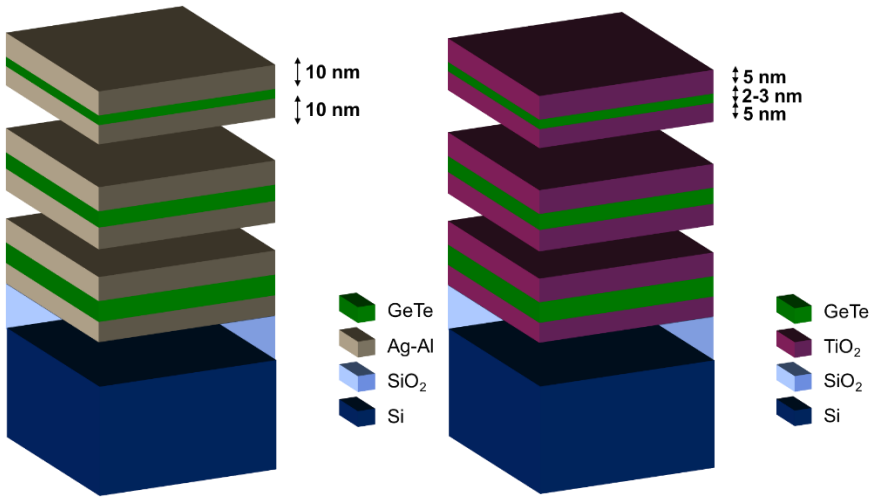


Figure 50. (a) Modulator design utilizing the selective heating with ultra-thin film silvers. (b) stress-engineering of GeTe with $TiO_2$ films to achieve different transition temperatures

To reduce the optical loss in the visible range of the optical spectrum, addition of Selenium (Se) in the GeTe compound could be considerd. As an example, the optical properties of Gallium Selenium (GaSe) films are summarized in Table 5.1. As shown, the refractive index of the films changes by adding Gallium (Ga) to the Se film, however, for all GaSe stoichiometric ratios, the k value is small compared to the GeTe films used in this work. Reported optical characteristics of the phase change materials in the literature have been summarized in the Table 5.2. Based on this table and Table 5.1, there is evidence that increasing the amount of the Se improves the transmission and reduces the k value in the amorphous phase. More characterization on the optical and phase transition properties of GeSeTe is needed to achieve higher transmission (lower loss) at the visible wavelength.

Multiple co-sputtering to grow GeSeTe films with different stoichiometry could help to achieve a film with minimum loss for desired wavelength of interest.

Table 5.1. Reported n and k values of the GaSe film in the amorphous phase

| *Material* | *n* | *k* |
|---|---|---|
| a-Se | 5.15 | 0.045 |
| a-Ga2.5Se97.5 | 1.88 | 0.064 |
| a-Ga5Se95 | 2.64 | 0.062 |
| a-Ga7.5Se92.5 | 4.32 | 0.061 |
| a-Ga10Se90 | 4.65 | 0.060 |

Table 5.2. Properties of the phase change material that are studied previously in the literature

| Material | Amorphous | | Crystalline | |
|---|---|---|---|---|
| | n | k | n | k |
| $Ge_{0.33}Te_{0.67}$ [5.3] | 4.5 | 0.8 | | |
| $Ge_5Se_{95}$ [5.4] | 1.95 | 0.025 | | |
| $Ge_5Se_{93}Te_2$ [5.4] | 2.25 | 0.066 | | |
| $Ge_5Se_{85}Te_{10}$ [5.4] | 2.55 | 0.07 | | |
| $Se_{84}Te_4Ag_{12}$ [5.5] | 3.15 | 0.04 | | |
| GeSe [5.6] | | | 3.75 | 0.2 |
| $GeSe_2$ [5.6] | | | 2.5 | ~0 |
| GeSbSe [5.6] | | | 2.8 | ~0 |
| $Sb_{40}Se_{20}S_{40}$ [5.7] | 2.95 | 0.03 | 3.15 | 0.06 |
| $Ag_8In_{14}Sb_{55}Te_{23}$ [5.8] | ~4.8 | ~1.9 | 4.9 | 1.7 |
| Sb-rich AgInSbTe [5.9] | 3.55 | 2.4 | 3.6 | 4.3 |

The challenge here is that the GeSeTe films also show lower contrast in n and k values between crystalline and amorphous phases compared to those of the GeTe. This results in

smaller modulation index or contrast for the device, which is not desirable. Better optical contrast, however, may be achieved by improving the design, material growth, and more complete phase transitions.

## 5.2. Strain-induced phase transition

Super-lattice structures that consist of the GeTe films, have recently drawn a lot of attention due to their high reliability and phase transitioning kinetics. By having a non-switchable thin film in the order of 1-4 nm within the transitioning GeTe film, one can achieve a very reliable structure, which transitions faster with lower power for several cycles. The effect of strain on the phase transition kinetics has been studied in several papers [5.2]. Here, we propose a novel method of real-time strain modulation of the GeTe film within a mechanical resonator. The dynamic stress that is generated in the ultra-thin GeTe film inside the resonator could result in both mechanical resonance tuning as well as modulation of optical properties. The schematic of such device is shown in Figure 51. The integration of the GeTe film in mechanical resonators could happen by simply depositing a thin film on a thickness mode, or surface acoustic wave (SAW) device. To modulate the mechanical properties of such an acoustic device, intimate integration of the GeTe film within the body of the resonator could be achieved by having GeTe nano-pillars within the piezoelectric material. Dynamic stress modulation of the GeTe film within these resonant

body devices will find great applications in optical modulators, time keeping elements, and temperature sensors.

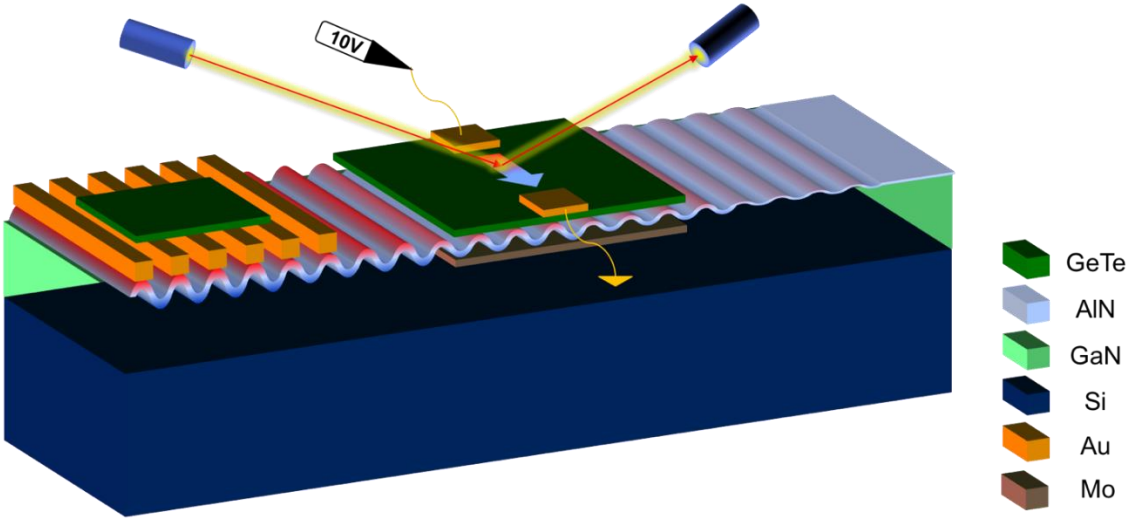


Figure 51. The acoustic-enhanced phase transitioning of a PCM by utilizing a SAW waves. The modulation of the reflection of the light is achievable by applying a RF voltage to the gold interdigitated transducers (IDTs). Thin molybdenum film between the GaN and AlN helps with the simpler integrated of the reflection-based device with such SAW system.

## 5.3. Laser-based heating

Although electrical switching of the GeTe films is very desirable in chip-scale devices with possible integrability, all optical modulation is of utmost need in many applications such as optical telecommunications, thermal imaging devices, and atomic clocks [5.10]. The ultra-fast laser-based phase transitioning of GeTe has been studied for the last decade and has yet to be accomplished within a compact device that makes it possible to be

integrated in a chip-scale system. With proper film protection, such as using $SiO_2$ [5.1], effective and reliable laser-based transitions could be achieved for multi-layer GeTe-based optical devices. Moreover, there is a better control on selective phase transitioing of each layer due to the temperature dependence of the crystallization temperatures for the GeTe films with different thicknesses. This selective annealing is required for multi-phase devices such as color reflectors with more than one layer of the integrated PCM. Figure 52 shows an example of such color reflectors by employing laser annealing, which shows three different colors by utilizing partial crystallization of only one GeTe layer. The image on the right side shows an example of a damaged color reflector during the laser annealing. It is important to optimize the power and the pulse width to prevent film damages due to the laser hitting of the device. A thin 100-nm silicon oxide could be used as protective layer to reduce the films evaporation during annealing [5.11].

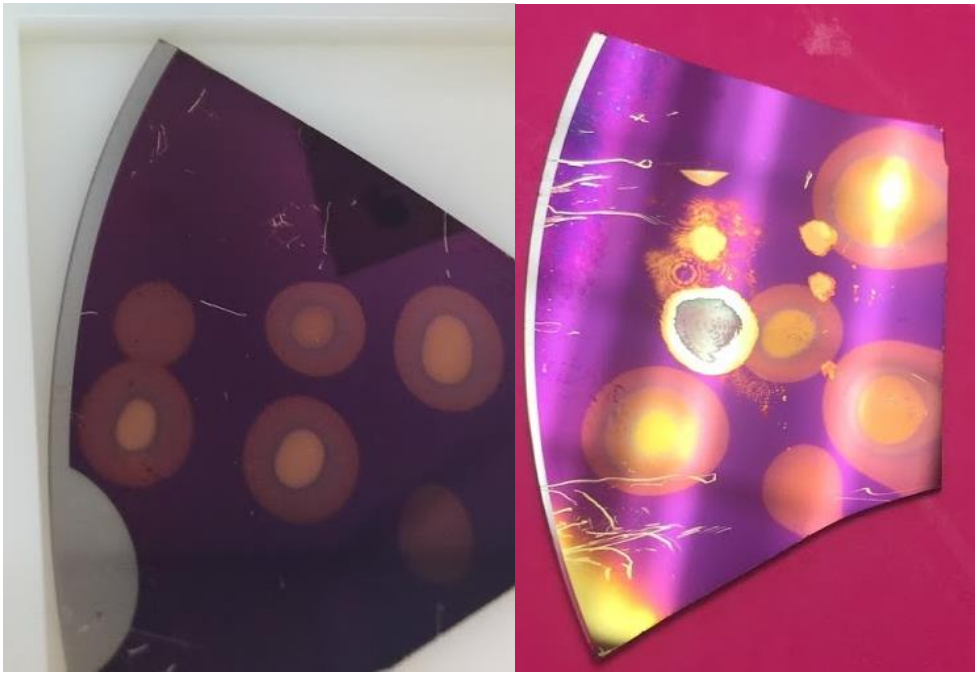

Figure 52. The laser annealing method to produce different color gradient in the stack that consists of GeTe, $SiO_2$ and $TiO_2$ films (left). Film evaporation due to excessive heat for a sample without the protecting oxide layer (right).

## 5.4. Other methods

As mentioned before, one main impediment in developing low-loss devices using GeTe is its high extinction coefficient (k) value at the visible range. This makes it difficult to take advantage of the change in the n and k values of the GeTe for optical devices for the visible range. To have any useful device at visible-NIR, the thickness of GeTe need to be minimized, which reduces the optical contrast that can be achieved from such a device. In an alternative approach, the GeTe can be integrated in a gain/loss periodic design to achieve

very high modulation contrast for the visible range. Space-time reflection symmetry (PT symmetry) based devices recently have shown successful integration in optical devices to reduce loss, enhance the contrast, and improve speed of the light modulations. Thus, for example a periodic 2D-crystal-based device can demonstrate fast and high contrast modulation of the light for the visible and NIR regions.

## 5.5. Conclusion

In this thesis, a new class of reconfigurable optical devices are proposed, designed, and fabricated employing chalcogenide glasses as their core tunable material. The well-known phase change material, GeTe, is used here due to the higher contrast in its optical, electrical and mechanical properties as well as better stability and reversible phase transitions compared to GST, $VO_2$, and LC. The required heat for the phase transitioning of the GeTe is generated through the joule-heating as an effective way to achieve complete and repeatable cycles. The optical reconfigurability, which comes from these phase transitions, is utilized to achieve ultra-high contrast light intensity modulation. Moreover, a passive color reflector with more than four stable colors at room-temperature is shown for the first time by using multiple layers of the GeTe films in a Fabry-Perot cavity. Different optical resonances were utilized to achieve high contrast both in ON/OFF ratio of an optical shutter or the color dynamics at visible and NIR regions. Several reliable phase transitions are shown by applying the pulsed voltage through the integrated heater within such devices.

Furthermore, all proposed devices operate by consuming lower power compared to those made from $VO_2$ or LC due to the stability of both phases of the GeTe (amorphous and crystalline) at the room temperature.

## 5.6. References


[5.1] JK Behera, X Zhou, J Tominaga, RE Simpson. "Laser switching and characterisation of chalcogenides: systems, measurements, and applicability to photonics." Optical Materials Express (Optical Society of America) 7 , no. 10 (2017): 3741-3759.

[5.2] Zhou, X., Kalikka, J., Ji, X., Wu, L., Song, Z. and Simpson, R.E., 2016. Phase-Change Memory Materials by Design: A Strain Engineering Approach. Advanced Materials, 28(15), pp.3007-3016.

[5.3] Kim, T. K., Han, S. S., & Bae, B. S. (1999). Optical and electrical properties of amorphous thin films in Ge x Te 1-x system. Metals and Materials, 5(1), 33-37.

[5.4] Khan, S. A., Zulfequar, M., & Husain, M. (2002). Effects of annealing on crystallization process in amorphous Ge5Se95− xTex thin films. Physica B: Condensed Matter, 324(1-4), 336-343.

[5.5] Al-Ghamdi, A. A. (2006). Optical band gap and optical constants in amorphous Se96− xTe4Agx thin films. Vacuum, 80(5), 400-405.

[5.6] Santos, L. F., Ganjoo, A., Jain, H., & Almeida, R. M. (2009). Optical and spectroscopic characterization of germanium selenide glass films. Journal of Non-Crystalline Solids, 355(37-42), 1984-1988.

[5.7] Naik, R., Parida, S. K., Kumar, C., Ganesan, R., & Sangunni, K. S. (2012). Optical properties change in Sb40S40Se20 thin films by light-induced effect. Journal of Alloys and Compounds, 522, 172-177.

[5.8] Li, J., Hou, L., & GAN, F. (2001). EFFECTS OF SPUTTERING TECHNICAL PARAMETERS ON THE OPTICAL PROPERTIES OF Ag-In-Sb-Te PHASE-CHANGE FILMS [J]. Chinese Journal of Material Research, 5.

[5.9] Guang-Jun, Z., Dong-Hong, G., & Fu-Xi, G. (2005). Optical properties and structure of Sb-rich AgInSbTe phase change thin films. Chinese Physics, 14(1), 218.

[5.10] Park, S. J., Zakar, A., Zerova, V. L., Chekulaev, D., Canham, L. T., & Kaplan, A. "All-optical modulation in Mid-Wavelength Infrared using porous Si membranes." Scientific reports (Nature), 2016: 30211.

[5.11] Weidenhof, V., Pirch, N., Friedrich, I., Ziegler, S., & Wuttig, M. (2000). Minimum time for laser induced amorphization of Ge2Sb2Te5 films. Journal of Applied Physics, 88(2), 657-664.